ABSTRACT

Title of Dissertation: STUDYING MANY-BODY PHYSICS WITH QUANTUM DOT QUBITS

Donovan Buterakos
Doctor of Philosophy, 2022

Dissertation Directed by: Professor Sankar Das Sarma
Department of Physics

Quantum dot spin qubits are a promising platform for realizing quantum information technologies, which can theoretically perform calculations such as factoring large integers that are otherwise intractable using classical computing methods. However, quantum dot qubit technology is still in its developmental phases, with current experimental devices capable of holding only a few (less than 10) noisy qubits. Even with only a small number of quantum dots, interesting experiments can be performed, simulating physical systems and observing many-body phenomena which are otherwise difficult to study or numerically simulate classically.

In the first part of this thesis, we analytically examine valley states in Silicon, which is one obstacle which can potentially lead to information loss in Silicon qubits. Using a perturbative method, we calculate the dynamics of two exchange-coupled quantum dots in which there is a valley degree of freedom. We find that the spin states can become entangled with the valley states of the system if the electrons are not initialized to the correct valley states, which can adversely affect quantum computations performed on these systems. In the second part of this thesis, we

detail how quantum dot plaquettes can simulate the Hubbard model and give many analytic results for different magnetic phenomena that arise under this model. These results include examples of Nagaoka ferromagnetism, violations of Hund's rule, and situations where flatband ferromagnetic ground states are necessarily degenerate with nonferromagnetic states. These phenomena all require only a few quantum dots, and are observable with current experimental technologies.

STUDYING MANY-BODY PHYSICS WITH QUANTUM DOT QUBITS

by

Donovan Buterakos

Dissertation submitted to the Faculty of the Graduate School of the
University of Maryland, College Park in partial fulfillment
of the requirements for the degree of
Doctor of Philosophy
2022

Advisory Committee:
Professor Sankar Das Sarma, Chair/Advisor
Professor Maissam Barkeshli
Professor Alicia Kollar
Professor Jay Sau
Professor Andrew Childs

Acknowledgments

I would like to thank my advisor, Sankar Das Sarma for his role in knowing and selecting the most interesting and relevant subjects to work on from the broad field of condensed matter physics, as well as for his help in answering questions, preparing manuscripts, and his guidance in general throughout my Ph. D. program. He strongly supported and encouraged me to pursue my own research interests, while providing concrete directions for my specific projects.

I would like to recognize my colleagues at the Condensed Matter Theory Center, many of whom I have coauthored papers with, and many more of whom have provided insightful and informative discussions about many different topics in our field. Specifically, I would like to thank Haining Pan, whose discussion about ferromagnetism directly impacted this work. I would also like to remember and appreciate Janet Das Sarma, both for warmly welcoming me personally to CMTC, and for keeping the center running smoothly and efficiently. Without her tireless work and sacrifice, CMTC and its unique, collaborative environment would not exist.

I would like to thank Maissam Barkeshli, Alicia Kollar, Jay Sau, and Andrew Childs for being on my advisory committee. I also appreciate my previous research advisors from Virginia Tech, Sophia Economou and Ed Barnes, for mentoring me during my Master's program, and for introducing me to the fascinating subject of quantum information.

I greatly appreciate my parents, who worked hard for many years homeschooling me and enabling me to pursue my passion of learning and studying math. I would also like to thank my

grandmother, who gifted me a book of 1000 colorful math puzzles which fueled and inspired my curiosity. Finally, I love and appreciate my fiancée Jacy, whose continual friendship, love, and support has kept me happy, motivated, and fulfilled throughout my time here.

Table of Contents

List of Tables

List of Figures

List of Abbreviations

1D	1-Dimensional
2D	2-Dimensional
2DEG	2-Dimensional Electron Gas
3D	3-Dimensional
$\mathring{A}$	Angstrom
AlGaAs	Aluminum Gallium Arsenide
BCC	Body Centered Cubic
CPU	Central Processing Unit
Co	Cobalt
CuCl	Copper Chloride
FCC	Face Centered Cubic
Fe	Iron
GaAs	Gallium Arsenide
InGaAs	Indium Gallium Arsenide
mK	millikelvin
Ni	Nickel
N.N.	Nearest Neighbor
N.N.N.	Next-Nearest Neighbor
PBC	Periodic Boundary Conditions
QD	Quantum Dot
Si	Silicon
SiGe	Silicon Germanium
Si-MOS	Silicon Metal Oxide Semiconductor
SU(n)	Special Unitary Group of degree n

Chapter 1: Introduction

Initially discovered in the early 1980s [1, 2], quantum dots are nanoparticles with size on the order of tens of Angstroms. Quantum dots have many similar features to atoms, most notably their spacial localization and discretized electronic states, and hence quantum dots are often informally referred to as "artificial atoms." Since their discovery, a great deal of experimental and theoretical work has been done in developing nanoparticle technology, and a wide range of applications for quantum dots exist [3, 4].

Of particular interest for this thesis is the development of semiconductor quantum dot qubits. It has been demonstrated that the information necessary for implementing quantum algorithms can potentially be held and processed using the spins of electrons trapped within quantum dots [5]. Electron spins are particularly useful for this purpose due to their long coherence times. There is a large ongoing effort to fabricate quantum dot devices robust enough to implement such algorithms. While there have been recent advances in other quantum information platforms such as superconducting transmon qubits [6], quantum dot qubits provide several key long-term advantages such as their small size, long coherence times, potential for scalability, and integration within the current semiconductor industry. However, industrial-level quantum information technologies using quantum dots are still many years away, as current experiments have only achieved on the order of 4 to 9 noisy quantum dots [7, 8, 9, 10, 11].

In this thesis, we investigate one of the potential obstacles to realizing quantum information technologies with quantum dots, as well as some of the potential applications of current experimental technology. In the remainder of this chapter, we review the background of proposed quantum information technologies, the progress of implementing these with quantum dots, and their applications in modeling many-body physics. In chapter 2, we investigate the valley degeneracy of Silicon, which is the standard material used in current quantum dot qubit experiments, detailing its potential adverse effects to qubit coherence, as well as the ability for these effects to go unnoticed in simple experiments. In the remaining chapters, we discuss the applications of small quantum dot qubit arrays in studying many-body physics by simulating the Hubbard model. Specifically, we give in-depth models of arrangements of several quantum dots, showing that interesting many-body phenomena exist such as Nagaoka ferromagnetism, flatband ferromagnetism, and counterexamples to Hund's rule, and crucially these phenomena require on the order of 4-9 sites on a plaquette, and thus their observation can reasonably be attempted with current quantum dot technologies.

1.1 Background of Quantum Information Technology

A Turing machine [12] is a minimal mathematical model which, as asserted by the so-called Church-Turing thesis [13, 14], is capable of simulating any classical computational algorithm. In 1980, Paul Benioff proposed a quantum mechanical model of a Turing machine, showing that computations are possible using Hamiltonian dynamics [15, 16]. Such a computational system has additional benefits beyond implementing classical algorithms. In 1981, Richard Feynman argued that many molecular systems are too complex to efficiently model classically; however,

he proposed that by using a computer which is quantum mechanical by nature, many otherwise difficult quantum problems could be solved [17]. Indeed, in chapter 4 of this thesis, we find that solving the Hubbard model via exact diagonalization cannot be done for more than 16 sites without requiring extensive classical computational resources, due to the exponential growth of the size of the Hilbert space as a function of the number of sites. These works by Feynman and Benioff, along with the Russian paper "Computable and Uncomputable" by Manin [18], were the first steps towards imagining a quantum computer. Several years later, David Deutsch extended the Church-Turing thesis to define the notion of a universal quantum computer as a device capable of performing any quantum algorithm, thus forming the basis of universal quantum computing theory [19].

The power of quantum computation was shown to be particularly useful with the development of Shor's algorithm [20, 21]. Shor was able to show that using the principle of quantum superposition, one could compute the order of a numerical group element in polynomial time, which would allow one to efficiently solve problems such as integer factorization and the discrete log problem, which are foundational to many modern public key cryptography protocols [22]. Because there are no known classical polynomial-time algorithms for either problem, Shor's algorithm provides a new disruptive computational ability, and has been a strong motivation for the ongoing development of quantum hardware. Other quantum algorithms such as Grover's search algorithm [23] offer a similar, though less drastic, speedup over their classical counterparts. Another application of quantum information technologies is quantum public key distribution [24], which allows for verifiably secure information exchange which is fundamentally unbreakable, due to the no-cloning theorem [25]. A long-term physics application for quantum computing is in areas with hard quantum problems such as solving the Hubbard model and quantum chromo-

dynamics.

The biggest obstacle to implementing quantum information technologies is the presence of noise. Noise can be addressed at both a hardware and software level. At the hardware level, coherent errors can potentially be corrected by using dynamical decoupling schemes [26, 27, 28, 29, 30, 31, 32, 33, 34, 35]. These protocols use complicated field pulses to drive qubit operations in such a way that the effects of static noise cancel to leading order in a manner similar to the Hahn spin-echo effect. Incoherent errors can be addressed at the software-level by using error-correcting codes. Theorems exist which prove the feasibility of a quantum error-correcting threshold, which allows for fault-tolerant quantum computation if error rates are reduced below this threshold. Kitaev proposed that anyons on a toric lattice could be used to encode qubits, and that quantum operations could be performed by braiding these anyons around each other [36]. It has been shown that by using this method, quantum algorithms can be implemented to arbitrary precision in a fault-tolerant manner using noisy gates so long as the error rate is below the threshold which has been calculated at around 0.6% to 0.8% [37, 38, 39]. These codes, however, require thousands of physical qubits for each logical qubit realized.

1.2 Quantum Dot Qubits

Quantum dots were proposed as a potential quantum information platform in 1998 [5]. In this proposal, qubits are encoded on electron spins which are trapped inside quantum dots, and operations are applied on the qubits by means of magnetic field pulses and electrically tuning barrier gate voltages between quantum dots. Because controlling spins via magnetic field pulses can be somewhat difficult, alternate qubit schemes have been proposed which do not require a

time-dependent magnetic field. In a singlet-triplet qubit [40], a single qubit is stored in the composite spin state of two electrons each trapped in one of two adjacent quantum dots. The logical qubit states $|0\rangle$ and $|1\rangle$ are encoded by the singlet state $|\uparrow\downarrow\rangle - |\downarrow\uparrow\rangle$ and triplet state $|\uparrow\downarrow\rangle + |\downarrow\uparrow\rangle$. A constant magnetic field gradient is applied across the two quantum dots, and time evolution under this gradient produces a logical σ_X rotation. Controlling the strength of the barrier potential between the two dots by electrically adjusting the voltage of the barrier gates allows control of the strength of the exchange interaction between the two electrons. Because the difference between the singlet and triplet state energies is determined by the exchange interaction, this allows time-dependent logical σ_Z rotations to be performed. These two rotations, along with two-qubit interactions which can be achieved via capacitive or exchange coupling, form a set of universal quantum gates. Significant experimental progress in achieving singlet-triplet qubits has been demonstrated. Other similar qubit encoding schemes exist, such as the 3-QD exchange-only qubit [41, 42], which does not require any magnetic field whatsoever, and the 2-dot 3-electron "hybrid" qubit [43, 44].

There has been significant experimental progress towards realizing quantum dot qubits. Singlet-triplet qubits have been created in GaAs [45], and two-qubit entangling gates have been performed between them with 90% fidelity [7]. While initial quantum dot qubits were implemented using GaAs systems, currently Silicon-based devices show particular promise due to their long coherence times [46, 47], although some experimental work is also done in Germanium [48, 49, 8]. Currently single qubit gates have been performed in Si with fidelities up to 99.9% [50, 51], and two qubit gates with fidelities up to 95% [52, 53]. These fidelities, however, are still short of the requisite 99% threshhold for fault-tolerant quantum computing. Continued progress in experimental work indicates that the necessary threshold will soon be reached with

quantum dot qubits. The potential for scalability in Si devices has also been demonstrated with the fabrication of a nine-qubit linear array [10].

1.3 Physical Structure of Quantum Dots

It was first noticed in 1981 that CuCl microcrystals exhibited an optical blueshift in the exciton absorption spectra [1]. This blueshift was dependent on the radius of the crystal and became most pronounced for crystals with radii on the order of $20\mathring{A}$, at which size quantum effects become relevant. This effect was explained shortly after by modeling the crystal as a spherical potential well with infinite walls. Due to their small size, electronic states within quantum dots are quantized, which leads to a widening of the gap between the conduction and valence bands by the zero-point energy of the confinement potential, which in turn produces the blueshift in the exciton absorption spectra [2]. This is the beginning of quantum dots being used as artificial atoms.

Six years later, it was shown that quantum dots could be formed by applying lithographic electrostatic confinement potentials to a two-dimensional electron gas [54]. In this experiment, a thin 2D InGaAs sheet was grown and embedded between two AlGaAs insulating barriers. A 2D approximate harmonic potential is then applied via metallic gates, which in combination with the AlGaAs barriers, confines electrons in all three dimensions. A schematic of this technique, which is still used in current experiments with varying materials, is shown in Fig. 1.1. Electrons are trapped within the circular cavity by Coulombic repulsion from the electrostatic barrier gates, and the electrons are confined in the vertical direction by the insulating barriers.

In the vertical direction, an electron trapped in a quantum dot can be modeled as a particle in

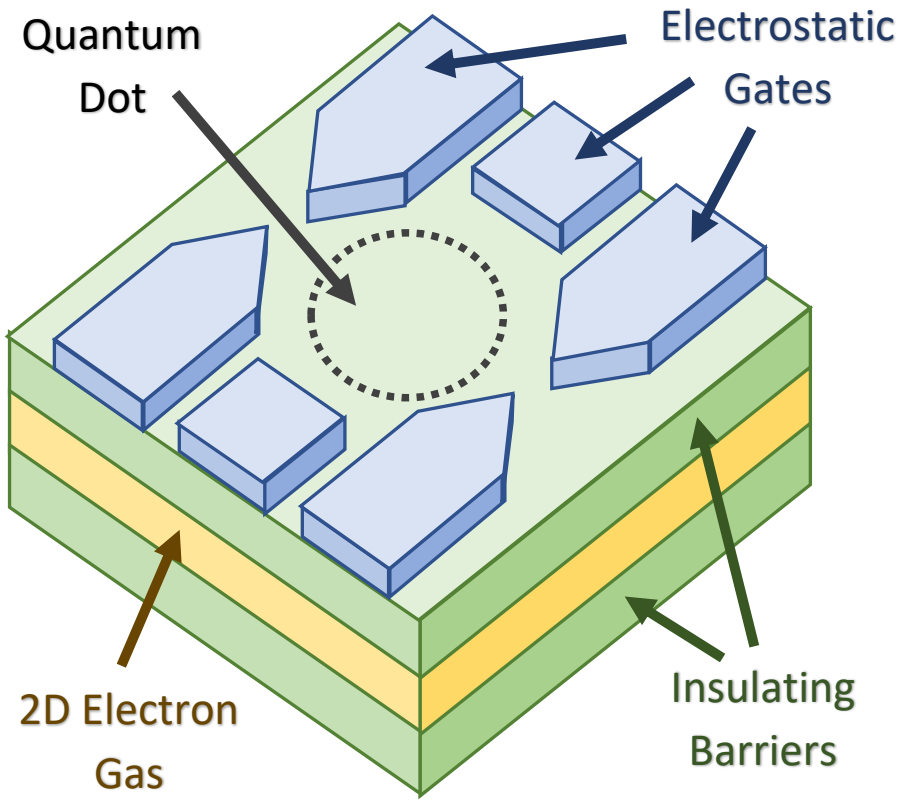

Figure 1.1: Schematic of a 2DEG quantum dot. Insulating barriers are placed around an electron gas, confining electrons to two dimensions. Then an electrostatic confinement potential is created by adjusting the voltage of metallic gates on the surface of the device. This traps electrons within a finite region, creating a quantum dot.

a square potential well. The resulting energy difference between the ground state and first excited state is well known, given by $3\pi^2\hbar^2/(2mL^2)$, where m is the effective mass of the electron, and L is the width of the electron gas layer. Because L is much smaller than the 2D radial size of the quantum dot, this energy difference is large enough that it plays very little role in the dynamics of the system, and thus the quantum dot can be treated as a purely 2D system. The lowest quantum level in this system forms a spin qubit by using the spin up and spin down states of an electron which occupies it.

The microscopic Hamiltonian within the 2D plane of the electron gas is not precisely

known, and in fact it may vary among devices depending on the exact arrangement of the electrostatic gates. It is often modeled as a harmonic potential; however, due to screening within the electron gas, it may in actuality be much flatter of a curve, closer to a rectangular barrier within the circular radius. Whatever the case, the ground state will be similar in features to a bell curve, where the majority of the wave function lies within the quantum dot, but where an exponentially decreasing tail extends outwards from the edge of the dot. If the tail of the wavefunction extends into the space of a neighboring quantum dot, quantum mechanical tunneling can occur between the two dots. The tunneling coefficient t_{ij} between dots i and j is defined by:

$$-t_{ij} = \langle \psi_i | H | \psi_j \rangle \tag{1.1}$$

where H is the Hamiltonian, and ψ_i and ψ_j are the ground states of each respective dot. If ψ_i and ψ_j are defined to have the same phase (and thus are translationally equivalent), then the sign of the matrix element $\langle \psi_i | H | \psi_j \rangle$ will be negative, because tunneling is driven by the kinetic term of the Hamiltonian $-\frac{\hbar^2}{2m}\frac{\partial^2}{\partial x^2}$, which produces a minus sign when acting on the exponentially decaying tail. In this thesis, we choose to define t_{ij} to be the absolute value of the tunneling coefficient, and include the minus sign explicitly in our equations. The strength of the tunneling coefficient for a constant potential barrier tends as $\exp(-\sqrt{2mV})$, where V is the height of the potential barrier between the two dots. Because V is determined by the voltage of the electrostatic gates which can be changed arbitrarily over the course of the experiment, the value of the tunneling coefficient t_{ij} can be freely controlled. While some applications such as dynamical decoupling require a precise knowledge of the microscopic Hamiltonian, for many applications it suffices to simply measure and work with the tunneling coefficient t_{ij} itself. Because the gates

are controlled electrostaticly, they are very fast, operating on the order of nanoseconds, which is one compelling advantage of using quantum dot qubits.

1.4 Valley Degrees of Freedom in Silicon

Silicon has become the current standard material for developing quantum dot qubit devices; however, Silicon has one potentially troublesome property that other materials such as GaAs do not have, the valley degree of freedom. This arises when considering the Fermi surface of Silicon, that is, the momentum space boundary of the set of occupied electronic states at zero temperature. In many cases, the Fermi surface of a metal approximates a sphere centered at zero momentum, corresponding to the simple dispersion relation $E = k^2/2m$. Here because the energy E does not depend on the direction of the momentum $\vec{k}$, but only on its magnitude, electrons at zero temperature will fill the states near $\vec{k} = \vec{0}$ first, occupying higher-momentum states only once the lower-momentum states are filled. However, as the Fermi surface approaches the Brillouin zone, its shape generally becomes much more irregular, in many cases changing quite drastically. This is the case with electron-doped Silicon, whose Fermi surface splits into six identical disconnected electron pockets as illustrated in Fig. 1.2. This is detrimental to creating silicon spin qubits, where it is necessary to keep electrons confined to a single orbital state, as here electrons can fill any one of six degenerate states. The situation can be remedied somewhat by applying tensile strain to the sample, which can energetically separate two of the valleys from the others. These two valley states remain degenerate up to a small energy splitting arising from microscopic imperfections in the interface between materials [55, 56]. This valley splitting is difficult to control and measure, and varies from dot to dot on the same device. While the valley splitting can be enough to

limit electrons to a single state, valley effects continue to be an issue in Silicon quantum dot experiments [57].

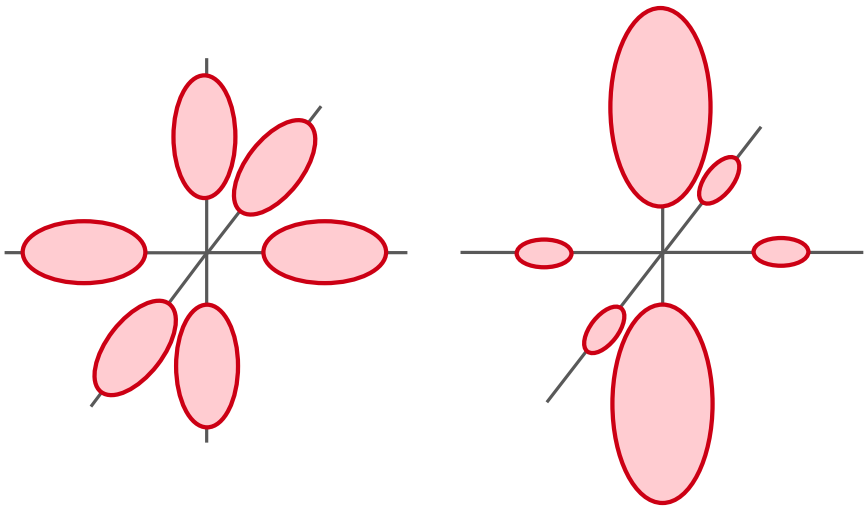

Figure 1.2: Illustration of the Fermi surface of isotropic silicon (left) and silicon under tensile strain (right).

1.5 The Hubbard Model

Although the effects of the excited states may be necessary to track for calculating the precise numeric interqubit coupling, the overall physics of the system is often sufficiently encapsulated in models involving just the ground states of each dot, and in fact, qubits are often operated in single-level occupation in each dot. In addition to tunneling between dots, it is important to consider electron-electron interactions whenever more than one electron is present in a system. Electron-electron interactions arise due to Coulombic repulsion between particles, and although the Coulomb force is long-range in vacuum, due to screening in semiconductors, Coulombic interactions are often become short range. The simplest model involves a so-called zero-range interaction, where the interaction range is smaller than the distance between quantum

dots, and thus the electrons only interact when they are within the same dot. In chapter 3 of this thesis, we investigate in detail the effects of longer-range electron-electron interactions; however, the physics of quantum dot systems are often determined qualitatively by the zero-range model.

A second quantized Hamiltonian which includes a zero-range electron-electron interaction and tunneling coefficients between dots can be written as follows:

$$H = \sum_{i,j} \sum_{s \in \{\uparrow,\downarrow\}} -t_{ij} c_{is}^{\dagger} c_{js} + \sum_{i} \frac{U}{2} n_i (n_i - 1) \tag{1.2}$$

where c_{is} is the annihilation operator for an electron with spin state s in the ground state of quantum dot i, and $n_i = c_{i\uparrow}^{\dagger} c_{i\uparrow} + c_{i\downarrow}^{\dagger} c_{i\downarrow}$ is the number operator which encodes the number of electrons present in dot i. Here U is the strength of the zero-range interaction; specifically, if two electrons occupy the same dot, then the resulting state will have additional energy U to account for the potential energy of two identical fermions in close proximity to one another. This interaction term does not affect particles in different dots.

Eq. (1.2) is the well-known Hubbard model, which was first proposed in 1963 with the hope of explaining the emergence of ferromagnetism in transition metals starting from a microscopic model [58]. In this case (as with many cases where this model is used), each site represents an atomic orbital in the conduction band of a metal rather than quantum dot bound states. The connection between the Hubbard model and quantum dots was first noted in 1994 when it was proposed that the Hubbard model could potentially be simulated using arrays of quantum dots [59, 60, 61]. This goal was only recently realized in an experiment at Delft [9] wherein a distinct many-body phenomenon which arises from the Hubbard model, namely Nagaoka ferromagnetism, was observed in a small plaquette of four quantum dots.

Despite the simplicity of the Hubbard model, numerous many-body phenomenon emerge from it. For example, the emergence of the exchange interaction is straightforward when considering two electrons trapped within a pair of quantum dots – this is equivalent to the Hubbard model mapped onto the Heisenberg model, which is often used as a minimal quantum computing model. If the electrons form a spin triplet, then tunneling between the dots cannot occur because the Pauli exclusion principle forbids two electrons with the same spin from occupying the same orbital state. In this case, each electron will occupy its own dot, and the total energy of the state will simply be the sum of the ground state energies of the two dots, which we shall set to 0 without any loss of generality.

In comparison, there are three allowed orbital states when the electrons form a singlet: the $(1,1)$ configuration where each electron inhabits its own dot, and the states where both electrons share a single dot, namely the $(0,2)$ and $(2,0)$ configurations. Here the states are notated by how many electrons occupy the first and second dot respectively. The $(1,1)$ state has energy 0, but the $(0,2)$ and $(2,0)$ states each have energy U because they possess a doubly-occupied dot. The $(1,1)$ state is connected to both of the other states via tunneling, as $\langle 1,1|H|0,2\rangle = -\sqrt{2}t$. Then the full singlet Hamiltonian is given by:

$$H_S = \begin{pmatrix} U & -\sqrt{2}t & 0 \\ -\sqrt{2}t & 0 & -\sqrt{2}t \\ 0 & -\sqrt{2}t & U \end{pmatrix} \tag{1.3}$$

If $U \gg t$, as is generally the case because hopping is exponentially weak, then the ground state of this matrix has energy $J = -4t^2/U$. Thus, the $(1,1)$ state can lower its energy by

slightly mixing with the higher energy states. This difference between the singlet and triplet energies gives rise to the exchange interaction J, under which electrons in neighboring quantum dots will slowly exchange spins with one another. This interaction is essential to singlet-triplet qubits, as discussed above. Because the exchange interaction gives a lower energy to spin singlets, multi-electron states under the Hubbard model generally tend to prefer antiferromagnetic configurations. However, this is not always the case, as it has been shown that the Hubbard model will have ferromagnetic ground states under certain specific circumstances, which have come to be known as Nagaoka ferromagnetism [62] and flatband ferromagnetism [63]. The details for how this occurs are the topics of chapters 3 and 4 of this thesis.

Chapter 2: The Valley Problem in Silicon Quantum Dots

2.1 Introduction

Silicon quantum dots have shown to be a promising candidate system for realizing quantum information technologies due to their long coherence times, fast gate times, potential for scalability, and integration within the current semiconductor industry. Significant progress has been made in the study of Si-based quantum-dot type qubits either using Si-MOS or Si-Ge devices including these representative (but by no means exhaustive) recent experimental publications [10, 11, 52, 53, 64, 65, 66, 67, 68, 69, 70, 71, 72, 73, 74, 75]. An eventual large-scale quantum computer will solve problems which no classical digital computers can. One such problem, which ushered in the modern era of quantum computing, is the Shor algorithm for prime factorization [21]. This is a problem of great technological interest as it is used in all modern cryptography. Trying to factorize a 1000-digit number, which classical computers cannot do since the computation cost is exponential in the number of digits, one may need roughly a million logical qubits. Since quantum error correction is essential for quantum computing to actually work, each logical qubit may easily require several thousand physical qubits for its realization, so in the end a hypothetical quantum CPU trying to decisively beat classical computers in doing prime factorization may require $\sim 10^{10}$ physical qubits. Although this sounds like a huge number of qubits, an ordinary CPU chip today may host 10^{10} transistors or bits. Each of these transistors or classical bits

is made of silicon, giving Si a huge materials and technological advantage in building a quantum computer. In this context, it is understandable why there are multiple large groups all over the world (e.g. INTEL, Princeton, Wisconsin, Sandia, Delft, Sydney, Hefei...) involved in developing Si-based qubits although in terms of the number of working qubits today, the Si system is well behind ion trap or superconducting transmon qubits. So far, only 1-4 Si qubits have been successfully demonstrated in the laboratory.

The physical property being used to create the Si qubit is the electron spin localized within an effective Si quantum dot near a Si surface or interface with another material, such as Si-SiO2 MOS system or Si-Ge 2D electron system. Since electron spin is by definition a quantum two-level system, an isolated localized electron spin, if it can be manipulated without much decoherence, is an ideal qubit. Silicon has enormous advantage because electron spins in Si are relatively long-lived with long spin coherence times even for natural Si, which can be enhanced greatly by isotopic purification [76]. In addition, two-qubit gates can be implemented by exchange coupling neighboring localized spins by electrically controlling the tunnel coupling between neighboring quantum dots, allowing very fast gate operations. Thus, long spin coherence time, fast electrostatic gating, and the existing Si chip technology allowing scaling up in principle make Si-based quantum information processing extremely attractive. There is however one serious fundamental problem: valley. Bulk Si has six equivalent conduction band minima, with the ground state of Si quantum dots having two valleys which are energetically degenerate in the ideal limit. Thus, ground state Si quantum dot electron spin can in principle be any of the four degenerate spin-valley states. Typically, there is always some valley splitting associated with the surface/interface [55, 56], but the magnitude of this valley splitting is uncontrollable and it varies randomly from dot to dot in essentially a random manner. The valley problem in silicon quantum dots, which has

received little attention in the literature so far although most researchers in the field recognize its importance [55, 56, 76, 77, 78, 79, 80, 81], is the topic of the theoretical work in this chapter.

The Si valley problem has mostly been considered in the context of the valley splitting in the quantum dot qubit being large compared with the qubit temperature ($\sim$ 25-100 mK) so that the thermal occupancy of the higher valley states remains negligible, enabling a valid two-level quantum description of the system in terms of only the electron spin states. This is indeed a serious potential problem as the qubit can no longer be defined if higher valley states are occupied. Therefore, much work has gone into producing Si qubits with large valley splittings through materials development and improved fabrication as well as on characterizing valley splittings in individual quantum dots [82, 83, 84, 85, 86, 87, 88, 89] But, this may not be the only problem when two-qubit gate operations are carried out using inter-qubit exchange coupling. We find that the relative value of the valley splitting with respect to the exchange coupling becomes an important limiting factor even at $T = 0$ when any valley splitting is by definition much larger than the temperature. In particular, we find that the valley splitting must be much larger than the inter-qubit exchange coupling to avoid leakage (i.e. quantum decoherence) for the Si system to operate as a multi-qubit quantum computing platform, and we also find that even when the valley splitting is large, the initialization of the valley states becomes a crucial consideration in multiqubit gate operations. This problem of valley splitting in the context of multiqubit gate operations as determined by the exchange coupling between quantum dots has not attracted attention yet in the literature perhaps because of two reasons: (1) There are very few reports of two-qubit exchange gate operations in Si quantum dot qubits; (2) the currently achieved values for the exchange coupling are very small so that the condition of a valley splitting being larger than the exchange energy is automatically satisfied when the valley splitting is larger than temperature. Since the

speed of the two-qubit gate operations is determined by the exchange coupling strength, higher exchange coupling strength is desirable in the future for progress in Si-based quantum computing, and we want to alert the community that the valley splitting issue is fundamental to two-qubit gate operations as a totally distinct problem from the one involving thermal occupancies of higher valley states.

The problem with having multiple valley states is that their presence can lead to leakage out of the computational space if the valley degeneracy is not adequately broken. Of the six valley states present in bulk Silicon, four of these decouple when strain is applied to the sample, but the degeneracy of the final two valley states is broken only by a small valley splitting term that is dependent on the microscopics of the system[57]. We emphasize that there is no known way to control this valley splitting in specific qubits, and in fact, one can figure out the size of the valley splitting only aposteriori. There is no existing in situ sample diagnostics providing the valley splitting information for the working qubits beforehand. In the current work, we analyze the effect of valleys on the coupled qubit dynamics, finding that valleys are a much bigger problem for coupled qubits than has been realized so far, and the valley problem worsens radically as the number of qubits goes beyond two. In fact, we believe that the Si quantum computing community should worry about the valley problem now before building circuits with tens of coupled quantum dots and finding out that they do not work because of the valley problem. The problem of principle we have uncovered here can be 'fixed' by having small exchange coupling ($\ll$ valley splitting), but this means that the two-qubit gate operations will remain bounded by the valley splitting energies.

In this chapter, we use a Hubbard model to determine the dynamics of a system of two exchange-coupled quantum dots. We show that spin-valley entanglement can easily arise from

time evolution of the system, which is detrimental to the use of the system for quantum information applications. This can be avoided if the valley splitting is large and electrons can be initialized to valley eigenstates, and in fact we show that under these conditions the system maintains coherence and is unaffected to leading order by the valley degree of freedom. If any electron begins in a superposition of valley states then spin-valley entanglement will result, but if the valley splitting is sufficiently large, electrons can be properly initialized to the valley ground state avoiding this situation. However, if the valley splitting is small compared to the exchange interaction strength, then an undesirable spin-valley entanglement is more difficult to avoid, as it will be present unless all electrons are initialized to the same valley state, which is generally difficult to achieve without a large valley splitting.

Additionally, we show that when the valley splitting is small, the measurement probabilities of a two-qubit system are unaffected and are identical to the corresponding measurement probabilities in an ideal system without valley degrees of freedom. However, this is not the case in systems with more than two qubits, and we give examples of gate sequences which give different measurement probabilities in a system with valley states than in an ideal system. Because valley degeneracy affects larger systems but not two-qubit systems, two-qubit gate fidelities measured in two-qubit systems may not accurately account for the effects of valley states, as these effects are only observable in larger system sizes containing more than just two qubits. This last property we discover has not been mentioned in the literature at all, and there has been a feeling that if the two-qubit gates work, the valley degeneracy problem is irrelevant. We show that this is false– one could have perfectly working two-qubit gates, but the system will lose quantum information through spin-valley entanglement as one scales up to more qubits. This is a very serious issue requiring a resolution before more qubits are added to the circuit. We work at $T = 0$

throughout so that the well-understood problem of the thermal occupancy of higher valley states is a non-issue. We consider the valley degeneracy question only in the context of gate operations driven by the inter-dot exchange coupling. Just to avoid any misunderstanding, our definition of 'large' and 'small' valley splitting is as compared with the inter-dot exchange coupling, and not compared with temperature as we are at $T = 0$. Thus, the valley splitting could be large (or small) for our two-qubit considerations even if it is considered to be small (or large) for thermal occupancies relevant for single qubit operations. For example, when the exchange coupling is large, as necessary for fast two-qubit gate operations, the valley splitting for our consideration is small independent of temperature.

This chapter is organized as follows: in Sec. 2.2, we present our model and give the Hamiltonian that we use. In Sec. 2.3, we diagonalize the Hamiltonian for a system of two electrons in two quantum dots, for both triplet and singlet spin configurations. In Sec. 2.4, we discuss the dynamics of the two-qubit system, first for the case where the valley splitting is large, then also for the case of small or zero valley splitting. In Sec. 2.5, we give examples of gate sequences in four-qubit systems where valley effects are observable even when they are not detectable in the two-qubit situation, and we give our conclusions in Sec. 2.6. The contents of this chapter have been published in Ref. [90].

2.2 Model and Hamiltonian

The Fermi surface of Silicon contains six electron pockets, leading to a six-fold degeneracy in the band structure minima. By applying tensile strain to the sample, two of these valleys are energetically separated from the other four, but remain nearly degenerate to each other. There-

fore, in addition to its spin, an electron in a Silicon quantum dot will contain a valley quantum number denoting whether it fills the $|+z\rangle$ or $|-z\rangle$ valley state. Microscopic features of the system introduce a small position-dependent valley splitting. We consider a double quantum dot in Silicon, which yields the following effective Hubbard Hamiltonian [57, 91, 92]:

$$\begin{aligned} H = &\sum_{s\in\{\uparrow,\downarrow\}}\sum_{j=1}^{2}\left(\tilde{\Delta}_j c^{\dagger}_{j,+z,s}c_{j,-z,s} + \tilde{\Delta}^{*}_j c^{\dagger}_{j,-z,s}c_{j,+z,s}\right) \\ &+ \frac{\epsilon}{2}(n_1 - n_2) + t_c \sum_{s\in\{\uparrow,\downarrow\}}\sum_{v=\pm z}\left(c^{\dagger}_{1,v,s}c_{2,v,s} + c^{\dagger}_{2,v,s}c_{1,v,s}\right) \\ &+ \sum_{j=1}^{2}\frac{U}{2}n_j(n_j-1) \end{aligned} \tag{2.1}$$

where $c_{j,v,s}$ is the second quantized annihilation operator for dot j, valley state v, and spin s, and where $n_j = n_{j,+z,\uparrow} + n_{j,+z,\downarrow} + n_{j,-z,\uparrow} + n_{j,-z,\downarrow}$. Here ϵ is the detuning between the two quantum dots, t_c is the tunneling constant between the two dots, and $\tilde{\Delta}_j$ determines the valley splitting of dot j. We define U to be the Coulomb energy difference between a dot occupied by two electrons, and a state with one electron occupying each dot. Thus we use a short-range Coulomb interaction term which is independent of valley states (including an explicit valley dependence in the interaction complicates the calculation, but does not affect our conclusion). Let $\tilde{\Delta}_j = \Delta_j e^{-i\phi_j}$, where $\Delta_j = |\tilde{\Delta}_j|$. Define $|j_{\pm}\rangle = (|j,+z\rangle \pm e^{i\phi_j}|j,-z\rangle)/\sqrt{2}$. Here $|j_{\pm}\rangle$ are the eigenstates of a single electron in a single dot j. Then for a single electron in a double-quantum-

dot, transforming H into the basis $\{|1_+\rangle, |1_-\rangle, |2_+\rangle, |2_-\rangle\}$ gives the following:

$$H = \begin{pmatrix} \epsilon/2 + \Delta_1 & 0 & t_+ & t_- \\ 0 & \epsilon/2 - \Delta_1 & t_- & t_+ \\ t_+^* & t_-^* & -\epsilon/2 + \Delta_2 & 0 \\ t_-^* & t_+^* & 0 & -\epsilon/2 - \Delta_2 \end{pmatrix} \tag{2.2}$$

where $t_\pm = (1 \pm e^{i\delta\phi})t_c/2$, and $\delta\phi = \phi_2 - \phi_1$. By this definition, t_+ is the tunneling coefficient between the valley ground states of both dots ($|1_+\rangle$ to $|2_+\rangle$), or between the valley excited states of both dots ($|1_-\rangle$ to $|2_-\rangle$). t_- is the tunneling coefficient between the valley ground state of one dot and the valley excited state of the other ($|1_+\rangle$ to $|2_-\rangle$, or $|1_-\rangle$ to $|2_+\rangle$). Note that while the $|-z\rangle$ state can be redefined for a single dot to eliminate the corresponding ϕ_j, the phase difference between two dots $\delta\phi$ is a well-defined quantity. Eq. (2.2) is equivalent to the two-dot Hamiltonian given in Ref. [57] up to a constant energy shift. We emphasize that this Hubbard model Hamiltonian describes quantum dot qubit coupling in reasonably realistic situations [91, 92, 59].

2.3 Diagonalization of Hamiltonian

In order to determine the effects of valley degeneracy and splitting on the exchange coupling between two dots, we consider two electrons in this two-dot system, diagonalizing the resulting Hamiltonian. We do this separately for the case when the electrons form a spin triplet and when they form a spin singlet.

2.3.1 Triplet Spin Configuration

Consider two electrons with a triplet spin configuration. Then due to the Pauli exclusion principle, the electrons must occupy different orbital or valley states. We will assume that $U \gg t_c, \Delta_j, \epsilon$, as the short-range Coulomb interaction energy is the largest energy scale in the system. Then there are four low energy states: $|1_+2_+\rangle$, $|1_+2_-\rangle$, $|1_-2_+\rangle$, and $|1_-2_-\rangle$ (note that because we are working entirely within the triplet subspace, we denote states only by their orbital and valley parts with the understanding that the spin part forms a triplet; explicit definitions of these states are given in Appendix A). These states couple via tunneling to the two high energy states $|1_+1_-\rangle$ and $|2_+2_-\rangle$, where the electrons occupy both valley states in a single dot. Perturbation theory to first order in U^{-1} gives the following Hamiltonian for the four lowest-energy states after including the effects of coupling to the two high energy states:

$$H_T = \begin{pmatrix} \Delta_1 + \Delta_2 - \frac{2|t_-|^2}{U} & \frac{t_- t_+^* - t_+ t_-^*}{U} & \frac{t_+ t_-^* - t_- t_+^*}{U} & \frac{2|t_-|^2}{U} \\ \frac{t_+ t_-^* - t_- t_+^*}{U} & \Delta_1 - \Delta_2 - \frac{2|t_+|^2}{U} & \frac{2|t_+|^2}{U} & \frac{t_- t_+^* - t_+ t_-^*}{U} \\ \frac{t_- t_+^* - t_+ t_-^*}{U} & \frac{2|t_+|^2}{U} & -\Delta_1 + \Delta_2 - \frac{2|t_+|^2}{U} & \frac{t_+ t_-^* - t_- t_+^*}{U} \\ \frac{2|t_-|^2}{U} & \frac{t_+ t_-^* - t_- t_+^*}{U} & \frac{t_- t_+^* - t_+ t_-^*}{U} & -\Delta_1 - \Delta_2 - \frac{2|t_-|^2}{U} \end{pmatrix} \tag{2.3}$$

The details of the derivation of Eq. (2.3) are given in Appendix A. Note that to leading order in ϵ/U, the four low energy states are independent of ϵ. This is because ϵ only affects the energies of states where both electrons occupy the same dot, and these are already energetically separated from the other states by the large onsite Coulomb interaction strength U and hence do not contribute in the leading order. If ϵ is allowed to be of the same scale as U, as is done in some experiments to control the exchange interaction, then these results must be adjusted accordingly.

Specifically where U appears in the denominator of terms in Eq. (2.3) it must be replaced with $U \pm \epsilon$ depending on the which state introduces each term. However for the purpose of this work we will focus on the situation where $\epsilon \ll U$, as is the case in experiments which use barrier control of the exchange interaction. In order to further study the system dynamics, Eq. (2.3) must be fully diagonalized. Since this cannot be easily analytically done for arbitrary Δ_j and t_c, we instead consider two different limits for small and large Δ_j. In the limit where $\Delta_j \gg t_c^2/U$, the matrix in eq. (2.3) is already diagonalized to leading order in $t_c^2/U\Delta_j$, and the energies are given by its diagonal entries. In the limit where $\Delta_j \ll t_c^2/U$, diagonalizing Eq. (2.3) yields the following energies:

$$
\begin{aligned}
E_1 &= -\frac{4t_c^2}{U} \\
E_2 &= -|\tilde{\Delta}_1 + \tilde{\Delta}_2| \\
E_3 &= 0 \\
E_4 &= |\tilde{\Delta}_1 + \tilde{\Delta}_2| = \sqrt{\Delta_1^2 + \Delta_2^2 + 2\Delta_1\Delta_2 \cos\delta\phi}
\end{aligned}
\tag{2.4}
$$

The corresponding eigenstates are given by:

$$
\begin{aligned}
|\psi_1\rangle &= \frac{1}{\sqrt{2}t_c}\Big(t_- \,|1_+2_+\rangle - t_+ \,|1_+2_-\rangle + t_+ \,|1_-2_+\rangle - t_- \,|1_-2_-\rangle\Big) \\
|\psi_2\rangle &= \Big[\frac{(\Delta_2+\Delta_1)t_+}{2t_c|\tilde{\Delta}_1+\tilde{\Delta}_2|}\big(\,|1_+2_+\rangle + |1_-2_-\rangle\,\big) + \frac{(\Delta_2-\Delta_1)t_-}{2t_c|\tilde{\Delta}_1+\tilde{\Delta}_2|}\big(\,|1_+2_-\rangle + |1_-2_+\rangle\,\big) \\
&\qquad - \frac{1}{2t_c}\Big(t_+ \,|1_+2_+\rangle - t_- \,|1_+2_-\rangle + t_- \,|1_-2_+\rangle - t_+ \,|1_-2_-\rangle\Big)\Big] \\
|\psi_3\rangle &= \frac{1}{\sqrt{2}t_c|\tilde{\Delta}_1+\tilde{\Delta}_2|}\Big[(\Delta_2-\Delta_1)t_-\big(\,|1_+2_+\rangle + |1_-2_-\rangle\,\big) + (\Delta_2+\Delta_1)t_+\big(\,|1_+2_-\rangle + |1_-2_+\rangle\,\big)\Big] \\
|\psi_4\rangle &= \Big[\frac{(\Delta_2+\Delta_1)t_+}{2t_c|\tilde{\Delta}_1+\tilde{\Delta}_2|}\big(\,|1_+2_+\rangle + |1_-2_-\rangle\,\big) + \frac{(\Delta_2-\Delta_1)t_-}{2t_c|\tilde{\Delta}_1+\tilde{\Delta}_2|}\big(\,|1_+2_-\rangle + |1_-2_+\rangle\,\big)
\end{aligned}
$$

$$+\frac{1}{2t_c}\Big(t_+\left|1_+2_+\right\rangle - t_-\left|1_+2_-\right\rangle + t_-\left|1_-2_+\right\rangle - t_+\left|1_-2_-\right\rangle\Big)\Big] \tag{2.5}$$

2.3.2 Singlet Spin Configuration

We now repeat the same calculation for a pair of electrons in a singlet spin configuration. In this case, the same six orbital states as in the triplet case are present, with the addition of four doubly occupied states $|1_{+\Uparrow}\rangle$, $|1_{-\Uparrow}\rangle$, $|2_{+\Uparrow}\rangle$, and $|2_{-\Uparrow}\rangle$, since both electrons can occupy the same valley and orbital state. Like above, we apply perturbation theory in U^{-1}, and calculate the Hamiltonian for the four lowest energy states, yielding:

$$H_S = \begin{pmatrix} \Delta_1+\Delta_2-\frac{2|t_-|^2+4|t_+|^2}{U} & -\frac{2t_-t_+^*}{U} & -\frac{2t_+t_-^*}{U} & -\frac{2|t_-|^2}{U} \\ -\frac{2t_+t_-^*}{U} & \Delta_1-\Delta_2-\frac{2|t_+|^2+4|t_-|^2}{U} & -\frac{2|t_+|^2}{U} & -\frac{2t_-t_+^*}{U} \\ -\frac{2t_-t_+^*}{U} & -\frac{2|t_+|^2}{U} & -\Delta_1+\Delta_2-\frac{2|t_+|^2+4|t_-|^2}{U} & -\frac{2t_+t_-^*}{U} \\ -\frac{2|t_-|^2}{U} & -\frac{2t_+t_-^*}{U} & -\frac{2t_-t_+^*}{U} & -\Delta_1-\Delta_2-\frac{2|t_-|^2+4|t_+|^2}{U} \end{pmatrix} \tag{2.6}$$

The details of the derivation of Eq. (2.6) are again given in Appendix A. Diagonalizing this matrix in the limit where $\Delta_j \ll t_c^2/U$ gives the following energies:

$$\begin{aligned} E_1 &= 0 \\ E_2 &= -\frac{4t_c^2}{U} - |\tilde{\Delta}_1+\tilde{\Delta}_2| \\ E_3 &= -\frac{4t_c^2}{U} \\ E_4 &= -\frac{4t_c^2}{U} + |\tilde{\Delta}_1+\tilde{\Delta}_2| \end{aligned} \tag{2.7}$$

The corresponding singlet case eigenstates are precisely the same as for the triplet case given by Eq. (2.5). Note that E_2, E_3, and E_4 are less than the corresponding triplet energies; however, E_1 is greater than the corresponding triplet energy. In each case, the difference is $\pm J_0$, where $J_0 = 4t_c^2/U$ is the strength of the exchange interaction in an ideal system which does not have any valley degeneracy.

2.4 System Dynamics

We now investigate the dynamics of a system prepared in a specific initial state and allowed to evolve under the Hamiltonian for some time t. This is the coupled qubit dynamics under gate operation, which controls quantum computation. We show that when the initial state is not prepared with each electron in the same valley state, leakage between valley states will introduce error. If the valley splitting Δ_j is small, this error can occur even if all electrons are initialized in the valley ground states $|j_-\rangle$ if the phases ϕ_j differ from one another. We first examine the large valley-splitting limit where $\Delta_j \gg J_0$, followed by the small valley-splitting limit where $\Delta_j \ll J_0$.

2.4.1 Large Valley Splitting

When $\Delta_j \gg t_c^2/U$, the system dynamics is determined to leading order by the diagonal entries of Eqs. (2.3) & (2.6). The off-diagonal elements only affect the energies to order J_0^2/Δ_j. If the system is prepared in one of the valley eigenstates, there will be an effective exchange interaction $J_+ = 4|t_+|^2/U$ for valley states $|1_+2_+\rangle$ and $|1_-2_-\rangle$; and an effective exchange interaction $J_- = 4|t_-|^2/U$ for valley states $|1_+2_-\rangle$ and $|1_-2_+\rangle$. Thus to leading order in J_0/Δ_j, the presence

of energetically separated valley states does not affect the dynamics of the system as long as the initial state is a valley eigenstate.

Since valley eigenstates have trivial dynamics in this regime, we consider a system not initialized to a valley eigenstate, representing a situation where some valley error has occurred during initialization. In such a scenario, the time evolution of the system can give rise to spin-valley entanglement, which will propagate the error to the spin state of the system. Consider, for example, an initial state where qubit 1 starts in the $|1_{+\uparrow}\rangle$ state, but qubit 2 starts in the state $(|2_{+\downarrow}\rangle + |2_{-\downarrow}\rangle)/\sqrt{2}$. Then after some time t, the system will evolve to:

$$\begin{aligned} |\Psi(t)\rangle = &\frac{1}{2}|1_+2_+\rangle\Big(|T_0\rangle + e^{iJ_+t}|S\rangle\Big) \\ &+ \frac{1}{2}e^{it(2\Delta_2+\frac{J_+-J_-}{2})}|1_+2_-\rangle\Big(|T_0\rangle + e^{iJ_-t}|S\rangle\Big) \end{aligned} \tag{2.8}$$

where $|T_0\rangle$ and $|S\rangle$ are the triplet and singlet spin states respectively. Suppose for simplicity that $\phi_1 = \phi_2$, and thus $J_- = 0$ and $J_+ = J_0$. Then the system reaches a maximally entangled state when $J_0 t = (2k+1)\pi$ for integer k:

$$\begin{aligned} |\Psi\big(\frac{(2k+1)\pi}{J_0}\big)\rangle = &\frac{1}{\sqrt{2}}|1_+2_+\rangle|{\downarrow\uparrow}\rangle \\ &+ \frac{1}{\sqrt{2}}e^{(2k+1)\pi i\left(\frac{2\Delta_2}{J_0}+\frac{1}{2}\cos^2\frac{\delta\phi}{2}\right)}|1_+2_-\rangle|{\uparrow\downarrow}\rangle \end{aligned} \tag{2.9}$$

Because the electron in dot 1 was initialized in a valley eigenstate in this example, it remains in that state throughout the evolution of the system. Thus, the state at any particular point in time corresponds a point on each of two Bloch spheres which represent the combined spin state (singlet or triplet) and the valley state of the second electron. This is not a one-to-one correspondence,

as different entangled states can correspond to the same set of points; nevertheless, it is useful for visualizing the information stored in the spin and valley states and the entanglement between them.

In Fig. 2.1, we plot the path $|\Psi(t)\rangle$ traces on the two Bloch spheres. The path begins on the surface of both Bloch spheres, indicating that initial state is separable. As time evolves to $t = \pi/J_0$, the path spirals toward the center of both Bloch spheres, indicating maximal spin-valley entanglement. In general, spin-valley entanglement is detrimental to quantum information applications, since measuring the spin state without the ability to measure the corresponding valley state can result in a complete loss of qubit information. Thus it is imperative to initialize the system in valley eigenstates – otherwise, information will leak out unwittingly through spin-valley entanglement during the coupled qubit dynamical evolution.

2.4.2 Small Valley Splitting

We now consider a situation where the valley splitting is small compared to the exchange interaction strength. In this regime the dynamics is dictated by the states and energies in Eqs. (2.3), (2.5), and (2.6). Because the singlet and triplet spin configurations share the same valley eigenstates, there is an effective exchange interaction $\pm J_0$ depending on the specific valley states occupied. We show that unless the system is initialized with all electrons occupying the same valley state, that the time evolution of the coupled system will result in spin-valley entanglement. Initializing the system in this way is difficult due to the near-degeneracy of the valley states. Additionally, if the phase difference $\delta\phi$ between dots is nonzero, as is often the case, spin-valley entanglement will occur even if all electrons are initialized to their individual ground valley states.

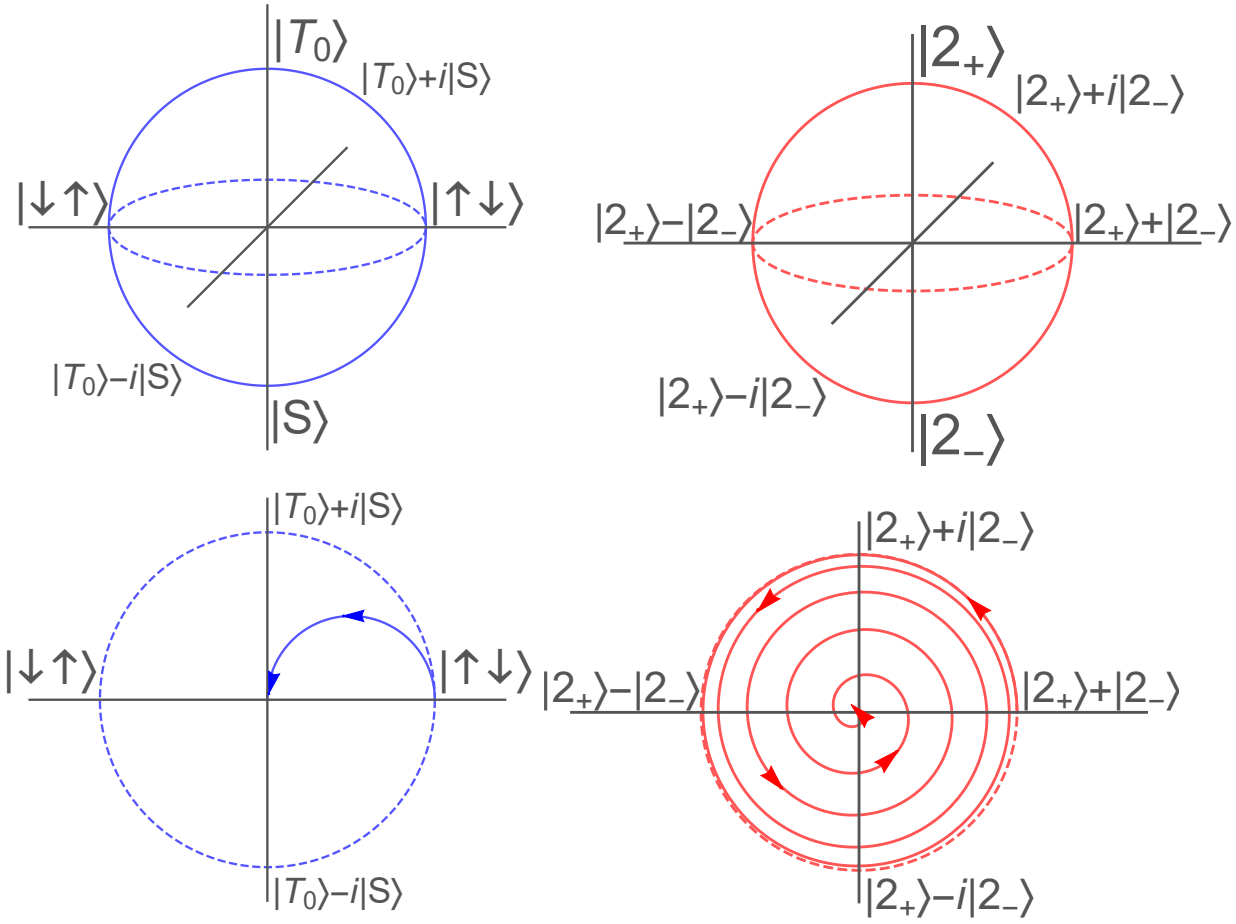

Figure 2.1: **Top:** Bloch sphere representation of the spin qubit in the singlet-triplet basis and valley qubit of the second dot (the first dot will always be in the valley state $|1_+\rangle$). **Bottom:** Time evolution of a state given by eq. (2.8) for t ranging from 0 to π/J_0, with $\Delta_2 = 5J_0$ and $\phi_1 = \phi_2$. The xy cross-sections of the Bloch spheres are plotted since the state stays entirely within the xy planes.

In fact, we are not aware of any experimental control capable of tuning the inter-valley phase difference $\delta\phi$, which we see as a potential problem requiring a resolution for Si spin qubits to work in a large circuit with many operational qubits.

To demonstrate the presence of spin-valley entanglement which can arise, consider an initial state $|1_{+\uparrow}2_{+\downarrow}\rangle$. For simplicity, suppose $\Delta_1 = \Delta_2 = \Delta$, and suppose there is a nonzero phase

difference $\delta\phi$. Then after some time t, the state will evolve to:

$$
\begin{aligned}
|\Psi(t)\rangle = \frac{t_-^*}{2t_c}\,|\psi_1\rangle\left(e^{iJ_0t}\,|T_0\rangle + |S\rangle\right) \\
+ \frac{t_+^*}{2\sqrt{2}t_c}\Bigg[\left(\frac{t_c}{|t_+|}-1\right)e^{i\frac{2|t_+|}{t_c}\Delta t}\,|\psi_2\rangle \\
+ \left(\frac{t_c}{|t_+|}+1\right)e^{-i\frac{2|t_+|}{t_c}\Delta t}\,|\psi_4\rangle\Bigg]\left(|T_0\rangle + e^{iJ_0t}\,|S\rangle\right)
\end{aligned}
\tag{2.10}
$$

By definition, $2|t_+|/t_c = 2\,|\cos\frac{\delta\phi}{2}|$, which equals $|\tilde{\Delta}_1+\tilde{\Delta}_2|/\Delta$ when $\Delta_1 = \Delta_2$. In Fig. 2.2 we plot the path on the Bloch sphere drawn out by total spin of $|\Psi(t)\rangle$. This path is independent of the value of Δ, and forms an ellipse confined to the xy-plane. The path given by the valley states, shown in Fig. 2.3, forms a rose curve which lies in the plane defined by $x + y\tan\delta\phi = 1$. Its projection into the xy-plane is a chord of the unit circle, the angle of which is independent of Δ and determined solely by $\delta\phi$. The exact shape of the rose curve is given by the quantity $\Delta\cos(\delta\phi/2)/J_0$.

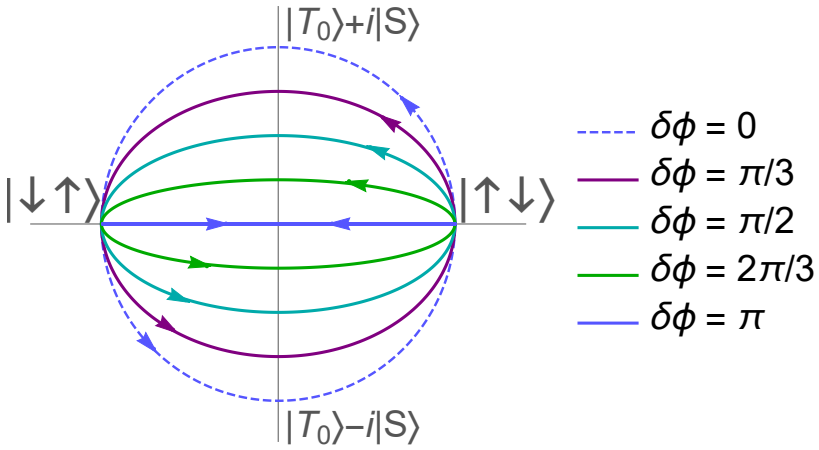

Figure 2.2: Time evolution of the spin state given by Eq. (2.10) for t ranging from 0 to $2\pi/J_0$ plotted for different values of $\delta\phi$. The xy cross-section of the Bloch sphere is shown since the path stays entirely within the xy plane. These paths are independent of Δ.

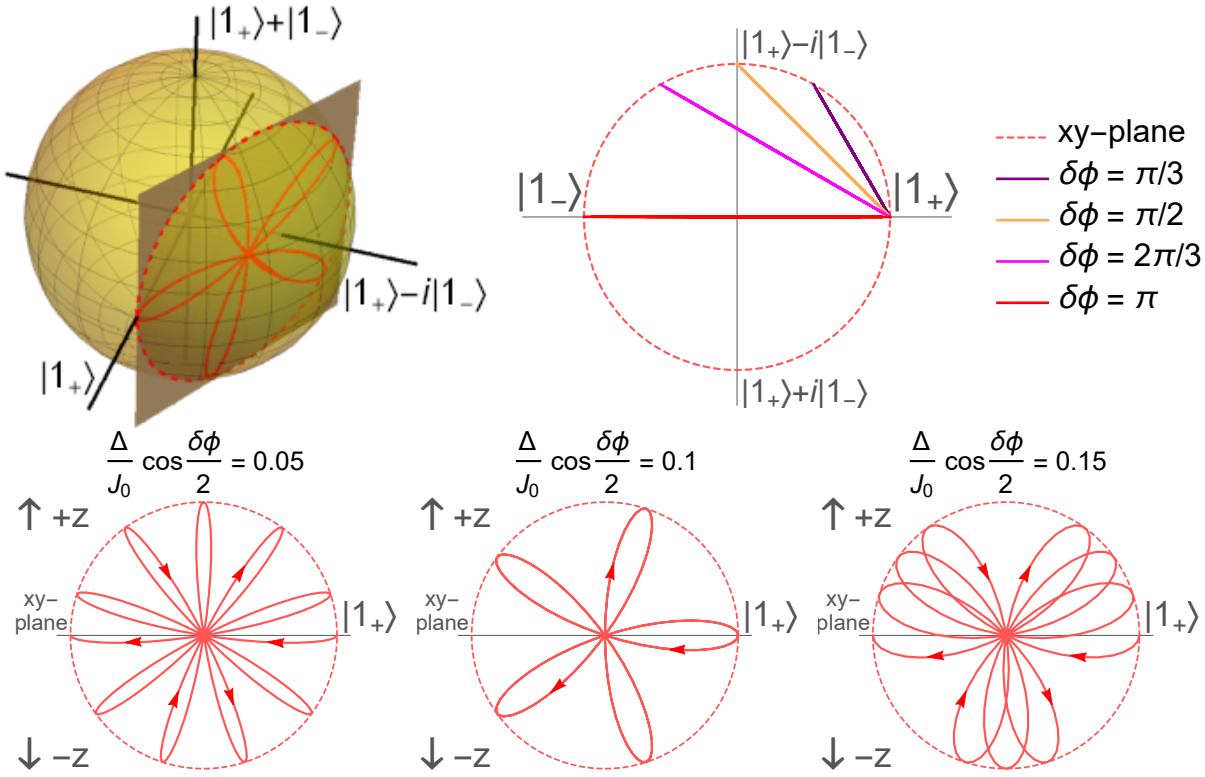

Figure 2.3: **Top Left:** Bloch sphere representation of the time evolution of the valley state of dot 1 in Eq. (2.10). The path forms a rose curve which lies within the plane given by $x+y\tan\delta\phi = 1$. **Top Right:** Projection of this path into the xy-plane, plotted for different values of $\delta\phi$. The plot for the valley state of dot 2 is identical, but reflected vertically. **Bottom:** Sample rose curves plotted for values of the quantity $\Delta\cos(\delta\phi/2)/J_0$ equal to 0.05, 0.1, and 0.15. The horizontal axis is the chord plotted in the top right figure, and the dashed circle is the intersection of the Bloch sphere with the plane $x + y\tan\delta\phi = 1$.

In general, $|\Psi(t)\rangle$ is an entangled state with two exceptions. $|\Psi(t)\rangle$ is separable if $\phi_1 = \phi_2$, as this makes $t_- = 0$ causing the first term in Eq. (2.10) to vanish. $|\Psi(t)\rangle$ also becomes separable when $t = k\pi/J_0$ (with integer k), as this causes the spin states in both terms of Eq. (2.10) to become identical. Conversely, $|\Psi(t)\rangle$ becomes a maximally entangled state when $\delta\phi = \pi$ and $J_0 t = (2k+1)\pi/2$, which causes Eq. (2.10) to simplify to the following:

$$\frac{1}{2\sqrt{2}}\Big(|1_+2_+\rangle - |1_-2_-\rangle\Big)\Big(i^{2k+1}|T_0\rangle + |S\rangle\Big) + \frac{1}{2\sqrt{2}}\Big(|1_+2_+\rangle + |1_-2_-\rangle\Big)\Big(|T_0\rangle + i^{2k+1}|S\rangle\Big) \tag{2.11}$$

It is instructive to consider the probability of recovering the initial spin state $|\uparrow\downarrow\rangle$ when measuring the spin of $|\Psi(t)\rangle$ after some time (leaving the valley state unmeasured). From Eq. (2.10), this probability is found to be given by:

$$P\big(\,|1_{+\uparrow}2_{+\downarrow}\rangle \rightarrow |\uparrow\downarrow\rangle\,\big) = \frac{1}{2}\big(1+\cos J_0 t\big) \tag{2.12}$$

This is precisely the same measurement probability as would result from time evolution in an "ideal" one-valley system. Differences occur when measuring in a different basis; for example the probability of obtaining the state $(|\uparrow\downarrow\rangle + i\,|\downarrow\uparrow\rangle)/\sqrt{2}$ is given by:

$$P\Big(\,|1_{+\uparrow}2_{+\downarrow}\rangle \rightarrow \frac{|\uparrow\downarrow\rangle + i\,|\downarrow\uparrow\rangle}{\sqrt{2}}\Big) = \frac{1}{2} - \frac{1}{2}\cos^2\frac{\delta\phi}{2}\sin J_0 t \tag{2.13}$$

If $\phi_1 = \phi_2$, meaning the two electrons start in the same valley states, then Eq. (2.13) reduces to $(1-\sin J_0 t)/2$, which is the same result as would be given by an ideal system. However if $\delta\phi = \pi$, then the two electrons start in opposite valley states, and Eq. (2.13) reduces to $P = 1/2$, independent of time. In this case when $J_0 t = (2k+1)\pi/2$, the probability outcome of measuring the spin in any basis gives $1/2$, as the spin state is maximally entangled with the valley state.

Despite the difference between Eq. (2.13) and the ideal case, spin-valley entanglement is difficult to observe in a system of two quantum dots. This is because it is difficult to directly measure in the basis containing the state $(|\uparrow\downarrow\rangle + i\,|\downarrow\uparrow\rangle)/\sqrt{2}$. Generally, if a quantum algorithm would require such a measurement, the measurement would be performed by applying a $\sqrt{SWAP}$ gate and then measuring in the z basis, which in an ideal system would produce the same result. However, $\sqrt{SWAP}$ gates are performed via the exchange interaction, which can disentangle a

spin-valley entangled state. In fact, for two qubits, as long as states are initialized and measured in the z-basis, valley splitting will not affect the measurement probability to first order in Δ/J_0. This is because the eigenstates given by Eq. (2.5) simultaneously diagonalize both the triplet and singlet Hamiltonians, Eqs. (2.3) and (2.6). Additionally, the energy difference between the corresponding triplet and singlet energies, Eqs. (2.4) and (2.7), is $\pm J_0$ for every eigenstate. Simply measuring in the z-basis cannot distinguish between rotations by $+J_0$ or $-J_0$.

One possible way to make such a distinction between rotations is the following. Start with a state $|\psi_1\rangle$, and perform a partial rotation (perhaps $2\pi/3$) via the exchange interaction J_0. Then allow $|\psi_1\rangle$ through some method to be transformed to any of the other states $|\psi_2\rangle$ through $|\psi_4\rangle$. One way in which this might happen is to let the system precess under the valley splitting, but with no exchange interaction present (note that in this case $\Delta \ll J_0$ does not hold). Finally, complete the initial rotation from the first step. In an ideal one-valley case, the system will have undergone one complete rotation. However, in a system with valley splitting, the last part of the rotation will be in the opposite direction as the first part, and thus will not form a complete rotation. This will affect the measurement probabilities in the z-basis. However, it is not possible to complete the second step (rotating $|\psi_1\rangle$ into $|\psi_2\rangle$) in a system of two qubits while keeping $\Delta \ll J_0$ without adding additional terms to the Hamiltonian.

2.5 Observing Valley Effects in 4-Qubit Systems

In the previous discussion, we demonstrated that despite the spin-valley entanglement that occurs, the measurement probabilities in the $\{\uparrow, \downarrow\}$ basis would be unaffected by the presence of valley states in a two-dot system. However, we now show that in a 4-dot system this is no longer

the case. We do this by giving two examples of sequences of operations which will result in a different measurement probability in a two-valley system than the same operations would in an ideal one-valley system.

Consider the fully degenerate case where $\Delta_1 = \Delta_2 = 0$ (exactly the same sequences apply when Δ_j are nonzero, but we consider the degenerate case for the sake of simplicity). Time evolution of the exchange interaction can be used to perform $\sqrt{SWAP}$ gates which swap both the spin and valley states of two electrons in adjacent dots. Consider an array of four quantum dots prepared in the initial state $|\uparrow_-\downarrow_+\uparrow_+\downarrow_-\rangle$ (this state is equivalent to $|\uparrow_+\downarrow_+\uparrow_+\downarrow_+\rangle$ where the phases $\phi_1 = \phi_4 = \pi$). Because the phases of Δ_j are not easy to control, the phases ϕ_j and initial valley states of each electron are relatively random, and thus there is no way to ensure that the system begins in the correct valley states. Thus, initial states like what we consider are likely to occur, and as we shall show, will lead to errors in the computation. In this example we only consider states with one electron confined to each dot, and therefore omit the dot numbers in our notation for the sake of notational brevity. Now perform the following operations to obtain $|\Psi_{\text{valley}}\rangle$:

$$\begin{aligned} |\Psi_{\text{valley}}\rangle = &\sqrt{SWAP_{23}}\sqrt{SWAP_{12}}\sqrt{SWAP_{34}} \\ &\times \sqrt{SWAP_{23}}\,|\uparrow_-\downarrow_+\uparrow_+\downarrow_-\rangle \end{aligned} \tag{2.14}$$

This sequence of gates is depicted in Fig. 2.4. Then $|\Psi_{\text{valley}}\rangle$ can be explicitly obtained, and is given by:

$$|\Psi_{\text{valley}}\rangle = \frac{1}{4}\Big[\,|\uparrow_+\uparrow_-\downarrow_+\downarrow_-\rangle - i\,|\uparrow_+\uparrow_-\downarrow_-\downarrow_+\rangle$$

$$
\begin{aligned}
&+ 2i\,|\uparrow_-\uparrow_+\downarrow_+\downarrow_-\rangle + |\uparrow_-\uparrow_+\downarrow_-\downarrow_+\rangle - |\uparrow_+\downarrow_-\uparrow_-\downarrow_+\rangle \\
&- i\,|\uparrow_+\downarrow_+\uparrow_-\downarrow_-\rangle - i\,|\uparrow_-\downarrow_-\uparrow_+\downarrow_+\rangle + |\downarrow_+\uparrow_-\downarrow_-\uparrow_+\rangle \\
&- i\,|\downarrow_+\downarrow_-\uparrow_-\uparrow_+\rangle + |\uparrow_-\downarrow_-\downarrow_+\uparrow_+\rangle + i\,|\uparrow_-\downarrow_+\downarrow_-\uparrow_+\rangle \\
&+ i\,|\downarrow_+\uparrow_-\uparrow_+\downarrow_-\rangle + |\downarrow_+\uparrow_+\uparrow_-\downarrow_-\rangle \Big]
\end{aligned} \tag{2.15}
$$

From this state, we calculate the measurement probability of the second dot being measured to be spin up, obtaining $P(2_\uparrow) = 5/8$. Now consider the ideal one-valley case, where the same set of operations are performed on a system of four spins in the same initial spin configuration. Then the resulting state $|\Psi_{\text{ideal}}\rangle$ will be given by:

$$
\begin{aligned}
|\Psi_{\text{ideal}}\rangle = \frac{1}{4}\Big[&(2+i)\,|\uparrow\uparrow\downarrow\downarrow\rangle - (1+2i)\,|\uparrow\downarrow\uparrow\downarrow\rangle + |\downarrow\uparrow\downarrow\uparrow\rangle \\
&- i\,|\downarrow\downarrow\uparrow\uparrow\rangle + (1+i)\,|\uparrow\downarrow\downarrow\uparrow\rangle + (1+i)\,|\downarrow\uparrow\uparrow\downarrow\rangle \Big]
\end{aligned} \tag{2.16}
$$

In the ideal case, the probability of measuring the second spin to be up is $P(2_\uparrow) = 1/2$, which is different from the case above where two valley states are present. This discrepancy arises from the fact that in the presence of valley states, there is a distinction between certain states that would be considered identical in the ideal case (e.g. $|\uparrow_+\uparrow_-\downarrow_+\downarrow_-\rangle$ and $|\uparrow_-\uparrow_+\downarrow_-\downarrow_+\rangle$). This distinction prevents constructive or destructive interference between the states, which influences the final measurement probabilities (in the ideal case both states are $|\uparrow\uparrow\downarrow\downarrow\rangle$ so their amplitudes should add together). This may have important implications for Si qubits. In order to perform correct calculations, all dots must be initialized to the same valley state, and the opposite valley state should be considered a leakage state. The presence of a phase difference between dots

$\delta\phi$ (leading to a t_- term) also introduces leakage into the system. However, the leakage states behave almost like the ideal states for small systems, and in fact they are indistinguishable for systems of only two dots, as we have shown in the previous section. This makes errors resulting from leakage difficult to detect in small systems and small gate sequences. Thus fidelities of two-qubit gates measured in two-qubit systems may be measured as higher than their true value in multiqubit circuits, because these measurements cannot account for leakage into other valley states without applying a larger sequence of gates such as that of Eq. (2.14) to a larger number of dots.

The sequence of gates given in Eq. (2.14) is a short sequence of gates which yields a different measurement outcome in an ideal system than in a system with multiple valley states. This effect is present for any initial state where the electrons with the same spin do not all have the same valley state. Note that the initial state is dependent on the values of ϕ_j, and the only way to control them is by controlling the valley phase. In Fig. 2.5 we plot the measurement probability of $|2_\uparrow\rangle$ versus the value of ϕ_4, with $\phi_1 = \phi_2 = \phi_3 = 0$. When ϕ_4 also equals 0, the initial valley states of all electrons are the same, and the measurement probability is the same as in the ideal case. As ϕ_4 varies away from 0, the measurement probability increases. This sequence of gates can be used to demonstrate the presence of valley-induced error, as if the state $|2_\uparrow\rangle$ is measured with probability greater than 1/2, this is a result of valley-induced error. However this sequence of gates cannot be used to show the converse in noisy systems, because if $|2_\uparrow\rangle$ is measured with probability 1/2, the result is indistinguishable from noise-induced decoherence.

We now give a different sequence of gates which has a measurement probability of 1 in the ideal case, and thus can be used to demonstrate initialization of electrons in the same valley state. Consider a ring of 4 quantum dots with the initial state $|\uparrow_-\downarrow_+\uparrow_+\downarrow_-\rangle$. Perform the following

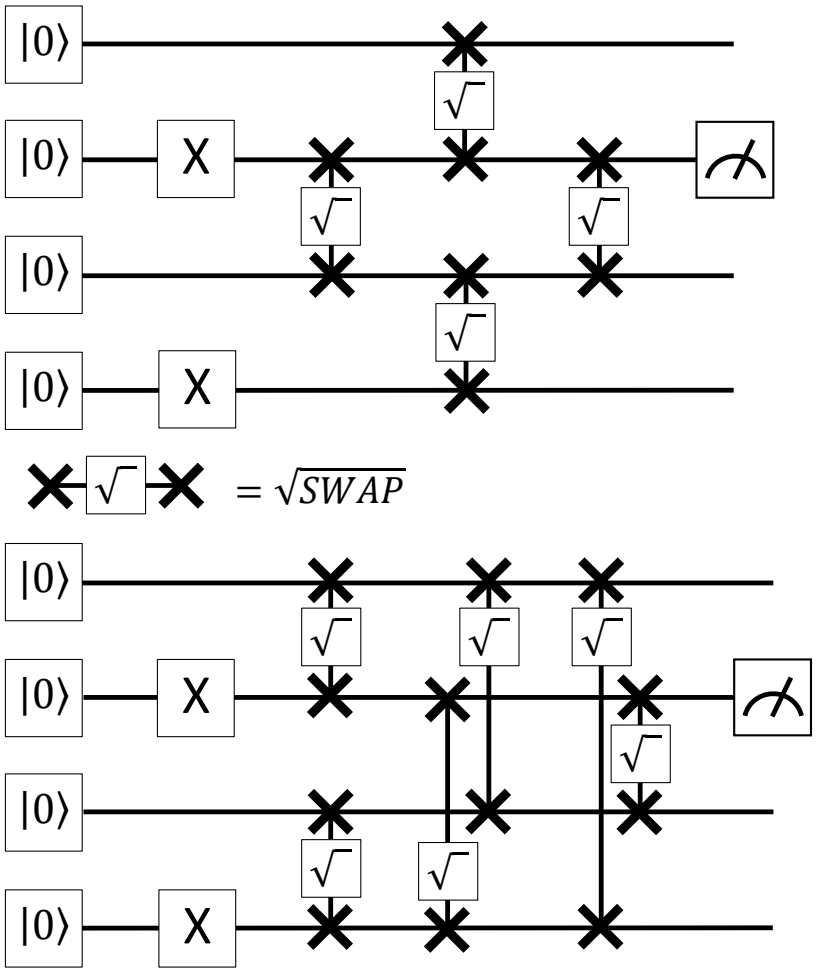

Figure 2.4: Quantum circuit depicting the sequence of gates in Eq. 2.14 (top) and Eq. 2.17 (bottom).

sequence of $\sqrt{SWAP}$ gates:

$$|\Psi_{\text{valley}}\rangle = \sqrt{SWAP_{23}}\sqrt{SWAP_{14}}\sqrt{SWAP_{13}}$$
$$\times \sqrt{SWAP_{24}}\sqrt{SWAP_{12}}\sqrt{SWAP_{34}}\,|\uparrow_-\downarrow_+\uparrow_+\downarrow_-\rangle \tag{2.17}$$

For this sequence of gates, $|\Psi_{\text{valley}}\rangle$ is given by:

$$|\Psi_{\text{valley}}\rangle = \frac{1}{4}\Big[\,|\uparrow_+\uparrow_-\downarrow_-\downarrow_+\rangle - |\uparrow_-\uparrow_+\downarrow_+\downarrow_-\rangle$$

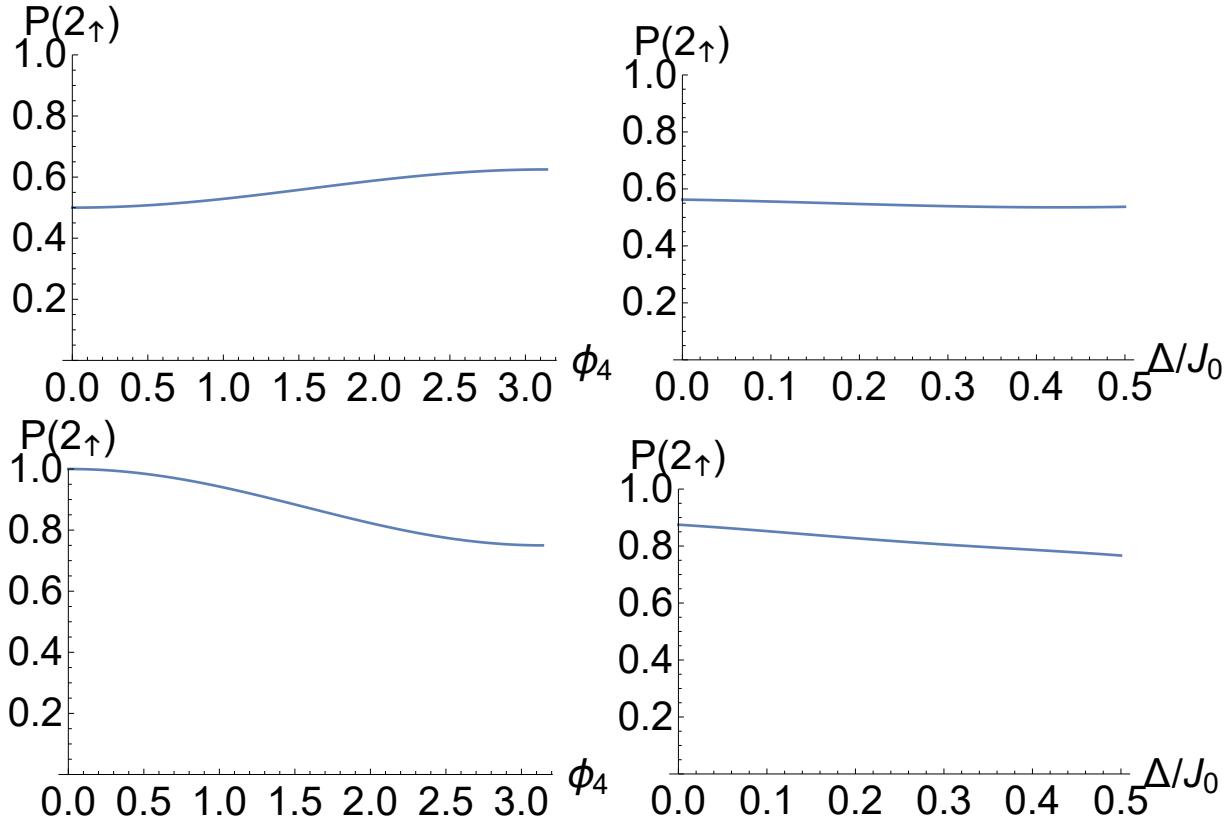

Figure 2.5: Probability that dot 2 will be measured in spin state ↑ after a sequence of gates is applied to the initial state $|\uparrow_+\downarrow_+\uparrow_+\downarrow_+\rangle$, with $\phi_1 = \phi_2 = \phi_3 = 0$. **Top Left:** The gate sequence is given by Eq. (2.14) and $\Delta = 0$. **Top Right:** The gate sequence is given by Eq. (2.14) and $\phi_4 = \pi/2$. **Bottom Left:** The gate sequence is given by Eq. (2.17) and $\Delta = 0$. **Bottom Right:** The gate sequence is given by Eq. (2.17) and $\phi_4 = \pi/2$.

$$
\begin{aligned}
&+ |\downarrow_+\downarrow_-\uparrow_-\uparrow_+\rangle - |\downarrow_-\downarrow_+\uparrow_+\uparrow_-\rangle + |\uparrow_+\downarrow_-\downarrow_+\uparrow_-\rangle \\
&- |\uparrow_-\downarrow_+\downarrow_-\uparrow_+\rangle - |\downarrow_+\uparrow_-\uparrow_+\downarrow_-\rangle + |\downarrow_-\uparrow_+\uparrow_-\downarrow_+\rangle \\
&+ 2\,|\downarrow_+\uparrow_+\downarrow_-\uparrow_-\rangle + 2\,|\downarrow_-\uparrow_-\downarrow_+\uparrow_+\rangle\Big]
\end{aligned}
\tag{2.18}
$$

The corresponding ideal state $|\Psi_{\text{ideal}}\rangle$ is simply:

$$
|\Psi_{\text{ideal}}\rangle = |\downarrow\uparrow\downarrow\uparrow\rangle \tag{2.19}
$$

With this sequence of gates, the ideal single-valley case will have measurement probabilities of 100%, but the corresponding two-valley case will only have corresponding measurement probabilities of 75%, simulating an unknown apparent decoherence although it arises simply from the inevitable spin-valley entanglement which is omnipresent in the multi-valley qubits. In Fig. 2.5 we again plot the measurement probability of $|2_\uparrow\rangle$ versus the value of ϕ_4 for this new gate sequence. When $\phi_4 = 0$, the measurement probability is 100% matching the ideal case, but for nonzero ϕ_4 the measurement probability decreases, allowing the adverse effects of spin-valley entanglement to be detected. We also plot the measurement probability as a function of Δ, showing that the effective decoherence increases as Δ increases, provided that Δ still stays within the regime $\Delta \ll J_0$.

2.6 Conclusion

We used an effective Hubbard model to investigate the effects of valley states in Silicon quantum dots in the context of exchange gate operations in multiqubit systems at zero temperature. We first considered a system of two exchange-coupled quantum dots, and determined the eigenstates and energies for both the singlet and triplet spin configurations to leading order in t_c^2/U. We considered the limits where $\Delta \gg J_0$ and $\Delta \ll J_0$, and found that in both cases the singlet and triplet spin configurations share the same eigenstates, though their energies differ. When the valley splitting is large, any state not initialized to valley eigenstates will lead to spin-valley entanglement as the system evolves. However, as long as the valley splitting is large and the system is initialized to the valley ground state, the evolution of the system will not be affected to leading order in Δ/J_0. Thus valley degrees of freedom are not problematic for exchange gate

operations as long as the valley splitting Δ is sufficiently large. For small valley splitting or completely degenerate valley states, spin-valley entanglement will arise any time the electrons are not initialized to the same valley state. Without the ability to perform valley state measurements, spin-valley entanglement will obfuscate any information stored in the electron spin states, making it impossible to perform quantum computations in such a state. For a two qubit system with $\Delta \ll J_0$, if all spins are initialized in z-eigenstates and measured in the z-basis, then the resulting measurement probabilities will be the same as an ideal single-valley system. However, this does not extend to systems with more qubits, as spin-valley entanglement can introduce errors despite states being initialized and measured in the z-basis. This means that two-qubit gate fidelities measured by performing a single gate in a two-qubit system will give deceptively high fidelity results, because the presence of valley states does not affect the fidelity measurement even though it can affect operations in systems with more qubits. To demonstrate robustness to spin-valley entanglement without the ability to measure valley states themselves requires a longer series of gates in a system with more qubits. We emphasize that our use of the Hubbard model is not an approximation here since the coupled spin qubit system is indeed equivalent to the Hubbard model where the Hubbard interaction U is simply related to the exchange coupling J_0 between the dots through $U = t_c^2/J_0$, where t_c is the inter-dot hopping energy from wavefunction overlap. Our fundamental finding of an apparent quantum leakage (or effective decoherence) due to spin-valley entanglement is also independent of additional complications arising from varying exchange couplings and/or inter-dot hopping through the circuit– all they do is to complicate the expressions for the leakage, but the basic physics of spin-valley entanglement remains the same.

We note that our considerations on spin-valley entanglement apply equally well to all-exchange gate operations considered in Ref. [41]– anytime the inter-dot exchange coupling is

used to carry out gate operations, the valley-spin entanglement (and potential decoherence to valley states) studied in this work becomes relevant. Right now, the Si qubit platforms have rather small exchange coupling, and the problem discussed in this work is most likely not crucial to the current generation of few qubit systems with rather small exchange coupling values. But faster gate operations in multiqubit circuits will necessitate larger exchange coupling strength in the future, making our dynamical consideration relevant as one must ensure that not only is the valley splitting much larger than the electron temperature in the qubits, it is also much larger than the inter-dot exchange coupling used in the gate operations.

We now critically discuss some aspects and approximations of our theory. First and foremost, the subtle physics of valley splitting on two-qubit operations we point out in this work is completely independent of the already well-known problem associated with valley occupancy in Si qubits which already necessitates having large valley splittings compared with temperature T. For our physics, the valley splitting must be much larger than the inter-qubit exchange coupling J_0. Since the current experimentally relevant values of J for existing Si qubits are rather small, often comparable to (or even smaller than) T itself (although T and J are completely independent parameters and have nothing to do with each other), it may seem that our theory is not particularly germane to the current experimental Si qubit activity since the condition for the valley splitting Δ being larger than J appears to be automatically satisfied in current devices by having splitting larger than temperature. This conclusion, however, may be misleading for two reasons. First, the functional dependence of 'errors' introduced by valley spitting in the two situations are very different: temperature enters exponentially through the thermal occupancy factor $e^{-\Delta/T}$ adversely affecting single qubit operations whereas, by contrast, as we show in the current work, the two-qubit fidelity is adversely affected algebraically by J_0/Δ. Thus, the same value of Δ in

a device may suffice to satisfy the condition $e^{-\Delta/T} \ll 1$ but completely fail to satisfy $J_0/\Delta \ll 1$. This means that for a given set of values of Δ, T, and J_0 for a device, it is possible for the valley splitting to be large for high-fidelity single qubit operations (i.e. exponentially low thermal occupancy) and low fidelity two-qubit operations (as described in our current work) because of not-so-small values of J_0/Δ. Considering a device with T = 25 mK, Δ = 300 mK, J_0 = 10 mK, which are typical numbers, we get $e^{-\Delta/T} \sim 6 * 10^{-6}$ and $J_0/\Delta \sim 3 * 10^{-2}$, implying that while valley splitting induced single qubit thermal occupancy errors are well below the quantum error correction threshold, the corresponding two-qubit errors discussed in the current work are not small enough., being 4 orders of magnitude larger than the one qubit error. The second reason is that in a many-qubit device, it is always possible to have a particular qubit with a valley splitting which is not very large (particularly since there is no automatic way of guaranteeing large valley splitting in a device), which, as we establish in the current work, will lead to two-qubit errors which will not directly show up in two-qubit operations. Thus, there is simply no way to ensure that the problem we describe in the current work is not lurking in a multiqubit device without going through the full multiqubit characterization as we discuss in this chapter. We also emphasize that the eventual Si quantum computer will have millions of qubits, and the problem we have discovered may become crucial in such a large device. It is much better to be aware of this problem now so that the condition $\Delta \gg J_0$ is satisfied everywhere in order to avoid unknown two-qubit errors.

The second issue we discuss is our use of the Hubbard model in Eq. (2.1), which may appear to be a drastic approximation since real Si qubits do not obey the Hubbard model precisely quantitatively – the applicability or not of the Hubbard model for Si qubits has been discussed in Ref. [91]. This is, however, not a limitation of the theory at all since the only aspect of the

Hubbard model relevant for our theory is the fact that it leads to an inter-dot exchange coupling ($J_0 = 4t_c^2/U$), and in the end, J_0 is the parameter to be compared with the valley splitting Δ to decide whether one is in the large ($\Delta \gg J_0$) or small valley splitting regime. The Hubbard model allows a straightforward transformation between electrons in the quantum dots and localized Heisenberg spins as 2-level qubit systems, and it enables a full analytical treatment of the problem. The fully analytical nature of our theory is a particularly attractive feature since it makes the theory universally applicable to all Si devices in different laboratories– all one needs to do is to carry out numerical simulations for the specific Si structure to obtain the inter-qubit exchange coupling. Thus, the Hubbard model description makes our theory universal, and specific devices can be adapted to the theory by calculating the exchange coupling realistically which must be done individually for each device.

The most obvious mitigation of the valley degeneracy induced exchange operation problem described in this work is to have the valley splitting being much larger than the exchange coupling and initialization of all dots in the lower energy ground valleys, which is guaranteed if the exchange coupling strength is very small. But for faster exchange gate operations with larger exchange coupling, other mitigation measures may be necessary. One possibility is carrying out measurements as a function of different values of J, enabling a characterization of whether two-qubit exchange operations are problematic or not because of small valley splitting. Spin-valley entanglement could be directly observed in a two-qubit system if sufficient control over the exchange interaction is available such that a time dependent pulse $J(t)$ can be performed where some part of the pulse $J(t)$ is much smaller than the valley splitting. Another possibility is measurements using different basis states which may be carried out under some type of random benchmarking protocols. Adding other terms to the Hamiltonian such as a magnetic field gradi-

ent may also allow potential spin-valley entanglement to be observed in a two-qubit system with large and constant J [93]. It may be that carefully crafted gate operations can avoid the entanglement problem altogether. Additionally, it may be possible to derive qubit encodings which are robust to valley effect. These are interesting directions and questions to address in future work. Our main purpose of this chapter is to alert the community that although it is absolutely necessary for valley splitting to be much larger than temperature in order to make sure that thermal occupancy of higher valley states does not compromise the qubit fidelity, this by itself is not sufficient as one must also worry about the relative magnitude of valley splitting and exchange coupling in order to ensure high-fidelity exchange gate operations even at zero temperature.

In this context it is encouraging that recent experimental work has had considerable success in consistently achieving large valley splittings [94, 95] although in a many qubit circuit whether each qubit has large splittings or not still must be determined individually, which makes it a challenge to scale up to a large qubit system, which is considered one of the key advantages of Si spin qubits. We conclude by emphasizing that although our work may not be of immediate relevance to the existing experimental Si qubit circuits mainly because of the few-qubit (1-4) nature of the current devices and their rather low values of exchange coupling, future Si circuits, which would hopefully compete with the many-qubit superconducting transmon circuits some day in the future, would have to incorporate the potential problem we have discovered.

Chapter 3: Nagaoka Ferromagnetism

3.1 Introduction

John Hubbard introduced the celebrated Hubbard model [58] as a minimal model to study ferromagnetism in narrow band itinerant electron systems such as Fe, Ni, and Co. The hope was that the minimal Hubbard model, with just one dimensionless interaction parameter U/t where U is the on-site interaction (arising from Coulomb repulsion) between two electrons with unlike spins and t is the nearest-neighbor tunneling associated with kinetic energy, would make the difficult problem of itinerant electron metallic ferromagnetism tractable and perhaps even exactly solvable. This early hope of the Hubbard model leading perhaps to an understanding of narrow band metallic ferromagnetism was echoed in other early publications also [96, 97]. After almost 60 years of extensive research, we still do not have a general solution to the Hubbard model (except under very restricted conditions, e.g., one dimensional, 1D, systems) and the Hubbard model has become the archetype underlying the whole subject of strongly correlated materials. In fact, large teams of computational physicists work on large computers with the single goal of trying to understand numerically the implications of the Hubbard model in various situations, and no clear signatures for ferromagnetic ground states in the Hubbard model have emerged from these extensive numerical calculations [98]. Perhaps the most ironic aspect of the Hubbard model is that it is now universally accepted to be an excellent model to study antiferromagnetism, local

moment formation, and Mott metal-insulator transition in narrow band lattice systems rather than as a model for metallic ferromagnetism as Hubbard originally dreamed of. Any ferromagnetism arising within the Hubbard model is fragile and is certainly limited to very narrow parameter ranges (i.e. band filling and the interaction strength U/t), and it is entirely possible that generic 2D and 3D ferromagnetic systems cannot be described by the Hubbard model at all.

One important early result in this context is the concept of Nagaoka ferromagnetism [62] which arises naturally in the 2D Hubbard model on square (and other bipartite) lattices under rather nongeneric and highly restrictive conditions (see, e.g. Refs. [63, 99, 100], and references therein). This is an exact result which asserts that the 2D Hubbard model doped by precisely one hole (i.e. one missing electron) away from the half-filling has full ferromagnetism of the whole system in the thermodynamic limit provided U is infinite. Since the half-filled 2D Hubbard model is surely not a ferromagnet at any interaction strength, the Nagaoka theorem appears pretty amazing in the sense that removing just one electron from the system drives the whole ground state completely ferromagnetic. The theorem derives from the kinetic constraint on the motion of a hole in the half-filled system in the infinite U limit, leading to the lowest energy state being the state of all the electrons becoming spin-polarized in order to minimize the kinetic energy in the strongly interacting limit (where double occupancy is not allowed). As an exact result Nagaoka ferromagnetism is valid only for U truly infinite. In practice, ferromagnetism still exists for U larger than some threshold value, and while this value threshold is reasonably small for small systems (as we show in our results), in the thermodynamic limit, this threshold becomes so large that Nagaoka's theorem will not actually apply to physical systems, which have a finite U. While Nagaoka ferromagnetism is of some theoretical significance because it is an exact result, it is of no consequence for any experimental situation since creating precisely one hole in

a thermodynamic system is obviously an impossible constraint (and the infinite interaction limit is unphysical as well). The very fragile nature of the proof underlying this theorem does not allow its generalization to a dilute density of holes around half-filling, and Nagaoka ferromagnetism in its original form [62] is unlikely to be observable experimentally in spite of its theoretical validity.

The question we address in the current work is the relevance of Nagaoka ferromagnetism in small finite 2D systems, which can be constructed by using semiconductor quantum dots with a few electrons in it. In such a system, with N electrons in M dots, the effective finite-size Nagaoka situation is easily achieved by tuning the system to having $N = M - 1$, assuming each dot to have one effective orbital energy level with two spin states. Such a scenario was recently achieved experimentally in Ref. [9], and signatures for ferromagnetism were observed. Our goal in the current work is to ask a general theoretical question on the existence or not of ferromagnetic ground states in small 2D plaquettes made of tunable semiconductor quantum dots: What experimentally accessible arrangements of a few coupled quantum dots ($\sim$4) with a few electrons would manifest stable ferromagnetic ground states? It turns out that this question can be answered analytically for several interesting quantum dot structures which are currently experimentally viable because of recent advances in control, engineering, and fabrication of coupled semiconductor quantum dots in the context of developing spin qubits [9, 11, 101, 102, 103, 104, 105, 106, 107].

It was pointed out 25 years ago [59, 60, 61] that semiconductor quantum dot arrays may be capable of simulating the Hubbard model in finite solid state systems searching for Mott transition and related strong correlation phenomena. Advances in materials growth and nanofabrication techniques finally made this idea practical in laboratory settings only in 2017 when Mott physics in the form of the predicted collective Coulomb blockade [59] was observed in a small linear array of coupled GaAs quantum dots emulating the Hubbard model [101]. There has been rapid

recent development in controlling small coupled quantum dot arrays in several laboratories [9, 11, 101, 102, 103, 104], and experimentalists can now study up to 4-9 dots with variable numbers of electrons per dot along with precise control of coherent electron tunneling between the dots. Our work, although purely theoretical, is inspired by these developments in the precise experimental control over small systems of coupled quantum dots. In particular, the recent experimental work from Delft [9] reporting the observation of Nagaoka ferromagnetism in a 2D square array of quantum dots has directly motivated our work although our emphasis is on the generality of the possible emergence of Nagaoka-type ferromagnetism in quantum dot arrays, not describing the observations in Ref. [9] which require a detailed numerical approach [108].

Electrons in quantum dots interact via the long-range Coulomb interaction, and hence our model is a generalized or extended Hubbard model which includes both on-site and inter-site Coulomb interaction. In addition, electrons in quantum dots could, in general, have distant neighbor hopping, not just nearest-neighbor hopping as in the minimal Hubbard model. We therefore include both nearest-neighbor and next-nearest-neighbor hopping in the theory. One other possible practical complication, which may be relevant to the experimental quantum dot arrays, is that each dot may have more than one relevant orbital level, making the system akin to an SU($2n$) Hubbard model where n is the number of orbitals ("quantum dot energy levels") playing a role in each dot [109]. In such a situation, the inter-site hopping process could involve inter-orbital hopping also. We neglect this complication and consider a purely SU(2) system with each dot having just two spin states, assuming the higher orbital levels in each dot to be reasonably high in energy. This is not an essential approximation, and is done to enable us to carry out our work completely analytically. In any case, the neglect of higher orbital levels is a well-defined and well-controlled theoretical approximation since this can always be achieved experimentally by making each dot

confinement potential sufficiently deep (and keeping the temperature sufficiently low) so that only the lowest orbital state in each dot is operational in the physics of the system. The finite size Hubbard model we consider is therefore a generalization of the minimal Hubbard model, and includes both distant neighbor hopping and inter-site Coulomb interaction, but no higher orbital physics.

We also should mention here that although the quantum ferromagnetism discussed in our work is adiabatically connected to the Nagaoka ferromagnetism in the half-filled infinite-U Hubbard model with one hole, there are important differences to keep in mind in order to avoid confusion and misunderstanding. First, our system is a finite 2D plaquette (Fig. 3.1) with 4 dots and 3-5 electrons whereas Nagaoka ferromagnetism is obviously a thermodynamic result. Second, in our system the interaction could be large, but never infinite, since the infinite-U limit is unphysical for actual quantum dots. Third, our model being semi-realistic includes distant neighbor hopping and interaction, so we are considering a generalized and extended Hubbard model. Fourth, our inter-site tunneling (i.e. the hopping parameter t) matrix element is negative, not positive as in the original work of Nagaoka. Fifth, because of the small size of our system, one missing electron (i.e. a hole) corresponds to a finite hole density in contrast to the Nagaoka situation where the hole density is by definition zero (e.g. 3 electrons in a 2D square with 4 dots at the corners correspond to one hole in the system, but the hole density is 25%). Thus, the ferromagnetism we consider should perhaps be better called "Nagaoka-type ferromagnetism" rather than just Nagaoka ferromagnetism. The important point is, however, the fact that the quantum ferromagnetism we predict can be observed experimentally in already existing semiconductor quantum dot arrays.

The rest of this chapter is organized as follows. In sec. 3.2, we investigate Nagaoka-type

ferromagnetism by finding the ground states of three electrons in 4-dot plaquettes of various geometries. In sec. 3.3, we repeat the calculations for a half-filled band (4 electrons) for the same geometries. In sec. 3.4, we look at the case of one hole in a 5-dot ring, and we summarize our results in sec. 3.5. The contents of this chapter have been published in Ref. [110].

3.2 Three Electrons in Four Dots

3.2.1 General Model And Method

3.2.1.1 Hamiltonian

We consider a single-band Hubbard model with four sites labeled 1 - 4. We define U_0 to be the onsite interaction energy, V_{ij} to be the Coulomb interaction energy between electrons at sites i and j, t_{ij} to be the hopping term between sites i and j. Because we are considering a single band model, we are assuming that the difference in orbital levels is much larger than the other relevant energy levels, namely U_0, an assumption that may or may not be true in practice. Then the Hamiltonian is given by:

$$H = \sum_{i \neq j, \alpha} t_{ij}\, c^{\dagger}_{i,\alpha} c_{j,\alpha} + \sum_{i} U_0\, n_{i\uparrow} n_{i\downarrow} + \sum_{i \neq j} \frac{V_{ij}}{2} n_i n_j \tag{3.1}$$

where $c_{i,\alpha}$ is the annihilation operator at site i with spin α. Nagaoka's theorem predicts ferromagnetism in systems with one hole in a half-filled band with certain geometries where Nagaoka's condition holds. The simplest of these systems are a triangle or square plaquette of three or four sites. However, of particular importance is the sign of the product of hopping elements around loops $t_{12}t_{23}t_{31}$. In order for the Nagaoka condition to hold, quantities of this

form must be positive; however, in reality, this sign is determined by the number of sites in the loop, and is negative for an odd number of sites. Thus a triangular plaquette with two electrons does not satisfy the Nagaoka condition, as must be the case since it is well known that the ground state of two electrons in any potential must necessarily be a singlet. Thus the addition of next nearest neighbor hopping terms (the dashed lines in fig. 3.1) break the Nagaoka condition and can potentially destroy ferromagnetism if strong enough. It is interesting to derive a condition on the relative strengths of the hopping terms that determines whether ferromagnetism exists. The fact that our hopping parameter is negative compared with the positive hopping used in the study of the traditional Nagaoka theorem may have implications which should be further investigated in future works. In fact, Nagaoka's original proof demands the positivity of the hopping parameter whereas our work shows that, at least for small system sizes, the theorem remains valid independent of the sign of hopping. In actual experimental systems, the sign of the hopping may not be known, but any theoretical modeling of the laboratory system would have definite signs of the hopping parameter, and our work is in some sense a generalization of the Nagaoka theorem to negative hopping.

We consider four different geometries with 4 quantum dots: a square, a rectangle, a linear array, and Y-shaped plaquette, all with and without diagonal hopping terms where applicable. We note that only the first two satisfy the Nagaoka condition, and only in the absence of the diagonal hopping, as discussed above. We define a to be the distance between nearest neighbors, along with $b > a$ in the case of the rectangle, and we define d to be the distance between next nearest neighbors in each respective geometry. We define V_r to be the Coulomb interaction energy between electrons separated by a distance r, and t_r be the magnitude of the hopping strength between dots separated by a distance r. U_0 will be the onsite interaction energy as defined above.

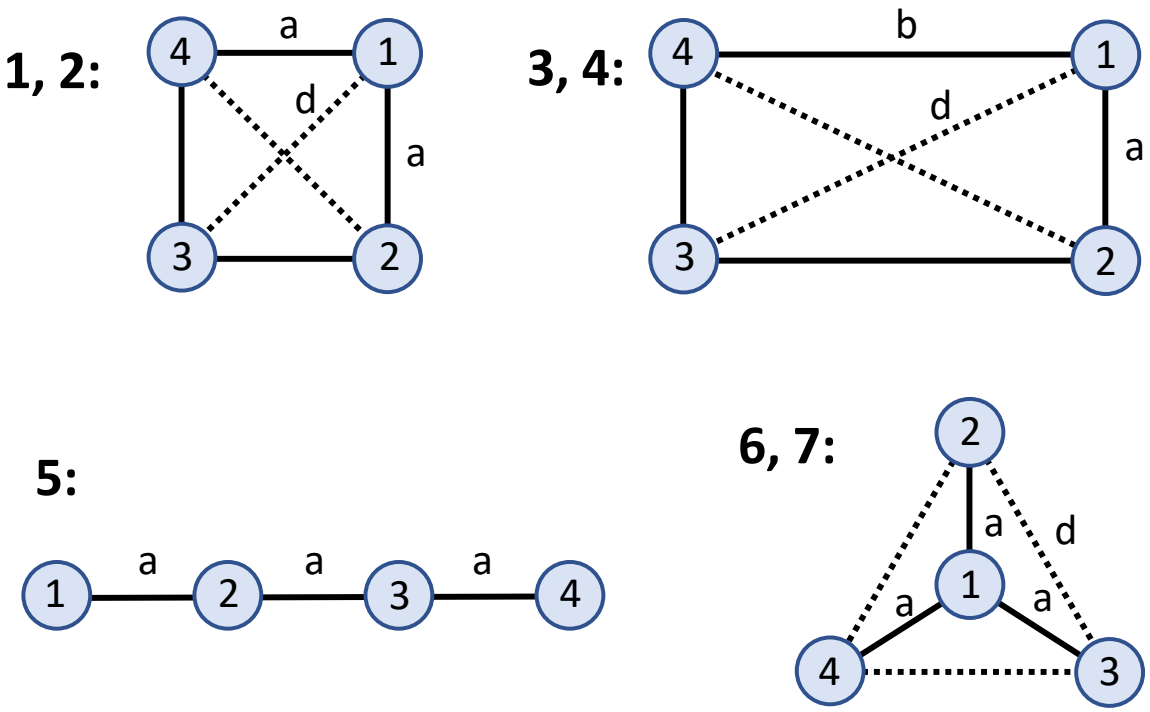

Figure 3.1: A depiction of the different 4-dot geometries studied in this work, numbered in bold according to the subsection numbers in which they are discussed. Solid lines depict nearest-neighbor hopping terms, and dashed lines next nearest neighbor hopping terms, which we consider in some cases. In all cases long-range Coulomb interactions are included.

The bare parameters V_r and U_0 are not important by themselves, but rather their differences are what affect the dynamics of the system, as a uniform shift in all these values will simply cause a constant shift in total energy, since the number of particles is conserved. Thus we will define new parameters U and V corresponding to the relevant energy differences, which vary for each geometry. We will also shift the total energy of the Hamiltonian by a constant such that the lowest energy configuration of electrons in the absence of tunneling is 0.

3.2.1.2 Spin 3/2 States

A system of three electrons can have either spin 1/2 or 3/2. To investigate the spin 3/2 states, we merely consider the case where all electrons are spin up, as all other states in the spin 3/2 quartet will be identical, aside from the value of S_z. We define the notation $|d_1 d_2 d_3 d_4\rangle$ to be the state where the electron filling of dot i is given by d_i, where $d_i \in \{0, \uparrow, \downarrow, \updownarrow\}$. Since the Pauli exclusion principle forbids two spin up electrons from occupying the same orbital state, there are four possible spin 3/2 states for each value of S_z. For $S_z = 3/2$, these are:

$$|\uparrow\uparrow\uparrow 0\rangle\,, \quad |\uparrow\uparrow 0\uparrow\rangle\,, \quad |\uparrow 0\uparrow\uparrow\rangle\,, \quad |0\uparrow\uparrow\uparrow\rangle \tag{3.2}$$

The Hamiltonian is then constructed in this basis and diagonalized to find the eigenstates and energies. The lowest energy spin 3/2 state is compared to the lowest energy spin 1/2 state to determine whether the ground state is ferromagnetic. Additionally, for comparison, we calculate the spin gap Δ, defined to be the energy difference between the two lowest energy spin 3/2 states.

3.2.1.3 Spin 1/2 States

For the spin 1/2 state, we consider the case where two electrons are spin up and one is spin down. For configurations with at most one electron per site, this gives three states, one of which is part of the spin 3/2 quartet, and the other two of which have spin 1/2, as follows:

$$|\psi_{3/2}\rangle = \frac{1}{\sqrt{3}}\big(\,|\uparrow\uparrow\downarrow\rangle + |\uparrow\downarrow\uparrow\rangle + |\downarrow\uparrow\uparrow\rangle\,\big)$$
$$|\psi^{+}_{1/2}\rangle = \frac{1}{\sqrt{3}}\big(e^{\frac{2\pi i}{3}}\,|\uparrow\uparrow\downarrow\rangle + |\uparrow\downarrow\uparrow\rangle + e^{\frac{-2\pi i}{3}}\,|\downarrow\uparrow\uparrow\rangle\,\big)$$

$$|\psi^-_{1/2}\rangle = \frac{1}{\sqrt{3}}\left(e^{\frac{-2\pi i}{3}}\,|\uparrow\uparrow\downarrow\rangle + |\uparrow\downarrow\uparrow\rangle + e^{\frac{2\pi i}{3}}\,|\downarrow\uparrow\uparrow\rangle\right) \tag{3.3}$$

Define a matrix M such that

$$\begin{pmatrix} |\psi^+_{1/2}\rangle \\ \\ |\psi^-_{1/2}\rangle \end{pmatrix} = M \begin{pmatrix} |\uparrow\uparrow\downarrow\rangle \\ \\ |\uparrow\downarrow\uparrow\rangle \\ \\ |\downarrow\uparrow\uparrow\rangle \end{pmatrix} \tag{3.4}$$

which can be obtained simply by reading off the coefficients of eq. (3.3). Then we have a total of 8 low-energy spin 1/2 states with $S_z = 1/2$:

$$\begin{gathered} |\psi^+_1\psi^+_2\psi^+_3 0\rangle\,, \quad |\psi^+_1\psi^+_2 0\psi^+_3\rangle\,, \quad |\psi^+_1 0\psi^+_2\psi^+_3\rangle\,, \quad |0\psi^+_1\psi^+_2\psi^+_3\rangle\,, \\ \\ |\psi^-_1\psi^-_2\psi^-_3 0\rangle\,, \quad |\psi^-_1\psi^-_2 0\psi^-_3\rangle\,, \quad |\psi^-_1 0\psi^-_2\psi^-_3\rangle\,, \quad |0\psi^-_1\psi^-_2\psi^-_3\rangle \end{gathered} \tag{3.5}$$

Here ψ^i_j refers to the state of the jth spin of $|\psi^i_{1/2}\rangle$ defined as in eq. (3.3). For example, the state $|\psi^+_1 0\psi^+_2\psi^+_3\rangle = \frac{1}{\sqrt{3}}(e^{\frac{2\pi i}{3}} c^\dagger_{1\uparrow}c^\dagger_{3\uparrow}c^\dagger_{4\downarrow} + c^\dagger_{1\uparrow}c^\dagger_{3\downarrow}c^\dagger_{4\uparrow} + e^{\frac{-2\pi i}{3}} c^\dagger_{1\downarrow}c^\dagger_{3\uparrow}c^\dagger_{4\uparrow})\,|0\rangle$. There are also 12 high energy states, corresponding to all permutations of $|\uparrow\downarrow\uparrow\,0\,0\rangle$. These states only affect the energies to order t^2/U. Since Nagaoka's theorem applies only in the infinite U limit, we will initially consider only the low energy states, and afterward calculate corrections to order t^2/U.

Nagaoka ferromagnetism occurs because as a hole tunnels around a loop, it causes the other electron spins in the loop to be cyclically shifted one position. In the ferromagnetic state, all spins point in the same direction, and thus cycling them does not change the spin configuration. At a lower total spin, however, there is a mixture of up and down spins, and thus cycling them will

have some effect such as rotating one spin configuration into another or adding a phase, which can potentially increase the energy of the state with lower total spin. In our calculation, we see this effect when calculating the matrix elements of H between states where one electron has tunneled. If the two dots where the tunneling occurred are in consecutive order, then the spins remain in the same order, and the matrix element is given by the corresponding term in the Hamiltonian, as in the following example:

$$\langle s_1 s_2 s_3 0| \, H \, |s_1' s_2' 0 s_3' \rangle = -t \delta_{s_1 s_1'} \delta_{s_2 s_2'} \delta_{s_3 s_3'} \tag{3.6}$$

and thus matrix elements between ψ^i can be found via:

$$\langle \psi_1^i \psi_2^i \psi_3^i 0| \, H \, |\psi_1^j \psi_2^j 0 \psi_3^j \rangle = \left(M^* (-t) M^T \right)_{ij} = -t \delta_{ij} \tag{3.7}$$

and similarly for all other states of this form. However, if the dots are not in consecutive order, such as for example hopping between dots 1 and 4, then the spins can potentially be rearranged:

$$\langle s_1 s_2 s_3 0| \, H \, |0 s_1' s_2' s_3' \rangle = -t \delta_{s_2 s_1'} \delta_{s_3 s_2'} \delta_{s_1 s_3'} \tag{3.8}$$

and therefore:

$$\langle \psi_1^i \psi_2^i \psi_3^i 0| \, H \, |0 \psi_1^j \psi_2^j \psi_3^j \rangle = -t \left[M^* \begin{pmatrix} 0 & 1 & 0 \\ 0 & 0 & 1 \\ 1 & 0 & 0 \end{pmatrix} M^T \right]_{ij}$$

$$= \begin{pmatrix} -te^{\frac{-2\pi i}{3}} & 0 \\ 0 & -te^{\frac{2\pi i}{3}} \end{pmatrix}_{ij} \tag{3.9}$$

3.2.1.4 Finite U Corrections

For several of the geometries, we also determine the leading order corrections to $E_{1/2}$ for $U \gg t$ but not infinite. This is done using perturbation theory, but is complicated by the fact that the spin 1/2 states are often degenerate. We determine the matrix elements of H between the lowest energy spin 1/2 states, which we denote $|\Psi^i_{1/2}\rangle$ and the high energy $(2,1,0,0)$ states, which we denote $|\Phi^i\rangle$ and order as follows:

$$\begin{gathered} |\uparrow\downarrow 0 \uparrow 0\rangle, \quad |0 \uparrow\downarrow 0 \uparrow\rangle, \quad |\uparrow 0 \uparrow\downarrow 0\rangle, \quad |0 \uparrow 0 \uparrow\downarrow\rangle, \\ |\uparrow\downarrow\uparrow 0\, 0\rangle, \quad |\uparrow\downarrow 0\, 0 \uparrow\rangle, \quad |0 \uparrow\downarrow\uparrow 0\rangle, \quad |\uparrow\uparrow\downarrow 0\, 0\rangle, \\ |0\, 0 \uparrow\downarrow\uparrow\rangle, \quad |0 \uparrow\uparrow\downarrow 0\rangle, \quad |\uparrow 0\, 0 \uparrow\downarrow\rangle, \quad |0\, 0 \uparrow\uparrow\downarrow\rangle, \end{gathered} \tag{3.10}$$

We define the matrices T and Λ as follows:

$$T_{ij} = \langle\Phi^i| H |\Psi^j_{1/2}\rangle \tag{3.11}$$

$$\Lambda_{ij} = \langle\Phi^i| H |\Phi^j\rangle \tag{3.12}$$

Note that Λ is diagonal to leading order in t/U, and is given simply by the energies of $|\Phi^i\rangle$. Then the corrections to the singlet state energies to order t^2/U are given by the eigenvalues of the matrix $-T^\dagger \Lambda^{-1} T$.

3.2.2 Ground State Calculations

3.2.2.1 Square with no Diagonal Hopping

We initially consider a system of four dots in a square, where t_{ij} and V_{ij} are given as follows:

$$t_{ij} = \begin{cases} -t_a & \text{if } i-j = \pm 1 \mod 4 \\ 0 & \text{otherwise} \end{cases} \tag{3.13}$$

$$V_{ij} = \begin{cases} V_a & \text{if } i-j = \pm 1 \mod 4 \\ V_d & \text{if } i-j = 2 \mod 4 \end{cases} \tag{3.14}$$

Up to symmetry, three different electron configurations are possible:

$$\begin{aligned} (1,1,1,0) &\text{ with energy: } 2V_a + V_d \\ (2,0,1,0) &\text{ with energy: } U_0 + 2V_d \\ (2,1,0,0) &\text{ with energy: } U_0 + 2V_a \end{aligned} \tag{3.15}$$

We shift the total energy of the Hamiltonian by a constant amount $2V_a + V_d$, and define U and V as:

$$\begin{aligned} U &\equiv U_0 - 2V_a + V_d \\ V &\equiv V_a - V_d \end{aligned} \tag{3.16}$$

so that the energies of the three electron configurations in eq. (3.15) become 0, U, and

$U + 2V$ respectively. Then the spin 3/2 Hamiltonian in the basis given by eq. (3.2) is:

$$H_{3/2} = -t_a \begin{pmatrix} 0 & 1 & 0 & 1 \\ 1 & 0 & 1 & 0 \\ 0 & 1 & 0 & 1 \\ 1 & 0 & 1 & 0 \end{pmatrix} \tag{3.17}$$

which has ground state $\Psi_{3/2} = \frac{1}{2}(1\,1\,1\,1)^T$ and energy $E_{3/2} = -2t_a$. The first excited spin 3/2 state has energy 0, so the spin gap is $\Delta = 2t_a$.

We now find the spin 1/2 Hamiltonian. From eq. (3.9), a phase is introduced when tunneling the hole around the loop. Thus the spin 1/2 Hamiltonian is given by a block diagonal matrix consisting of two blocks, corresponding to $\psi^{\pm}_{1/2}$ as defined in eq. (3.3):

$$H^{\pm}_{1/2} = -t_a \begin{pmatrix} 0 & 1 & 0 & e^{\mp\frac{2\pi i}{3}} \\ 1 & 0 & 1 & 0 \\ 0 & 1 & 0 & 1 \\ e^{\pm\frac{2\pi i}{3}} & 0 & 1 & 0 \end{pmatrix} \tag{3.18}$$

which has ground states given by:

$$\begin{aligned} \Psi^{\pm}_{1/2} = \frac{1}{2}\Big[& |\psi^{\pm}_1\psi^{\pm}_2\psi^{\pm}_3 0\rangle + e^{\pm\frac{\pi i}{6}} |\psi^{\pm}_1\psi^{\pm}_2 0\psi^{\pm}_3\rangle \\ & + e^{\pm\frac{\pi i}{3}} |\psi^{\pm}_1 0\psi^{\pm}_2\psi^{\pm}_3\rangle \pm i\, |0\psi^{\pm}_1\psi^{\pm}_2\psi^{\pm}_3\rangle \Big] \end{aligned} \tag{3.19}$$

with energy $E^{\pm}_{1/2} = -\sqrt{3}t_a$. Thus in the infinite U limit, the system exhibits ferromag-

netism, since the spin 3/2 state has lower energy.

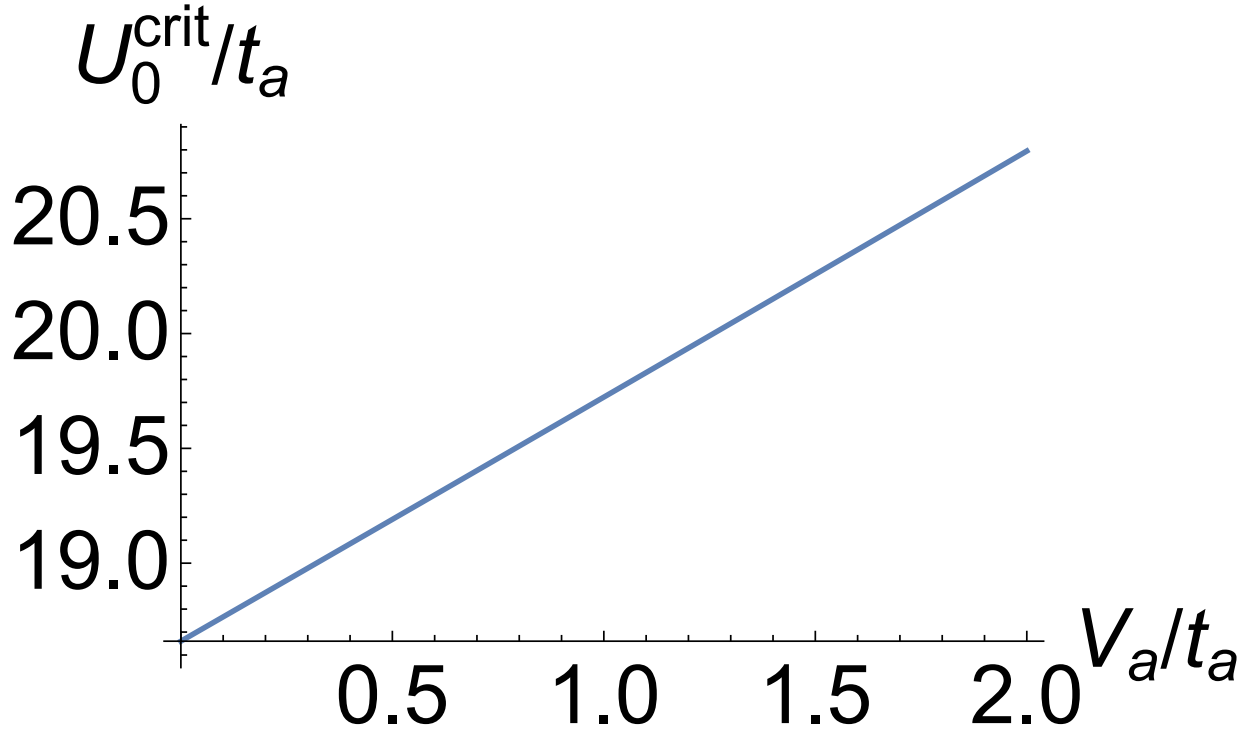

Figure 3.2: U_0^{crit} versus V_a for three electrons in a four-dot square configuration. Here $V_d = V_a/\sqrt{2}$.

We also determine the finite U corrections to $E_{1/2}$. Since there are two degenerate spin 1/2 states, $-T^\dagger \Lambda^{-1} T$ is a 2×2 matrix, given by:

$$-T^\dagger \Lambda^{-1} T = \Big[-3\frac{t_a^2}{U} - 2\frac{t_a^2}{U+2V} \Big] \begin{pmatrix} 1 & 0 \\ 0 & 1 \end{pmatrix} \tag{3.20}$$

Hence we find that the $\Psi_{1/2}^{\pm}$ degeneracy remains unbroken, and the spin 1/2 ground state energy is given by:

$$E_{1/2} = -\sqrt{3}t_a - 3\frac{t_a^2}{U} - 2\frac{t_a^2}{U+2V} + O\Big(\frac{t_a^3}{U^2}\Big) \tag{3.21}$$

Then for $V \to 0$, we recover a correction of $-5t_a^2/U$, agreeing with the result given in

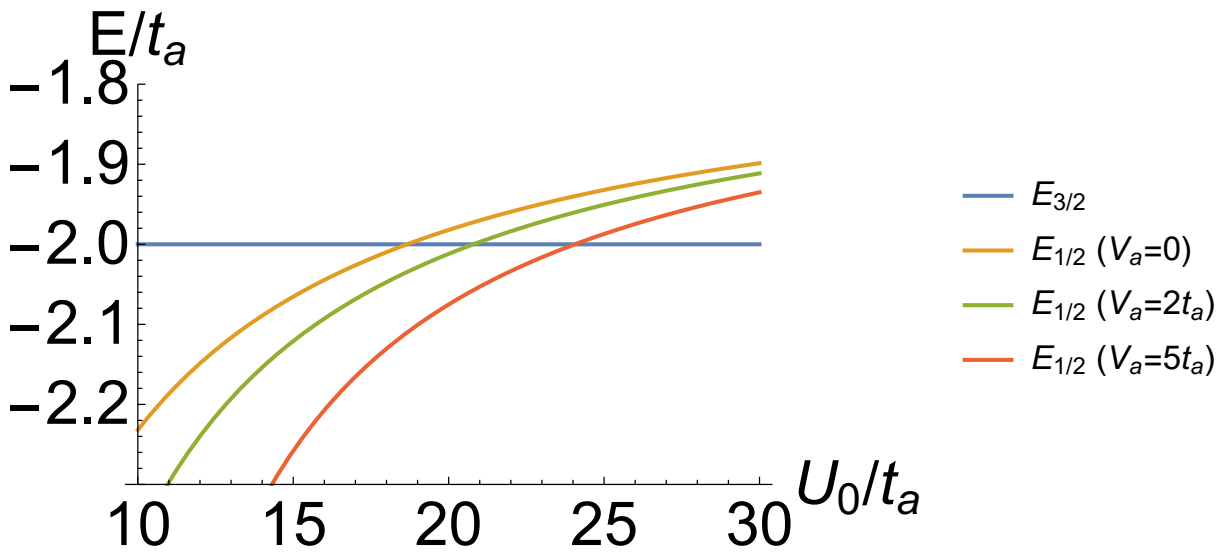

Figure 3.3: $E_{3/2}$ and $E_{1/2}$ versus U_0 for different values of V_a for three electrons in a four-dot square configuration. The point where $E_{3/2}$ and $E_{1/2}$ cross is U_0^{crit}. Here $V_d = V_a/\sqrt{2}$.

Ref. [9]. Using this result, we can derive the value U_{crit} (to first order in t_a/U) which marks the transition between the ferromagnetic and antiferromagnetic phases:

$$U_{\text{crit}} = \frac{1}{2(2-\sqrt{3})}\Big[-2(2-\sqrt{3})V + 5t_a + \sqrt{(2(2-\sqrt{3})V - 5t_a)^2 + 24(2-\sqrt{3})Vt_a}\Big] \tag{3.22}$$

For $V \to 0$, this gives $U_{\text{crit}} = 5t_a/(2-\sqrt{3}) \approx 18.7t_a$. From this point we use eq. (3.16) to find the raw parameter value U_0^{crit} as a function of V_a and V_d, plotting the result in fig. 3.2, with $V_d = V_a/\sqrt{2}$. In fig. 3.3 we also plot the energies $E_{3/2}$ and $E_{1/2}$ at different values of V_a as a function of U_0. These figures demonstrate that the value of U_0 which marks the transition between ferromagnetism and antiferromagnetism increases as the strength of the long-range Coulomb interaction V_a increases. This is because increasing V_a decreases the effective value of U defined

by eq. (3.16), which in tun increases the magnitude of the second order corrections in eq. (3.21). This means that the transition to an antiferromagnetic ground state will occur at a higher value of U_0.

3.2.2.2 Square with Diagonal Hopping

We now investigate how diagonal hopping terms effect the system. We use the same square configuration of four dots, but now add extra hopping terms $t_{13} = t_{31} = t_{42} = t_{24} = -t_d$. We again define U and V as in equation (3.16). The analysis for the spin 3/2 states is similar to above, except there are now extra matrix elements corresponding to t_d. These will be positive rather than negative as an extra minus sign is introduced due to Fermi statistics, since diagonal tunneling essentially exchanges two electrons. We emphasize that this sign difference originates from multi-electron effects. The single-particle hopping matrix elements have the same sign: $\langle 0|\, c_2|H|c_1^\dagger\,|0\rangle = -t_a$ and $\langle 0|\, c_3|H|c_1^\dagger\,|0\rangle = -t_d$. Thus there is no physical difference between nearest neighbor and next-nearest neighbor hopping. The sign difference arises as a result of the anticommutativity of the creation and annihilation operators when considering the multi-electron wavefunctions: $\langle 0|\, c_4c_3c_2|H|c_1^\dagger c_3^\dagger c_4^\dagger\,|0\rangle = -t_a$ but $\langle 0|\, c_4c_3c_2|H|c_1^\dagger c_2^\dagger c_4^\dagger\,|0\rangle = +t_d$. Then the spin 3/2 Hamiltonian is given as follows:

$$H_{3/2} = \begin{pmatrix} 0 & -t_a & t_d & -t_a \\ -t_a & 0 & -t_a & t_d \\ t_d & -t_a & 0 & -t_a \\ -t_a & t_d & -t_a & 0 \end{pmatrix} \tag{3.23}$$

which has ground state $\Psi_{3/2} = \frac{1}{2}(1\,1\,1\,1)^T$ and energy $E_{3/2} = -2t_a + t_d$. The first excited state has energy $-t_d$, so the spin gap is $\Delta = 2t_a - 2t_d$.

The analysis for the spin 1/2 states is also similar to the square model, with again the only difference in the infinite U limit being the diagonal hopping terms t_d. Then a calculation similar to eq. (3.9) yields:

$$\begin{aligned}\langle\psi_1^i\psi_2^i\psi_3^i 0|\, H\, |\psi_1^j 0\psi_2^j\psi_3^j\rangle &= \begin{pmatrix} 0 & t_d e^{\frac{-2\pi i}{3}} \\ t_d e^{\frac{2\pi i}{3}} & 0 \end{pmatrix}_{ij} \\ \langle\psi_1^i\psi_2^i 0\psi_3^i|\, H\, |0\psi_1^j\psi_2^j\psi_3^j\rangle &= \begin{pmatrix} 0 & t_d e^{\frac{2\pi i}{3}} \\ t_d e^{\frac{-2\pi i}{3}} & 0 \end{pmatrix}_{ij}\end{aligned} \tag{3.24}$$

Thus diagonal hopping rotates $|\psi_{1/2}^+\rangle$ into $|\psi_{1/2}^-\rangle$ and vice versa. Then $H_{1/2}$ is no longer block-diagonal, and is given by:

$$H_{1/2} = \begin{pmatrix} 0 & -t_a & 0 & -t_a e^{\frac{-2\pi i}{3}} & 0 & 0 & t_d e^{\frac{-2\pi i}{3}} & 0 \\ -t_a & 0 & -t_a & 0 & 0 & 0 & 0 & t_d e^{\frac{2\pi i}{3}} \\ 0 & -t_a & 0 & -t_a & t_d e^{\frac{-2\pi i}{3}} & 0 & 0 & 0 \\ -t_a e^{\frac{2\pi i}{3}} & 0 & -t_a & 0 & 0 & t_d e^{\frac{2\pi i}{3}} & 0 & 0 \\ 0 & 0 & t_d e^{\frac{2\pi i}{3}} & 0 & 0 & -t_a & 0 & -t_a e^{\frac{2\pi i}{3}} \\ 0 & 0 & 0 & t_d e^{\frac{-2\pi i}{3}} & -t_a & 0 & -t_a & 0 \\ t_d e^{\frac{2\pi i}{3}} & 0 & 0 & 0 & 0 & -t_a & 0 & -t_a \\ 0 & t_d e^{\frac{-2\pi i}{3}} & 0 & 0 & -t_a e^{\frac{-2\pi i}{3}} & 0 & -t_a & 0 \end{pmatrix} \tag{3.25}$$

which has two degenerate ground states with energy $E_{1/2} = -\sqrt{3t_a^2 + t_d^2}$. Thus, in the

infinite U limit, $E_{3/2} < E_{1/2}$ as long as $t_d < t_a/4$, and thus ferromagnetism only exists for $t_d < t_a/4$, as demonstrated in fig. 3.4. This crossover point must exist somewhere, as the limiting cases are a square with no diagonal hopping which exhibits ferromagnetism under Nagaoka's theroem, and a complete graph, which exhibits antiferromagnetism.

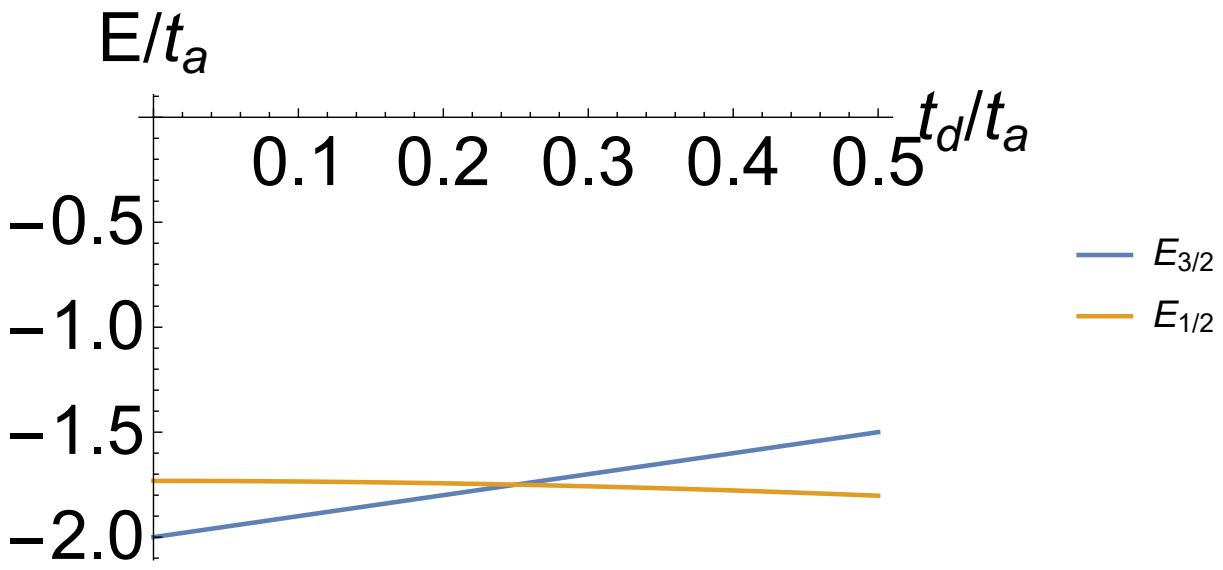

Figure 3.4: Plot of $E_{3/2}$ and $E_{1/2}$ versus t_d/t_a for three electrons in a four-dot square configuration with diagonal hopping in the infinite U limit. We see that ground state ferromagnetism is only possible for $t_d < t_a/4$.

3.2.2.3 Rectangle with no Diagonal Hopping

We now model a rectangular configuration of four dots. This will be similar to the square model, except t_{ij} and V_{ij} are given by:

$$t_{ij} = \begin{cases} -t_a & \text{if } \{i,j\} = \{1,2\} \text{ or } \{3,4\} \\ -t_b & \text{if } \{i,j\} = \{2,3\} \text{ or } \{1,4\} \\ 0 & \text{otherwise} \end{cases} \tag{3.26}$$

$$V_{ij} = \begin{cases} V_a & \text{if } \{i,j\} = \{1,2\} \text{ or } \{3,4\} \\ V_b & \text{if } \{i,j\} = \{2,3\} \text{ or } \{1,4\} \\ V_d & \text{if } i - j = \pm 2 \end{cases} \tag{3.27}$$

Without loss of generality, we will assume $b > a$, and thus $t_a > t_b$ and $V_a > V_b$. We note that up to symmetry the following four electron configurations are possible:

$$\begin{aligned} &(1,1,1,0) \text{ with energy: } V_a + V_b + V_d \\ &(2,0,1,0) \text{ with energy: } U_0 + 2V_d \\ &(2,0,0,1) \text{ with energy: } U_0 + 2V_b \\ &(2,1,0,0) \text{ with energy: } U_0 + 2V_a \end{aligned} \tag{3.28}$$

We shift the total energy by $V_a + V_b + V_d$, and define U, V, and W as:

$$\begin{aligned} U &\equiv U_0 - V_a - V_b + V_d \\ V &\equiv V_a - V_d \\ W &\equiv V_b - V_d \end{aligned} \tag{3.29}$$

so that the energies of the electron configurations in eq. (3.28) become 0, U, $U + 2W$, $U + 2V$ respectively. The analysis for the spin 3/2 states is identical to the square model, except that care must be taken to distinguish between t_a and t_b. Thus we construct the Hamiltonian:

$$H_{3/2} = \begin{pmatrix} 0 & -t_a & 0 & -t_b \\ -t_a & 0 & -t_b & 0 \\ 0 & -t_b & 0 & -t_a \\ -t_b & 0 & -t_a & 0 \end{pmatrix} \tag{3.30}$$

which has ground state $\Psi_{3/2} = \frac{1}{2}(1\,1\,1\,1)^T$ and energy $E_{3/2} = -t_a - t_b$. The first excited state has energy $-t_a + t_b$, so the spin gap is $\Delta = 2t_b$.

The analysis for the spin 1/2 states is also similar to the square model, with again the only difference in the infinite U limit being the the second hopping strength t_b. Then the spin 1/2

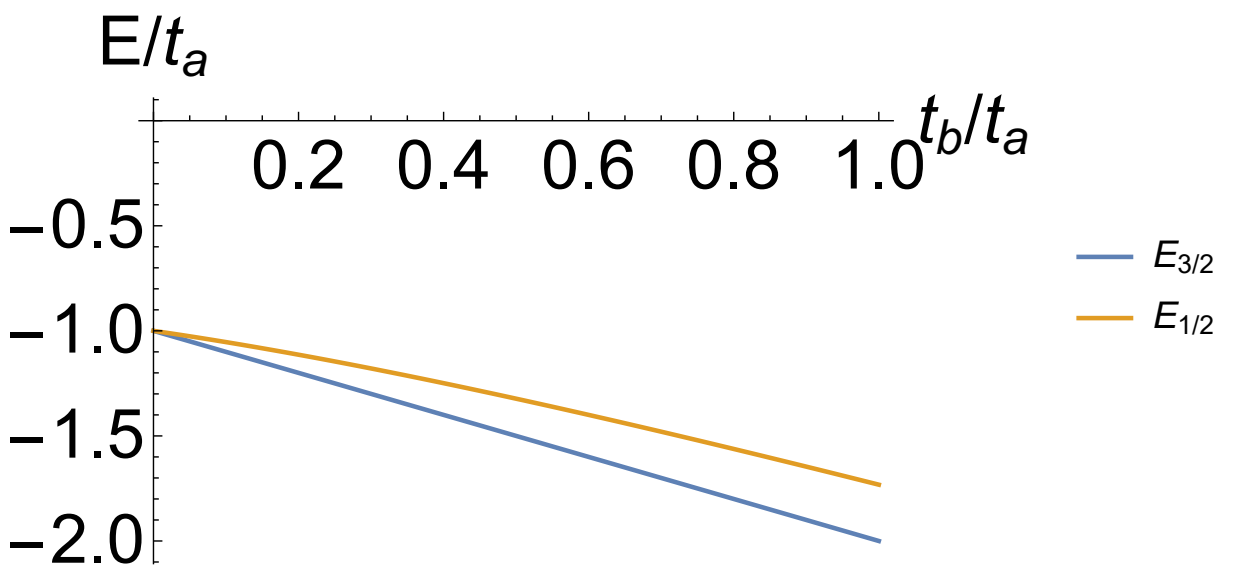

Figure 3.5: Plot of $E_{3/2}$ and $E_{1/2}$ versus t_b/t_a for three electrons in a four-dot rectangular configuration with no diagonal hopping in the infinite U limit.

Hamiltonian is given by:

$$H^{\pm}_{1/2} = \begin{pmatrix} 0 & -t_a & 0 & -t_b e^{\mp \frac{2\pi i}{3}} \\ -t_a & 0 & -t_b & 0 \\ 0 & -t_b & 0 & -t_a \\ -t_b e^{\pm \frac{2\pi i}{3}} & 0 & -t_a & 0 \end{pmatrix} \tag{3.31}$$

which has energy $E^{\pm}_{1/2} = -\sqrt{t_a^2 + t_a t_b + t_b^2}$, and ground state given by:

$$\Psi^{\pm}_{1/2} = \frac{1}{2}\Big[|\psi_1^{\pm}\psi_2^{\pm}\psi_3^{\pm}0\rangle + e^{\pm i\varphi} |\psi_1^{\pm}\psi_2^{\pm}0\psi_3^{\pm}\rangle + e^{\pm i\frac{\pi}{3}} |\psi_1^{\pm}0\psi_2^{\pm}\psi_3^{\pm}\rangle + e^{\pm i(\varphi+\frac{\pi}{3})} |0\psi_1^{\pm}\psi_2^{\pm}\psi_3^{\pm}\rangle \Big] \tag{3.32}$$

where $\varphi \equiv \arctan \frac{\sqrt{3}t_b}{2t_a+t_b}$. Thus, three electrons in four dots arranged in a rectangular

configuration will exhibit ferromagnetism for large U, regardless of the ratio of t_a and t_b, as shown in fig. 3.5. This is assuming that there is no diagonal hopping, an assumption that may break down for extreme ratios of t_a to t_b.

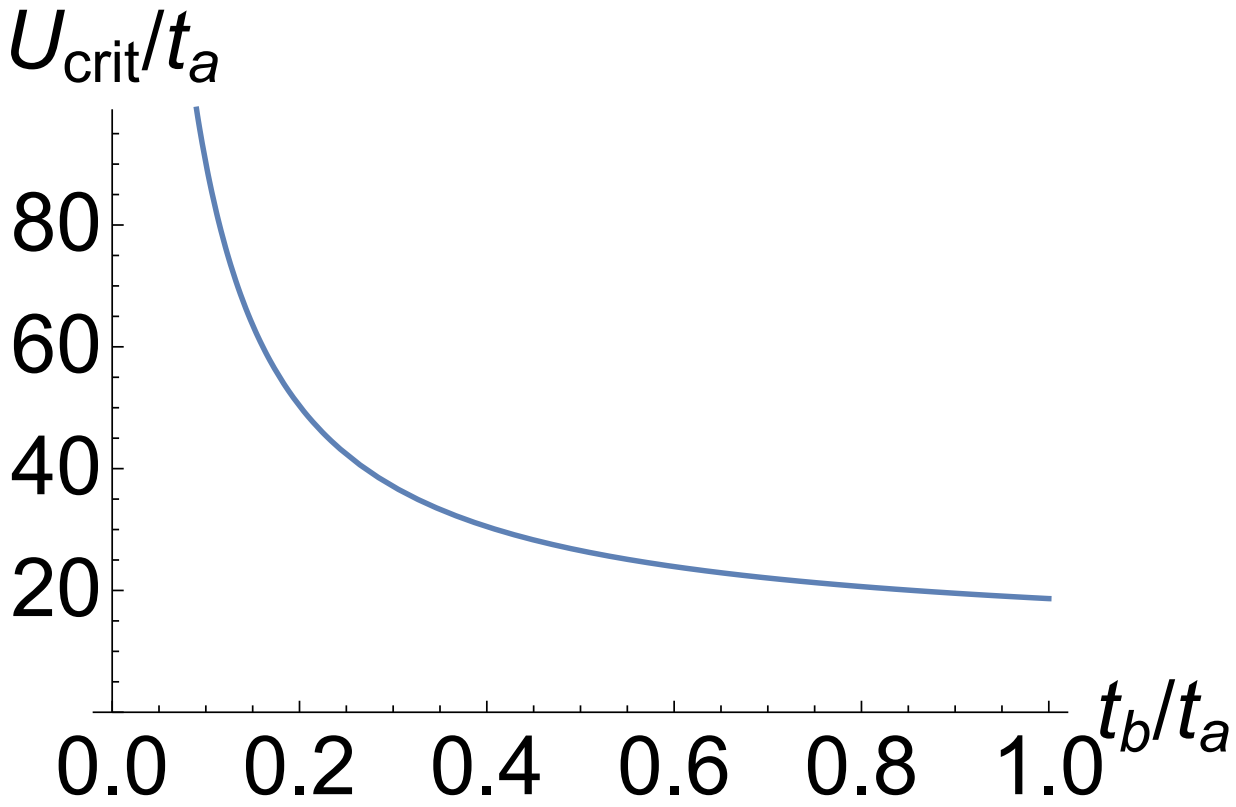

Figure 3.6: Plot of U_{crit} versus t_b/t_a for three electrons in a four-dot rectangular configuration with $V = W = 0$.

The procedure for calculating the finite U corrections to $E^{\pm}_{1/2}$ is also similar to the square model. We calculate $-T^{\dagger}\Lambda^{-1}T$ like before, obtaining:

$$
\begin{aligned}
&-T^{\dagger}\Lambda^{-1}T \\
&= \frac{-t_a^2 - t_a t_b - t_b^2}{U}
\begin{pmatrix}
1 & e^{\frac{-i\pi}{3} - i\varphi}\cos 3\varphi \\
e^{\frac{i\pi}{3} + i\varphi}\cos 3\varphi & 1
\end{pmatrix}
\end{aligned}
$$

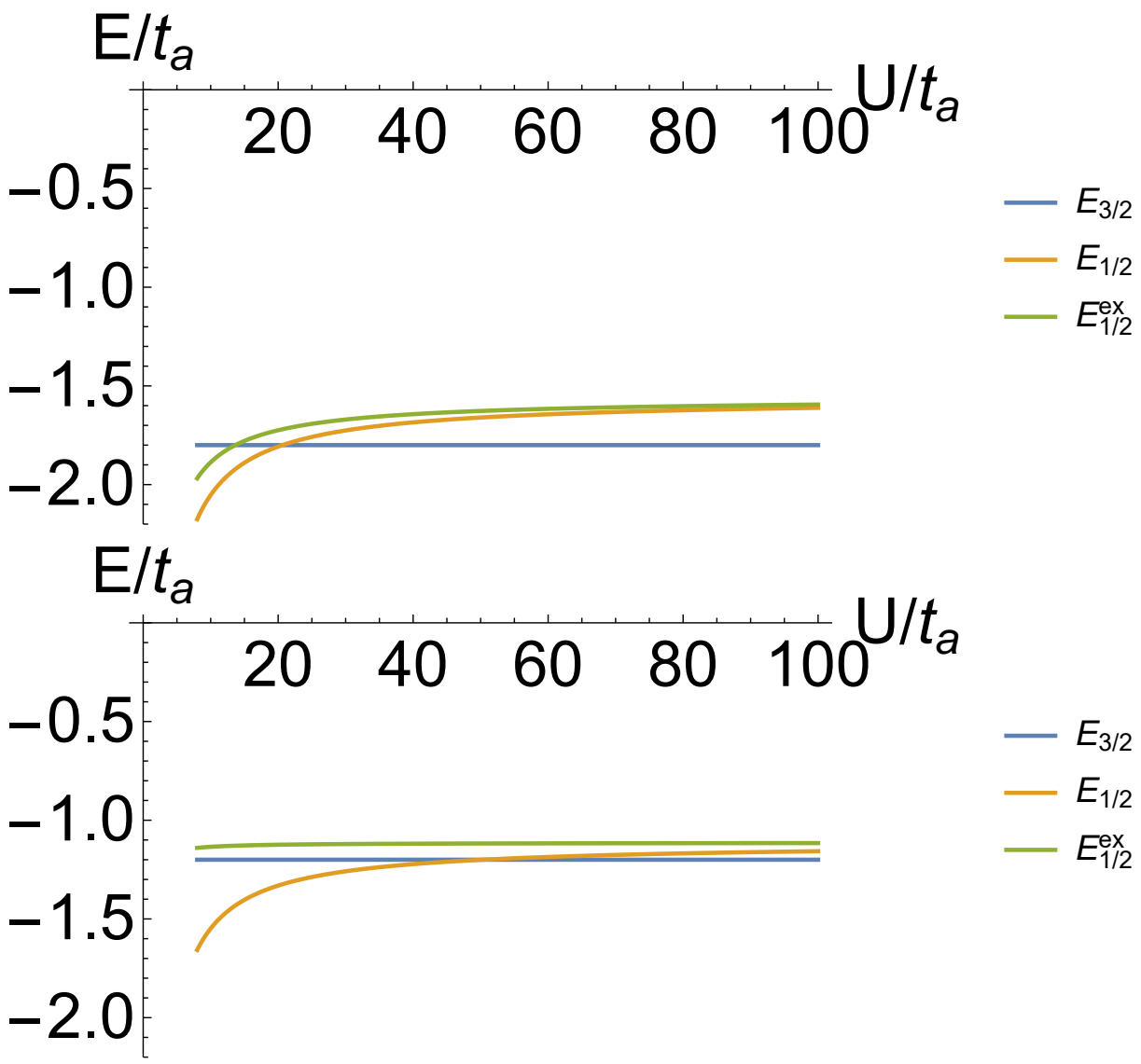

Figure 3.7: Plot of $E_{3/2}$, $E_{1/2}$, and the nearly-degenerate excited state energy $E^{\text{ex}}_{1/2}$ versus U for three electrons in a four-dot rectangular configuration with no diagonal hopping with $t_b/t_a = .8$ (Top) and $t_b/t_a = .2$ (Bottom). Here $V = W = 0$.

$$
-\frac{t_a^2}{U+2W}\begin{pmatrix} 1 & e^{\frac{-i\pi}{3}-i\varphi}\cos\varphi \\ e^{\frac{i\pi}{3}+i\varphi}\cos\varphi & 1 \end{pmatrix}
$$

$$
-\frac{t_b^2}{U+2V}\begin{pmatrix} 1 & -e^{\frac{-i\pi}{3}-i\varphi}\cos(\varphi-\frac{\pi}{3}) \\ -e^{\frac{i\pi}{3}+i\varphi}\cos(\varphi-\frac{\pi}{3}) & 1 \end{pmatrix}
$$

(3.33)

The off-diagonal terms break the $|\Psi^+_{1/2}\rangle, |\Psi^-_{1/2}\rangle$ degeneracy, with the lower energy state given by:

$$|\Psi_{1/2}\rangle = \frac{1}{\sqrt{2}}\Big[\,|\Psi^+_{1/2}\rangle + e^{\frac{i\pi}{3}+i\varphi}\,|\Psi^-_{1/2}\rangle\,\Big] \tag{3.34}$$

and thus, the energy of the lowest energy state is:

$$\begin{aligned} E_{1/2} = &-\sqrt{t_a^2 + t_a t_b + t_b^2} - \frac{t_a^2 + t_a t_b + t_b^2}{U}(1+\cos 3\varphi) \\ &- \frac{t_a^2}{U+2W}(1+\cos\varphi) - \frac{t_b^2}{U+2V}(1-\cos(\varphi-\frac{\pi}{3})) \end{aligned} \tag{3.35}$$

In fig. 3.6, we plot the cutoff value of U such that ground state ferromagnetism is present U_{crit} against the ratio of t_b to t_a. For small t_b, we find that the required onsite interaction energy grows very large, and thus while ground state ferromagnetism is present for any size rectangle in the infinite U limit, there will be some practical limit to the size of the rectangle in experimental systems where U will be finite. This effect is demonstrated in fig. 3.7, where the crossover point between $E_{1/2}$ and $E_{3/2}$ moves far to the right for smaller t_b due to how close the energies become in the infinite U limit.

3.2.2.4 Rectangle with Diagonal Hopping

We now address the case of diagonal hopping in a rectangular system. We define t_a and t_b as in eq. (3.26), and let the diagonal hopping term be given by t_d. We assume $t_a > t_b > t_d$. We shift the total energy by $V_a + V_b + V_d$, as in the rectangular case, and define U, V, W as in

equation (3.29).

The analysis for the spin 3/2 states is similar to above. Thus we construct the Hamiltonian:

$$H_{3/2} = \begin{pmatrix} 0 & -t_a & t_d & -t_b \\ -t_a & 0 & -t_b & t_d \\ t_d & -t_b & 0 & -t_a \\ -t_b & t_d & -t_a & 0 \end{pmatrix} \tag{3.36}$$

which has ground state $\Psi_{3/2} = \frac{1}{2}(1\,1\,1\,1)^T$ and energy $E_{3/2} = -t_a - t_b + t_d$. The first excited state has energy $-t_a + t_b - t_d$, so the spin gap is $\Delta = 2t_b - 2t_d$.

The analysis for the spin 1/2 states is also similar to above. Then $H_{1/2}$ is given by:

$$H_{1/2} = \begin{pmatrix} 0 & -t_a & 0 & -t_b e^{\frac{-2\pi i}{3}} & 0 & 0 & t_d e^{\frac{-2\pi i}{3}} & 0 \\ -t_a & 0 & -t_b & 0 & 0 & 0 & 0 & t_d e^{\frac{2\pi i}{3}} \\ 0 & -t_b & 0 & -t_a & t_d e^{\frac{-2\pi i}{3}} & 0 & 0 & 0 \\ -t_b e^{\frac{2\pi i}{3}} & 0 & -t_a & 0 & 0 & t_d e^{\frac{2\pi i}{3}} & 0 & 0 \\ 0 & 0 & t_d e^{\frac{2\pi i}{3}} & 0 & 0 & -t_a & 0 & -t_b e^{\frac{2\pi i}{3}} \\ 0 & 0 & 0 & t_d e^{\frac{-2\pi i}{3}} & -t_a & 0 & -t_b & 0 \\ t_d e^{\frac{2\pi i}{3}} & 0 & 0 & 0 & 0 & -t_b & 0 & -t_a \\ 0 & t_d e^{\frac{-2\pi i}{3}} & 0 & 0 & -t_b e^{\frac{-2\pi i}{3}} & 0 & -t_a & 0 \end{pmatrix} \tag{3.37}$$

which has a nondegenerate ground state with energy $E_{1/2} = -\sqrt{t_a^2 + t_b^2 + t_d^2 + t_a t_b + t_a t_d - t_b t_d}$. From this, it is easy to show that in the infinite U limit, $E_{3/2} < E_{1/2}$ as long as $t_d < t_a t_b/(3t_a + t_b)$.

3.2.2.5 Linear Array of Four Dots

We also model a linear array of four dots. This will be similar to the square model, except $t_{14} = t_{41} = 0$, and V_{ij} is given by:

$$V_{ij} = \begin{cases} V_a & \text{if } i-j = \pm 1 \\ V_{2a} & \text{if } i-j = \pm 2 \\ V_{3a} & \text{if } i-j = \pm 3 \end{cases} \tag{3.38}$$

We note that up to symmetry, the following electron configurations are possible:

$$\begin{aligned} &(1,1,0,1) \text{ with energy: } V_a + V_{2a} + V_{3a} \\ &(1,1,1,0) \text{ with energy: } 2V_a + V_{2a} \\ &(2,0,0,1) \text{ with energy: } U_0 + 2V_{3a} \\ &(2,0,1,0) \text{ with energy: } U_0 + 2V_{2a} \\ &(2,1,0,0) \text{ with energy: } U_0 + 2V_a \end{aligned} \tag{3.39}$$

We shift the total energy by $V_a + V_{2a} + V_{3a}$, and define U, V, and W as:

$$\begin{aligned} U &\equiv U_0 - V_a - V_{2a} + V_{3a} \\ V &\equiv V_a - V_{3a} \\ W &\equiv V_{2a} - V_{3a} \end{aligned} \tag{3.40}$$

so that the energies of the electron configurations in eq. (3.39) become 0, V, U, $U+2W$, $U+2V$ respectively. The analysis for the spin 3/2 states is identical to the square model, except that some states have an extra energy V, and no hopping is permitted between dots 1 and 4. Thus we construct the Hamiltonian:

$$H_{3/2} = \begin{pmatrix} V & -t_a & 0 & 0 \\ -t_a & 0 & -t_a & 0 \\ 0 & -t_a & 0 & -t_a \\ 0 & 0 & -t_a & V \end{pmatrix} \tag{3.41}$$

which has a nondegenerate ground state with energy:

$$E_{3/2} = (V - t_a - \sqrt{(V+t_a)^2 + 4t_a^2})/2 \tag{3.42}$$

and ground state given by:

$$\Psi_{3/2} = \frac{1}{\sqrt{2}\sqrt{1 + \frac{(V-E_{3/2})^2}{t_a^2}}} \begin{pmatrix} 1 \\ (V-E_{3/2})/t_a \\ (V-E_{3/2})/t_a \\ 1 \end{pmatrix} \tag{3.43}$$

For convenience, we define $A(V,t)$ and $B(V,t)$ from eq. (3.43) above such that $\Psi_{3/2} = (A\ B\ B\ A)^T$. The first excited state has energy $(V + t_a - \sqrt{(V-t_a)^2 + 4t_a^2})/2$, and so the spin gap is given by the difference of this energy and $E_{3/2}$.

In the square model without diagonal hopping, the only difference between the spin 3/2

and spin 1/2 subspaces in the infinite U limit is in the hopping term between dots 1 and 4. Since this term no longer exists in the linear model, we find that the spin 1/2 Hamiltonian is simply two exact copies of the spin 3/2 Hamiltonian, $H^{\pm}_{1/2} = H_{3/2}$, and thus the ground state energy $E^{\pm}_{1/2} = E_{3/2}$, as well. Thus for finite U, the system cannot exhibit ferromagnetism, since the finite U corrections will lower the energy of the spin 1/2 states, as shown in fig. 3.8.

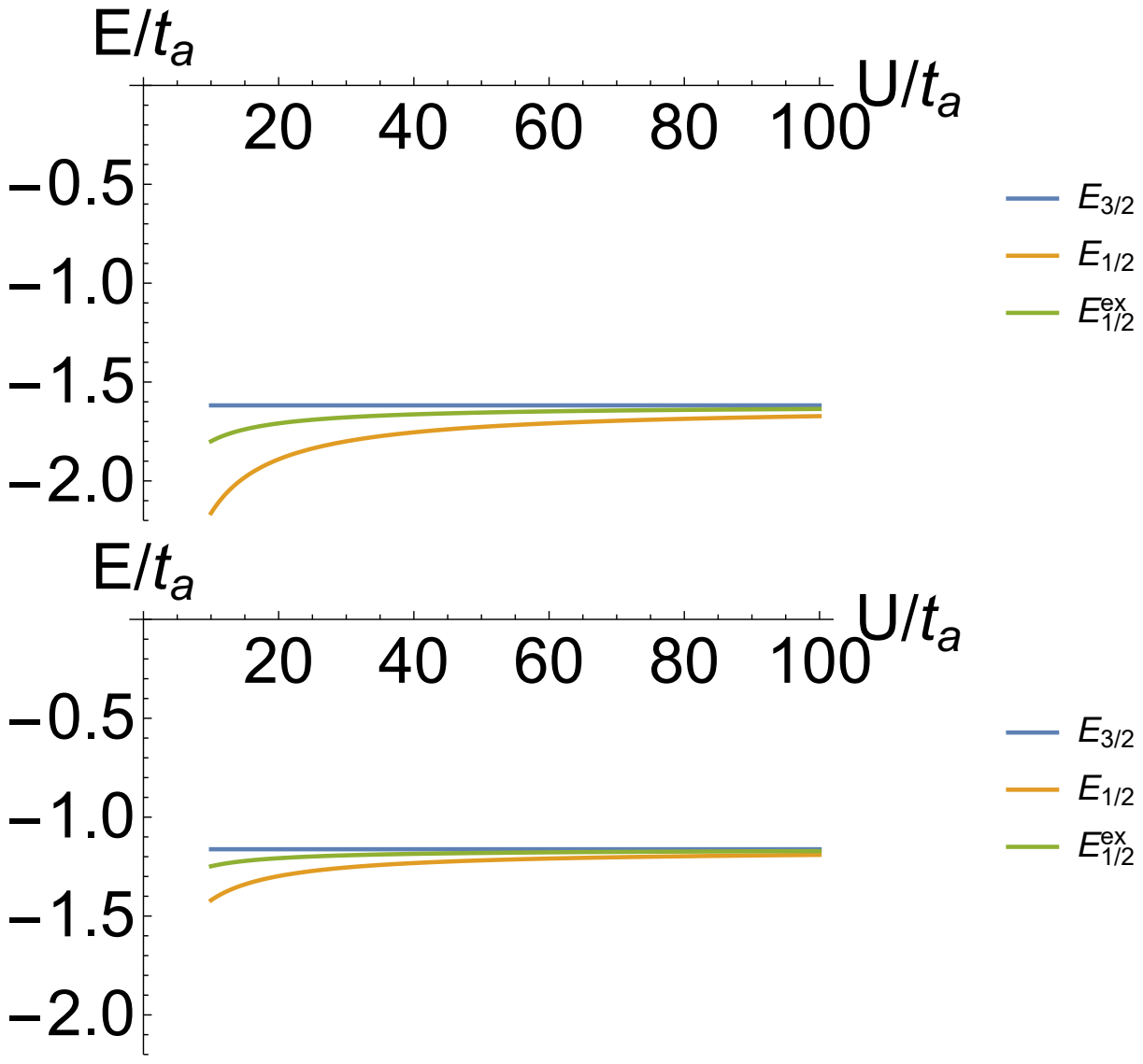

Figure 3.8: Plot of $E_{3/2}$, $E_{1/2}$ and $E^{\text{ex}}_{1/2}$ versus U for three electrons in a four-dot linear array for $V = 0$ (Top) and $V = 5t_a$ (Bottom). Here $W = V/4$.

We repeat the procedure discussed above to calculate the finite U corrections to $E^{\pm}_{1/2}$. Then $-T^{\dagger}\Lambda^{-1}T$ is given by:

$$
\begin{aligned}
&-T^{\dagger}\Lambda^{-1}T \\
&= \left[\frac{-B^2t_a^2}{U} - \frac{((A+B)^2+A^2)t_a^2}{U+2W} - \frac{2A^2t_a^2}{U+2V}\right]\begin{pmatrix} 2 & 1 \\ 1 & 2 \end{pmatrix}
\end{aligned}
\tag{3.44}
$$

The off-diagonal terms break the $|\Psi^{+}_{1/2}\rangle, |\Psi^{-}_{1/2}\rangle$ degeneracy, with the lower energy state given by:

$$
|\Psi_{1/2}\rangle = \frac{1}{\sqrt{2}}\Big[\,|\Psi^{+}_{1/2}\rangle + |\Psi^{-}_{1/2}\rangle\,\Big] \tag{3.45}
$$

which corresponds to the spin configuration:

$$
\frac{1}{\sqrt{6}}\big[\,-|\uparrow\uparrow\downarrow\rangle + 2\,|\uparrow\downarrow\uparrow\rangle - |\downarrow\uparrow\uparrow\rangle\,\big] \tag{3.46}
$$

This spin configuration is the spin 1/2 state which maximizes overlap with the alternating spin configuration $|\uparrow\downarrow\uparrow\rangle$, and so the ground state of 3 electrons in a linear array of 4 dots is an antiferromagnet. The ground state energy is given by:

$$
\begin{aligned}
E_{1/2} = &\frac{V - t_a - \sqrt{(V+t_a)^2 + 4t_a^2}}{2} \\
&- 3t_a^2\left[\frac{B^2}{U} + \frac{((A+B)^2+A^2)}{U+2W} + \frac{2A^2}{U+2V}\right]
\end{aligned}
\tag{3.47}
$$

3.2.2.6 Y-Shaped Configuration

We now model a Y-shaped configuration of four dots. We will let dots 2 through 4 be positioned at the corners of an equilateral triangle, and dot 1 be at the center, with hopping terms only between a corner dot and the center dot. Then t_{ij} and V_{ij} are given by:

$$t_{ij} = \begin{cases} -t_a & \text{if } i \text{ or } j = 1 \\ 0 & \text{otherwise} \end{cases} \tag{3.48}$$

$$V_{ij} = \begin{cases} V_a & \text{if } i \text{ or } j = 1 \\ V_d & \text{otherwise} \end{cases} \tag{3.49}$$

Then up to symmetry, the following electron configurations are possible:

$$\begin{aligned} &(0,1,1,1) \text{ with energy: } 3V_d \\ &(1,1,1,0) \text{ with energy: } 2V_a + V_d \\ &(0,2,1,0) \text{ with energy: } U_0 + 2V_d \\ &(2,1,0,0) \text{ with energy: } U_0 + 2V_a \\ &(1,2,0,0) \text{ with energy: } U_0 + 2V_a \end{aligned} \tag{3.50}$$

We shift the total energy by $3V_d$, and define U and V as:

$$U \equiv U_0 - V_d$$

$$V \equiv V_a - V_d \tag{3.51}$$

so that the energies of the electron configurations in eq. (3.50) become 0, $2V$, U, $U+2V$, $U+2V$ respectively. Using the same methods as above, we construct the spin 3/2 Hamiltonian:

$$H_{3/2} = \begin{pmatrix} 2V & 0 & 0 & -t_a \\ 0 & 2V & 0 & t_a \\ 0 & 0 & 2V & -t_a \\ -t_a & t_a & -t_a & 0 \end{pmatrix} \tag{3.52}$$

which has a nondegenerate ground state with energy:

$$E_{3/2} = V - \sqrt{V^2 + 3t_a^2} \tag{3.53}$$

given by:

$$\Psi_{3/2} = \frac{1}{\sqrt{3 + \frac{9t_a^2}{E_{3/2}^2}}} \begin{pmatrix} 1 \\ -1 \\ 1 \\ 3t_a/(-E_{3/2}) \end{pmatrix} \tag{3.54}$$

The first excited state has energy $2V$, and so the spin gap is given by the difference $2V - E_{3/2}$.

For the spin 1/2 case, in the infinite U limit, the Hamiltonian separates into a block-diagonal

matrix with two blocks, where the basis for each block is given by:

$$|\psi_1^{\pm}\psi_2^{\pm}\psi_3^{\pm}0\rangle\,,\quad |\psi_1^{\mp}\psi_2^{\mp}0\psi_3^{\mp}\rangle\,,\quad |\psi_1^{\pm}0\psi_2^{\pm}\psi_3^{\pm}\rangle\,,\quad |0\psi_1^{\pm}\psi_2^{\pm}\psi_3^{\pm}\rangle \tag{3.55}$$

In this basis, the two blocks of the spin 1/2 Hamiltonian $H_{1/2}^{\pm}$ are given by:

$$H_{1/2}^{\pm} = \begin{pmatrix} 2V & 0 & 0 & -t_a e^{\mp\frac{2\pi i}{3}} \\ 0 & 2V & 0 & t_a e^{\mp\frac{2\pi i}{3}} \\ 0 & 0 & 2V & -t_a \\ -t_a e^{\pm\frac{2\pi i}{3}} & t_a e^{\pm\frac{2\pi i}{3}} & -t_a & 0 \end{pmatrix} \tag{3.56}$$

which is identical to $H_{3/2}$ up to a phase redefinition of some of the states. Therefore in the infinite U limit, $E_{1/2}^{\pm} = E_{3/2}$, and thus for finite U, the system cannot exhibit ferromagnetism, since the finite U corrections will lower the energy of the spin 1/2 states.

3.2.2.7 Y-Shaped Configuration With N.N.N. Hopping

We now add a next nearest neighbor hopping term t_d between the outer corners of the Y-shaped configuration. Then t_{ij} is given by:

$$t_{ij} = \begin{cases} -t_a & \text{if } i \text{ or } j = 1 \\ -t_d & \text{otherwise} \end{cases} \tag{3.57}$$

The same electron configurations as in eq. (3.50) above are possible. We again shift the total energy by $3V_2$, and define U and V as in eq. (3.51). Using the same methods as above, we

construct the Hamiltonian:

$$H_{3/2} = \begin{pmatrix} 2V & -t_d & t_d & -t_a \\ -t_d & 2V & -t_d & t_a \\ t_d & -t_d & 2V & -t_a \\ -t_a & t_a & -t_a & 0 \end{pmatrix} \tag{3.58}$$

which has a nondegenerate ground state with energy:

$$E_{3/2} = V + t_d - \sqrt{(V + t_d)^2 + 3t_a^2} \tag{3.59}$$

The first excited state has energy $2V - t_d$.

We construct the spin 1/2 Hamiltonian in the basis given by eq. (3.5) as follows:

$$H_{1/2} = \begin{pmatrix} 2V & -t_d & 0 & -t_a e^{\frac{-2\pi i}{3}} & 0 & 0 & t_d e^{\frac{-2\pi i}{3}} & 0 \\ -t_d & 2V & -t_d & 0 & 0 & 0 & 0 & t_a e^{\frac{2\pi i}{3}} \\ 0 & -t_d & 2V & -t_a & t_d e^{\frac{-2\pi i}{3}} & 0 & 0 & 0 \\ -t_a e^{\frac{2\pi i}{3}} & 0 & -t_a & 0 & 0 & t_a e^{\frac{2\pi i}{3}} & 0 & 0 \\ 0 & 0 & t_d e^{\frac{2\pi i}{3}} & 0 & 2V & -t_d & 0 & -t_a e^{\frac{2\pi i}{3}} \\ 0 & 0 & 0 & t_a e^{\frac{-2\pi i}{3}} & -t_d & 2V & -t_d & 0 \\ t_d e^{\frac{2\pi i}{3}} & 0 & 0 & 0 & 0 & -t_d & 2V & -t_a \\ 0 & t_a e^{\frac{-2\pi i}{3}} & 0 & 0 & -t_a e^{\frac{-2\pi i}{3}} & 0 & -t_a & 0 \end{pmatrix} \tag{3.60}$$

This matrix has two degenerate ground states with energy given by the smallest root of a

cubic polynomial $P(E_{1/2}) = 0$, where $P(E)$ is given by:

$$P(E) = E^3 - 4VE^2 + (-3t_a^2 - t_d^2 + 4V^2)E + 6t_a^2 V \tag{3.61}$$

To compare $E_{1/2}$ with $E_{3/2}$, one can show that $P(E_{3/2}) > 0$ for $0 < t_d < t_a$. This implies that there must be a root of $P(E)$ which lies to the left of $E_{3/2}$, and thus $E_{1/2} < E_{3/2}$. Therefore the ground state is not ferromagnetic.

3.2.3 Summary

Sec. num.	dot config.	n.n.n. hopping	$E_{3/2}$	$E_{1/2}$ for $U \to \infty$	Spin gap	Ferro-magnetism?
1	square	no	$-2t_a$	$-\sqrt{3}t_a$	$2t_a$	yes
2	square	yes	$-2t_a + t_d$	$-\sqrt{3t_a^2 + t_d^2}$	$2t_a - 2t_d$	if $t_d < t_a/4$
3	rectangle	no	$-t_a - t_b$	$-\sqrt{t_a^2 + t_a t_b + t_b^2}$	$2t_b$	yes
4	rectangle	yes	$-t_a - t_b + t_d$	$-\sqrt{\begin{matrix} t_a^2 + t_b^2 + t_d^2 \\ +t_a t_b + t_a t_d - t_b t_d \end{matrix}}$	$2t_b - 2t_d$	if $t_d < \frac{t_a t_b}{3t_a + t_b}$
5	linear	no	$\frac{1}{2}\begin{pmatrix} V - t_a \\ -\sqrt{(V+t_a)^2 + 4t_a^2} \end{pmatrix}$	$\frac{1}{2}\begin{pmatrix} V - t_a \\ -\sqrt{(V+t_a)^2 + 4t_a^2} \end{pmatrix}$	Δ_{lin}	no
6	Y-shaped	no	$V - \sqrt{V^2 + 3t_a^2}$	$V - \sqrt{V^2 + 3t_a^2}$	$2V - E_{3/2}$	no
7	Y-shaped	yes	$\begin{matrix} V + t_d \\ -\sqrt{(V+t_d)^2 + 3t_a^2} \end{matrix}$	given by $P(E_{1/2}) = 0$	$\begin{matrix} 2V - t_d \\ -E_{3/2} \end{matrix}$	no

Table 3.1: A summary of the analytical results obtained for three electrons in four-dot plaquettes of various geometries. Here V is given by $V = V_a - V_{3a}$ in sec. 5, and $V = V_a - V_d$ for sec. 6 and 7. Δ_{lin} and $P(E_{1/2})$ are given by: $\Delta_{\text{lin}} = t_a + \frac{1}{2}\left(\sqrt{(V+t_a)^2 + 4t_a^2} - \sqrt{(V-t_a)^2 + 4t_a^2}\right)$, $P(E_{1/2}) = E_{1/2}^3 - 4VE_{1/2}^2 + (-3t_a^2 - t_d^2 + 4V^2)E_{1/2} + 6t_a^2 V$

We have explored many different plaquette geometries in the presence of long-range Coulomb interactions, with and without next nearest neighbor hopping. We have found that in these systems, Nagaoka ferromagnetism is robust to the presence of long-range Coulomb interactions,

and is present even if the plaquette is rectangular rather than square. We argued that next nearest neighbor hopping can destroy Nagaoka ferromagnetism, and derived conditions for the value of t_d where this transition occurs for both the square and rectangular geometries. for completeness, we showed that other geometries such as a linear array and Y-shaped configuration have an antiferrromagnetic ground state. We present these findings in table 3.1.

3.3 Four Electrons In Four Dots

3.3.1 General Method

We now consider a half-filled band consisting of four electrons and four dots in an arbitrary configuration, for large U_0. It is well-known that for large systems, the ground state of a half-filled band is antiferromagnetic; however, we show that a four dot plaquette can have a partially ferromagnetic spin-1 ground state for certain geometries.

The lowest energy states will be in the $(1, 1, 1, 1)$ configuration, and we will shift the energy of our Hamiltonian to account for the Coulomb interaction energy in this configuration. Thus, by definition, the spin 2 states, which are not affected by tunneling, have energy $E_2 = 0$, and in the infinite U limit, the spin 0 and 1 states have 0 energy as well. We will define $U_{i(j)}$ to be the Coulomb interaction energy of the $(2, 1, 1, 0)$ configuration states with two electrons in dot i and no electrons in dot j, again offset by the energy of the $(1, 1, 1, 1)$ state. We ignore the $(2, 2, 0, 0)$ states, as they are not connected to the $(1, 1, 1, 1)$ states by a single tunneling operation, and thus will have no effect on the ground state energies to order t^2/U.

Our strategy is the same as when finding the finite U corrections in the previous section. We list all low energy states with a given spin. Since these will all be in the $(1, 1, 1, 1)$ configuration,

they will be degenerate to leading order. We then list the relevant high energy states, and let Λ be the diagonal matrix with entries given by the energies of the high energy states, and let the entries of T be given by the matrix elements of H between a low and a high energy state. Then the first order corrections in t^2/U to the energies of the low energy states are given by diagonalizing the matrix $-T^\dagger \Lambda^{-1} T$. This will potentially also break the degeneracy, as long as $-T^\dagger \Lambda^{-1} T$ is not proportional to the identity matrix.

3.3.1.1 Spin 0 States

There are two states with total spin 0 for electrons in the $(1,1,1,1)$ configuration:

$$|\Psi_0^\pm\rangle = \frac{1}{\sqrt{6}}\Big[e^{\pm\frac{2\pi i}{3}} |\uparrow\uparrow\downarrow\downarrow\rangle + |\uparrow\downarrow\uparrow\downarrow\rangle + e^{\mp\frac{2\pi i}{3}} |\uparrow\downarrow\downarrow\uparrow\rangle + e^{\mp\frac{2\pi i}{3}} |\downarrow\uparrow\uparrow\downarrow\rangle + |\downarrow\uparrow\downarrow\uparrow\rangle + e^{\pm\frac{2\pi i}{3}} |\downarrow\downarrow\uparrow\uparrow\rangle \Big] \tag{3.62}$$

There are 24 high energy states connected to $|\Psi_0^\pm\rangle$ by a single tunneling operation, corresponding to all permutations of $|\,1|\uparrow\downarrow 0\rangle$. However, due to conservation of spin, only states where the two single electrons form a spin singlet will contribute, and thus we need only consider 12 states. We calculating matrix elements between these states and $|\Psi_0^\pm\rangle$, we obtain the matrix $-T^\dagger \Lambda^{-1} T$:

$$-T^\dagger \Lambda^{-1} T = -\sum_{i\neq j} \frac{t_{ij}^2}{U_{i(j)}} \begin{pmatrix} 1 & e^{-i\varphi_{ij}} \\ e^{i\varphi_{ij}} & 1 \end{pmatrix} \tag{3.63}$$

where φ_{ij} is given by:

$$\varphi_{ij} = \begin{cases} \frac{\pi}{3} & \text{if } \{i,j\} = \{1,2\} \text{ or } \{3,4\} \\ \pi & \text{if } \{i,j\} = \{1,3\} \text{ or } \{2,4\} \\ \frac{5\pi}{3} & \text{if } \{i,j\} = \{1,4\} \text{ or } \{2,3\} \end{cases} \tag{3.64}$$

Thus, to order t^2/U, the total energy of the spin 0 ground state is:

$$E_0 = -\sum_{i \neq j} \frac{t_{ij}^2}{U_{i(j)}} - \left| \sum_{i \neq j} \frac{t_{ij}^2}{U_{i(j)}} e^{i\varphi_{ij}} \right| \tag{3.65}$$

3.3.1.2 Spin 1 States

To investigate the spin 1 states, we consider the subspace where $S_z = 1$. There are three states with total spin 1 for electrons in the $(1,1,1,1)$ configuration:

$$\begin{aligned} |\Psi_1^1\rangle &= \frac{1}{2}\Big[\, |\uparrow\uparrow\uparrow\downarrow\rangle + |\uparrow\uparrow\downarrow\uparrow\rangle - |\uparrow\downarrow\uparrow\uparrow\rangle - |\downarrow\uparrow\uparrow\uparrow\rangle \,\Big] \\ |\Psi_1^2\rangle &= \frac{1}{2}\Big[\, |\uparrow\uparrow\uparrow\downarrow\rangle - |\uparrow\uparrow\downarrow\uparrow\rangle + |\uparrow\downarrow\uparrow\uparrow\rangle - |\downarrow\uparrow\uparrow\uparrow\rangle \,\Big] \\ |\Psi_1^3\rangle &= \frac{1}{2}\Big[\, |\uparrow\uparrow\uparrow\downarrow\rangle - |\uparrow\uparrow\downarrow\uparrow\rangle - |\uparrow\downarrow\uparrow\uparrow\rangle + |\downarrow\uparrow\uparrow\uparrow\rangle \,\Big] \end{aligned} \tag{3.66}$$

There are 12 high energy states connected to $|\Psi_1^i\rangle$, given by all permutations of $|\!\downarrow\uparrow\uparrow\, 0\rangle$. Calculating matrix elements between these states and $|\Psi_1^i\rangle$, we find that $-T^\dagger \Lambda^{-1} T$ is given by:

$$-T^\dagger \Lambda^{-1} T = -\sum_{i \neq j} \frac{t_{ij}^2}{U_{i(j)}} \nVdash +$$

$$\begin{pmatrix} A_{12}+A_{34} & A_{23}-A_{14} & A_{13}-A_{24} \\ A_{23}-A_{14} & A_{13}+A_{24} & A_{12}-A_{34} \\ A_{13}-A_{24} & A_{12}-A_{34} & A_{14}+A_{23} \end{pmatrix} \tag{3.67}$$

where A_{ij} is given by:

$$A_{ij} = t_{ij}^2 \left(\frac{1}{U_{i(j)}} + \frac{1}{U_{j(i)}} \right) \tag{3.68}$$

3.3.2 Ground State Calculations

3.3.2.1 Square with no Diagonal Hopping

For four dots in a square, with no diagonal hopping, we have for spin 0,

$$(-T^\dagger \Lambda^{-1} T)_0 = -\frac{t_a^2}{U} \begin{pmatrix} 8 & 4 \\ 4 & 8 \end{pmatrix} \tag{3.69}$$

where $U \equiv U_0 - V_a$. The off-diagonal terms break the degeneracy, and the ground state and energy is given by:

$$\begin{aligned} |\Psi_0\rangle = \frac{1}{2\sqrt{3}} \Big[&- |\uparrow\uparrow\downarrow\downarrow\rangle + 2\,|\uparrow\downarrow\uparrow\downarrow\rangle - |\uparrow\downarrow\downarrow\uparrow\rangle \\ &- |\downarrow\uparrow\uparrow\downarrow\rangle + 2\,|\downarrow\uparrow\downarrow\uparrow\rangle - |\downarrow\downarrow\uparrow\uparrow\rangle \Big] \end{aligned} \tag{3.70}$$

$$E_0 = -12\frac{t_a^2}{U} \tag{3.71}$$

We note that as expected, this is the spin 0 state which maximizes overlap with the antifer-

romagnetic configurations $|\uparrow\downarrow\uparrow\downarrow\rangle$ and $|\downarrow\uparrow\downarrow\uparrow\rangle$. For spin 1, we have

$$(-T^\dagger \Lambda^{-1} T)_1 = -\frac{t_a^2}{U}\begin{pmatrix} 4 & 0 & 0 \\ 0 & 8 & 0 \\ 0 & 0 & 4 \end{pmatrix} \tag{3.72}$$

$$E_1 = -8\frac{t_a^2}{U} \tag{3.73}$$

Here the degeneracy is also broken, and the ground state is given by $|\Psi_1^2\rangle$ as defined in eq. (3.66).

3.3.2.2 Square With Diagonal Hopping

For four dots in a square, with diagonal hopping, we have

$$(-T^\dagger \Lambda^{-1} T)_0 = -\frac{t_a^2}{U}\begin{pmatrix} 8 & 4 \\ 4 & 8 \end{pmatrix} - \frac{t_d^2}{U+V}\begin{pmatrix} 4 & -4 \\ -4 & 4 \end{pmatrix} \tag{3.74}$$

$$E_0 = -12\frac{t_a^2}{U} \tag{3.75}$$

where $U \equiv U_0 - V_a$ and $V \equiv V_a - V_d$. For spin 1,

$$(-T^\dagger \Lambda^{-1} T)_1 = -\frac{t_a^2}{U}\begin{pmatrix} 4 & 0 & 0 \\ 0 & 8 & 0 \\ 0 & 0 & 4 \end{pmatrix} - \frac{t_d^2}{U+V}\begin{pmatrix} 4 & 0 & 0 \\ 0 & 0 & 0 \\ 0 & 0 & 4 \end{pmatrix} \tag{3.76}$$

$$E_1 = -8\frac{t_a^2}{U} \tag{3.77}$$

Interestingly, diagonal hopping for a square does not affect the ground state energies E_0 or E_1, and only serves to decrease the energy of the excited states. This can be understood by noticing that in each of the ground states, spins at opposite corners of the square (dots 1 and 3 or dots 2 and 4) only occur in a triplet configuration. This is necessary to allow adjacent spins to anti-align as much as possible.

3.3.2.3 Rectangle

For four dots in a rectangle, with no diagonal hopping, we have

$$(-T^\dagger \Lambda^{-1} T)_0 = -4 \begin{pmatrix} \frac{t_a^2}{U} + \frac{t_b^2}{U+V} & \frac{t_a^2}{U} e^{\frac{-\pi i}{3}} + \frac{t_b^2}{U+V} e^{\frac{\pi i}{3}} \\ \frac{t_a^2}{U} e^{\frac{\pi i}{3}} + \frac{t_b^2}{U+V} e^{\frac{-\pi i}{3}} & \frac{t_a^2}{U} + \frac{t_b^2}{U+V} \end{pmatrix} \tag{3.78}$$

$$E_0 = -4\left[\frac{t_a^2}{U} + \frac{t_b^2}{U+V} + \sqrt{\frac{t_a^4}{U^2} + \frac{t_b^4}{(U+V)^2} - \frac{t_a^2 t_b^2}{U(U+V)}}\right] \tag{3.79}$$

where $U \equiv U_0 - V_a$, and $V \equiv V_a - V_b$. For spin 1,

$$(-T^\dagger \Lambda^{-1} T)_1 = -4\left[\frac{t_a^2}{U} + \frac{t_b^2}{U+V}\right] \not{1} + 4 \begin{pmatrix} \frac{t_a^2}{U} & 0 & 0 \\ 0 & 0 & 0 \\ 0 & 0 & \frac{t_b^2}{U+V} \end{pmatrix} \tag{3.80}$$

$$E_1 = -4\left[\frac{t_a^2}{U} + \frac{t_b^2}{U+V}\right] \tag{3.81}$$

We note that the spin 1 ground state remains the same as in the square case, while the spin 0 ground state rotates, essentially in such a way as to include a greater weight to singlets across

the shorter edge of the rectangle than the longer edge. This must be the case, as when $t_b \to 0$, the ground state must become two spin singlets.

3.3.2.4 Rectangle With Diagonal Hopping

For four dots in a rectangle, with diagonal hopping, we have

$$(-T^\dagger \Lambda^{-1} T)_0 = -4 \begin{pmatrix} \frac{t_a^2}{U} + \frac{t_b^2}{U+V} + \frac{t_d^2}{U+W} & \frac{t_a^2}{U} e^{\frac{-\pi i}{3}} + \frac{t_b^2}{U+V} e^{\frac{\pi i}{3}} - \frac{t_d^2}{U+W} \\ \frac{t_a^2}{U} e^{\frac{\pi i}{3}} + \frac{t_b^2}{U+V} e^{\frac{-\pi i}{3}} - \frac{t_d^2}{U+W} & \frac{t_a^2}{U} + \frac{t_b^2}{U+V} + \frac{t_d^2}{U+W} \end{pmatrix} \tag{3.82}$$

$$\begin{aligned} E_0 = -4 \Bigg[& \frac{t_a^2}{U} + \frac{t_b^2}{U+V} + \frac{t_d^2}{U+W} \\ & + \left(\frac{t_a^4}{U^2} + \frac{t_b^4}{(U+V)^2} + \frac{t_d^4}{(U+W)^2} \right. \\ & \left. - \frac{t_a^2 t_b^2}{U(U+V)} - \frac{t_a^2 t_d^2}{U(U+W)} - \frac{t_b^2 t_d^2}{(U+V)(U+W)} \right)^{1/2} \Bigg] \end{aligned} \tag{3.83}$$

where $U \equiv U_0 - V_a$, $V \equiv V_a - V_b$, and $W = V_a - V_d$. For spin 1,

$$(-T^\dagger \Lambda^{-1} T)_1 = -4 \left[\frac{t_a^2}{U} + \frac{t_b^2}{U+V} + \frac{t_d^2}{U+W} \right] \mathbb{1} + 4 \begin{pmatrix} \frac{t_a^2}{U} & 0 & 0 \\ 0 & \frac{t_d^2}{U+W} & 0 \\ 0 & 0 & \frac{t_b^2}{U+V} \end{pmatrix} \tag{3.84}$$

$$E_1 = -4 \left[\frac{t_a^2}{U} + \frac{t_b^2}{U+V} \right] \tag{3.85}$$

Again the the spin 1 ground state is unaffected by the presence of diagonal hopping, for

the same reason discussed above. However, the diagonal hopping terms do affect the spin 0 state, since the imbalance between t_a and t_b causes opposite spins to no longer only appear in triplets.

3.3.2.5 Linear Array

For four dots in a line, we have

$$(-T^\dagger \Lambda^{-1} T)_0 = \\ -2t_a^2 \begin{pmatrix} \frac{1}{U}+\frac{1}{U+2V}+\frac{1}{U+V} & (\frac{1}{U}+\frac{1}{U+2V})e^{\frac{-\pi i}{3}}+\frac{e^{\frac{\pi i}{3}}}{U+V} \\ (\frac{1}{U}+\frac{1}{U+2V})e^{\frac{\pi i}{3}}+\frac{e^{\frac{-\pi i}{3}}}{U+V} & \frac{1}{U}+\frac{1}{U+2V}+\frac{1}{U+V} \end{pmatrix} \tag{3.86}$$

$$E_0 = -2t_a^2 \Big[\frac{1}{U} + \frac{1}{U+2V} + \frac{1}{U+V} \\ + \sqrt{(\frac{1}{U}+\frac{1}{U+2V})^2 + \frac{1}{(U+V)^2} - \frac{1}{U+V}(\frac{1}{U}+\frac{1}{U+2V})} \Big] \tag{3.87}$$

where $U \equiv U_0 - 2V_a + V_{3a}$, and $V \equiv V_a - V_{3a}$. For spin 1,

$$(-T^\dagger \Lambda^{-1} T)_1 = -2t_a^2 \Big[\frac{1}{U} + \frac{1}{U+2V} + \frac{1}{U+V} \Big] \not{1} \\ + 2t_a^2 \begin{pmatrix} \frac{1}{U}+\frac{1}{U+2V} & \frac{1}{U+V} & 0 \\ \frac{1}{U+V} & 0 & 0 \\ 0 & 0 & \frac{1}{U+V} \end{pmatrix} \tag{3.88}$$

$$E_1 = \frac{-t_a^2}{U} - \frac{t_a^2}{U+2V} - \frac{2t_a^2}{U+V} \\ - t_a^2 \sqrt{(\frac{1}{U}+\frac{1}{U+2V})^2 + \frac{4}{(U+V)^2}} \tag{3.89}$$

In the limit where $V \to 0$, this reduces to $E_0 = -(6+2\sqrt{3})t_a^2/U$ and $E_1 = -(4+$

$2\sqrt{2})t_a^2/U$.

3.3.2.6 Y-Shaped Configuration

For four dots in a Y-shaped configuration, we have

$$(-T^\dagger \Lambda^{-1} T)_0 = -\Big(\frac{t_a^2}{U} + \frac{t_a^2}{U+4V}\Big) \begin{pmatrix} 3 & 0 \\ 0 & 3 \end{pmatrix} \tag{3.90}$$

$$E_0 = -3\Big(\frac{t_a^2}{U} + \frac{t_a^2}{U+4V}\Big) \tag{3.91}$$

where $U \equiv U_0 - 3V_a + 2V_d$ and $V \equiv V_a - V_d$. Thus, the $|\Psi_0^{\pm}\rangle$ degeneracy remains unbroken, due to the three-fold rotational symmetry of the system. For spin 1,

$$(-T^\dagger \Lambda^{-1} T)_1 = \Big(\frac{t_a^2}{U} + \frac{t_a^2}{U+4V}\Big) \begin{pmatrix} -2 & -1 & 1 \\ -1 & -2 & 1 \\ 1 & 1 & -2 \end{pmatrix} \tag{3.92}$$

$$E_1 = -4\Big(\frac{t_a^2}{U} + \frac{t_a^2}{U+4V}\Big) \tag{3.93}$$

Interestingly, the ground state is the spin 1 state rather than the spin 0 state. This state is given by:

$$|\Psi_1\rangle = \frac{1}{2\sqrt{3}}\Big[\,|\uparrow\uparrow\uparrow\downarrow\rangle + |\uparrow\uparrow\downarrow\uparrow\rangle + |\uparrow\downarrow\uparrow\uparrow\rangle - 3\,|\downarrow\uparrow\uparrow\uparrow\rangle\,\Big] \tag{3.94}$$

which is the state maximizes the weight of the spin configuration where the center electron has opposite spin as the three corner electrons. Thus, the ground state can be thought of as antiferromagnetic in the sense that adjacent spins are anti-aligned; however, since there is an

imbalance in the number of sites in the odd and even sublattices, assigning alternating spins to these sites causes a total spin of 1 rather than 0.

3.3.2.7 Y-Shaped Configuration with N.N.N. Hopping

For four dots in a Y-shaped configuration, with next nearest neighbor hopping (that is hopping between the outer corners), we have

$$(-T^{\dagger}\Lambda^{-1}T)_0 = -\Big(\frac{t_a^2}{U} + \frac{t_a^2}{U+4V} + \frac{2t_d^2}{U+3V}\Big)\begin{pmatrix} 3 & 0 \\ 0 & 3 \end{pmatrix} \tag{3.95}$$

$$E_0 = -3\Big(\frac{t_a^2}{U} + \frac{t_a^2}{U+4V} + \frac{2t_d^2}{U+3V}\Big) \tag{3.96}$$

where $U \equiv U_0 - 3V_a + 2V_d$ and $V \equiv V_a - V_d$. For spin 1,

$$\begin{aligned}(-T^{\dagger}\Lambda^{-1}T)_1 = &-2\Big(\frac{t_a^2}{U} + \frac{t_a^2}{U+4V} + \frac{2t_d^2}{U+3V}\Big)\not{\mathbb{1}} \\ &+ \Big(\frac{t_a^2}{U} + \frac{t_a^2}{U+4V} - \frac{2t_d^2}{U+3V}\Big)\begin{pmatrix} 0 & -1 & 1 \\ -1 & 0 & 1 \\ 1 & 1 & 0 \end{pmatrix}\end{aligned} \tag{3.97}$$

$$E_1 = -4\Big(\frac{t_a^2}{U} + \frac{t_a^2}{U+4V}\Big) \tag{3.98}$$

Here the presence of next nearest neighbor hopping reduces the energy of the spin 0 states, while still maintaining the $|\Psi_0^{\pm}\rangle$ degeneracy, as the three-fold symmetry of the system remains unbroken. The next nearest neighbor hopping terms do not affect the spin 1 ground state, however, as the spins in any of the two corners only appear in triplet configurations. Thus, as t_d is increased

there exists a crossover point between E_0 and E_1. $E_1 < E_0$ as long as $\frac{6t_d^2}{U+3V} < \frac{t_a^2}{U} + \frac{t_a^2}{U+4V}$.

3.3.3 Summary

We have calculated the energies of the lowest energy spin 0 and spin 1 state for half-filled band in several different four-dot geometries to first order in t^2/U. In each case, the ground state is antiferromagnetic; however, with the Y-shaped configuration, alternating spins on each cite causes a total spin of 1 rather than 0, because there are 3 corner dots and only 1 center dot. Adding next nearest neighbor interactions reduces the energy difference between the two states, up to a critical strength at which point the spin 0 state becomes the ground state. We summarize these findings in table 3.2.

Sec. num.	dot config.	nnn. hop.	E_0 to order t^2/U	E_1 to order t^2/U	E_2	$E_1 < E_0$?
1	square	no	$-12t_a^2/U$	$-8t_a^2/U$	0	no
2	square	yes	$-12t_a^2/U$	$-8t_a^2/U$	0	no
3	rectangle	no	$\frac{-4t_a^2}{U} - \frac{4t_b^2}{U+V} - 4\sqrt{\frac{t_a^4}{U^2} + \frac{t_b^4}{(U+V)^2} - \frac{t_a^2 t_b^2}{U(U+V)}}$	$\frac{-4t_a^2}{U} - \frac{4t_b^2}{U+V}$	0	no
4	rectangle	yes	$-4\begin{pmatrix} \frac{-4t_a^2}{U} - \frac{4t_b^2}{U+V} - \frac{4t_d^2}{U+W} \\ \frac{t_a^4}{U^2} + \frac{t_b^4}{(U+V)^2} + \frac{t_d^4}{(U+W)^2} \\ -\frac{t_a^2 t_b^2}{U(U+V)} - \frac{t_a^2 t_d^2}{U(U+W)} - \frac{t_b^2 t_d^2}{(U+V)(U+W)} \end{pmatrix}^{\frac{1}{2}}$	$\frac{-4t_a^2}{U} - \frac{4t_b^2}{U+V}$	0	no
5	linear	no	$\frac{-2t_a^2}{U} - \frac{2t_a^2}{U+2V} - \frac{2t_a^2}{U+V} - 2t_a^2\begin{pmatrix} \left(\frac{1}{U} + \frac{1}{U+2V}\right)^2 + \frac{1}{(U+V)^2} \\ -\frac{1}{U+V}\left(\frac{1}{U} + \frac{1}{U+2V}\right) \end{pmatrix}^{1/2}$	$\frac{-t_a^2}{U} - \frac{t_a^2}{U+2V} - \frac{2t_a^2}{U+V} - t_a^2\sqrt{\left(\frac{1}{U} + \frac{1}{U+2V}\right)^2 + \frac{4}{(U+V)^2}}$	0	no
6	Y-shaped	no	$-3\left(\frac{t_a^2}{U} + \frac{t_a^2}{U+4V}\right)$	$-4\left(\frac{t_a^2}{U} + \frac{t_a^2}{U+4V}\right)$	0	yes
7	Y-shaped	yes	$-3\left(\frac{t_a^2}{U} + \frac{t_a^2}{U+4V} + \frac{2t_d^2}{U+3V}\right)$	$-4\left(\frac{t_a^2}{U} + \frac{t_a^2}{U+4V}\right)$	0	if $\frac{6t_d^2}{U+3V} < \frac{t_a^2}{U} + \frac{t_a^2}{U+4V}$

Table 3.2: A summary of the analytical results obtained for four electrons in four-dot plaquettes of various geometries. Here U is given by $U = U_0 - V_a$ in sec. 1-4, $U = U_0 - 2V_a + V_{3a}$ in sec. 5, and $U = U_0 - 3V_a + 2V_d$ in sec. 6 and 7. Additionally V is given by $V = V_a - V_b$ in sec. 3 and 4, $V = V_a - V_{3a}$ in sec. 5, and $V_a - V_d$ in sec. 6 and 7. Finally, $W = V_a - V_d$.

3.4 Four Electrons in Five Dots

3.4.1 Model

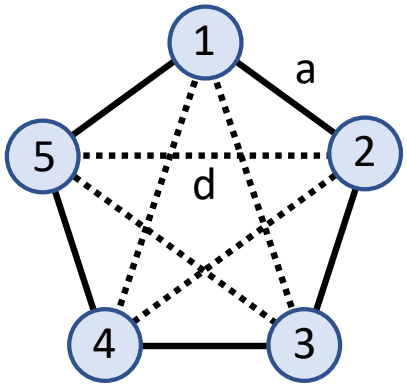

Figure 3.9: A depiction of a ring of 5 dots. Solid lines depict nearest-neighbor hopping terms and Coulomb interactions, and dashed lines long-range Coulomb interactions.

We now consider a ring of five dots with four electrons, as depicted in fig. 3.9. This does not satisfy the Nagaoka condition, and thus we do not predict the ground state to be ferromagnetic. The Hamiltonian is given by eq. (3.1), with t_{ij} and V_{ij} given as follows:

$$t_{ij} = \begin{cases} -t_a & \text{if } i-j = \pm 1 \mod 5 \\ 0 & \text{otherwise} \end{cases} \tag{3.99}$$

$$V_{ij} = \begin{cases} V_a & \text{if } i-j = \pm 1 \mod 5 \\ V_d & \text{if } i-j = \pm 2 \mod 5 \end{cases} \tag{3.100}$$

Up to symmetry, only one low energy electron configuration is possible. There are also

three high energy configurations that are connected to the low energy states by a single tunneling operation. These are:

$$\begin{aligned}
&(1,1,1,1,0) \text{ with energy: } 3V_a + 3V_d \\
&(2,0,1,1,0) \text{ with energy: } U_0 + V_a + 4V_d \\
&(2,1,0,1,0) \text{ with energy: } U_0 + 2V_a + 3V_d \\
&(2,1,1,0,0) \text{ with energy: } U_0 + 3V_a + 2V_d
\end{aligned} \tag{3.101}$$

We shift the total energy of the Hamiltonian by $3V_a + 3V_d$, and define U and V as:

$$\begin{aligned}
U &\equiv U_0 - 2V_a + V_d \\
V &\equiv V_a - V_d
\end{aligned} \tag{3.102}$$

so that the energies of the electrons configurations in eq. (3.101) become 0, U, $U+V$, and $U+2V$ respectively.

3.4.2 Ground State Calculation

3.4.2.1 Spin 2

We proceed in a similar fashion as above. For spin 2, there are five states for each value of S_z corresponding to the position of the hole, since there is only one spin configuration for a given

value of S_z that has spin 2. For $S_z = 2$, these states are:

$$|\uparrow\uparrow\uparrow\uparrow 0\rangle\,,\;\; |\uparrow\uparrow\uparrow 0\uparrow\rangle\,,\;\; |\uparrow\uparrow 0\uparrow\uparrow\rangle\,,\;\; |\uparrow 0\uparrow\uparrow\uparrow\rangle\,,\;\; |0\uparrow\uparrow\uparrow\uparrow\rangle \tag{3.103}$$

In this basis, the spin 2 Hamiltonian is given as follows:

$$H_2 = -t_a \begin{pmatrix} 0 & 1 & 0 & 0 & -1 \\ 1 & 0 & 1 & 0 & 0 \\ 0 & 1 & 0 & 1 & 0 \\ 0 & 0 & 1 & 0 & 1 \\ -1 & 0 & 0 & 1 & 0 \end{pmatrix} \tag{3.104}$$

Here the sign in the (1,5) elements is due to Fermi exchange statistics. There are two degenerate ground states to this Hamiltonian given by:

$$|\Psi_2^{\pm}\rangle = \frac{1}{\sqrt{5}} \begin{pmatrix} 1 & e^{\pm\frac{\pi i}{5}} & e^{\pm\frac{2\pi i}{5}} & e^{\pm\frac{3\pi i}{5}} & e^{\pm\frac{4\pi i}{5}} \end{pmatrix}^T \tag{3.105}$$

with energy:

$$E_2 = -\frac{1+\sqrt{5}}{2} t_a \tag{3.106}$$

3.4.2.2 Spin 1

We now consider the spin 1 subspace. We define the following spin configurations:

$$|\psi_1^j\rangle = \frac{1}{2}\Big[\; |\uparrow\uparrow\uparrow\downarrow\rangle + e^{j\frac{\pi i}{2}} \, |\uparrow\uparrow\downarrow\uparrow\rangle$$

$$+ e^{2j\frac{\pi i}{2}} |\uparrow\downarrow\uparrow\uparrow\rangle + e^{3j\frac{\pi i}{2}} |\downarrow\uparrow\uparrow\uparrow\rangle \Big] \tag{3.107}$$

for j between 1 and 3. We see that cycling the spins will return the same state with an extra phase $e^{j\frac{\pi i}{2}}$. The orbital part will be similar to the spin 2 case discussed above, and thus the spin 1 Hamiltonian will be given by a block-diagonal matrix, with blocks given as follows:

$$H_1^j = -t_a \begin{pmatrix} 0 & 1 & 0 & 0 & -e^{j\frac{\pi i}{2}} \\ 1 & 0 & 1 & 0 & 0 \\ 0 & 1 & 0 & 1 & 0 \\ 0 & 0 & 1 & 0 & 1 \\ -e^{-j\frac{\pi i}{2}} & 0 & 0 & 1 & 0 \end{pmatrix} \tag{3.108}$$

This has a nondegenerate ground state with energy $E_1 = -2t_a$. The ground state has spin configuration given by $|\psi_1^2\rangle$, and orbital part $\frac{1}{\sqrt{5}}(1\ 1\ 1\ 1\ 1)^T$.

3.4.2.3 Spin 0

Finally, we examine the spin 0 subspace. There are two spin configurations, which we define as follows:

$$|\psi_0^0\rangle = \frac{1}{2\sqrt{3}} \Big[- |\uparrow\uparrow\downarrow\downarrow\rangle + 2\,|\uparrow\downarrow\uparrow\downarrow\rangle - |\uparrow\downarrow\downarrow\uparrow\rangle \\ - |\downarrow\uparrow\uparrow\downarrow\rangle + 2\,|\downarrow\uparrow\downarrow\uparrow\rangle - |\downarrow\downarrow\uparrow\uparrow\rangle \Big] \tag{3.109}$$

$$|\psi_0^1\rangle = \frac{1}{2} \Big[|\uparrow\uparrow\downarrow\downarrow\rangle - |\uparrow\downarrow\downarrow\uparrow\rangle - |\downarrow\uparrow\uparrow\downarrow\rangle + |\downarrow\downarrow\uparrow\uparrow\rangle \Big] \tag{3.110}$$

We note that cycling the spins of $|\psi_0^j\rangle$ returns the same state with an additional phase $(-1)^j |\psi_0^j\rangle$. The the spin 0 Hamiltonian will be a block-diagonal matrix with blocks:

$$H_0^j = -t_a \begin{pmatrix} 0 & 1 & 0 & 0 & (-1)^{j+1} \\ 1 & 0 & 1 & 0 & 0 \\ 0 & 1 & 0 & 1 & 0 \\ 0 & 0 & 1 & 0 & 1 \\ (-1)^{j+1} & 0 & 0 & 1 & 0 \end{pmatrix} \tag{3.111}$$

This also has a nondegenerate ground state with energy $E_0 = -2t_a$. This state has spin configuration given by $|\psi_0^1\rangle$, and orbital part $\frac{1}{\sqrt{5}}(1\ 1\ 1\ 1\ 1)^T$.

3.4.2.4 Finite U Corrections

As before, the spin 2 energy is exact for finite U, since the Pauli exclusion principle forbids any other states than the five examined. Additionally, since neither the spin 1 nor spin 0 ground states are degenerate with other states of the same spin, we simply use nondegenerate perturbation theory to calculate the leading order correction to the energy. We find that to order t^2/U, the energy of the lowest energy spin 1 state is given by:

$$E_1 = -2t_a - 4\frac{t_a^2}{U} - 2\frac{t_a^2}{U+V} - 2\frac{t_a^2}{U+2V} + O\Big(\frac{t_a^3}{U^2}\Big) \tag{3.112}$$

and the energy of the lowest energy spin 0 state is given by:

$$E_0 = -2t_a - 2\frac{t_a^2}{U} - \frac{t_a^2}{U+V} - \frac{t_a^2}{U+2V} + O\Big(\frac{t_a^3}{U^2}\Big) \tag{3.113}$$

Thus, for finite U, the ground state of the system is the spin 1 state. This means the ground state is partially ferromagnetic.

3.5 Conclusion

We have theoretically considered 4-dot quantum arrays in several different geometries investigating analytically within a simple, but semi-realistic, model the existence or not of Nagaoka-type ferromagnetic ground states. Our work includes distant-neighbor hopping and distant-neighbor Coulomb coupling within a one orbital (with two spins) per dot model. Although the interaction is always finite in our system we find several situations where Nagaoka-type ferromagnetism should emerge provided the kinetic and potential energies obey certain constraints (which we derive). We calculate the spin gap for our system, and obtain the energy difference between the lowest-energy ferromagnetic state and lowest-energy nonferromagnetic state. We also provide results for a 5-dot ring with 4 electrons, finding a partially ferromagnetic ground state. We believe that our predictions are experimentally testable in currently available quantum dot arrays as long as there is sufficient control over the system (i.e. hopping matrix elements, number of electrons in the system) and the temperature is low. In principle, one can try to numerically calculate the hopping and the interaction matrix elements for a given system of coupled dots to make the prediction quantitative. We, however, do not believe that such an endeavor, which would be numerically very demanding involving large configuration interaction calculations [111, 112, 113] for the coupled dot system, is particularly useful since the necessary information for the quantum confinement in each dot is unknown and therefore, the results would be numerically unreliable. Since all the matrix elements of hopping and interaction entering the model are likely to be ex-

ponentially sensitive to the unknown dot confinement potential, our phenomenological approach using model parameters based on a delta function confinement model is likely to have reasonable qualitative accuracy. In particular, our specific predictions on which geometry would lead to ferromagnetism and which would not and the conditions necessary for obtaining full or partial ferromagetism in the ground states of different arrays should motivate experiments in current semiconductor dot based qubit structures where the observation of different types of nontrivial magnetic ground states could be construed as quantum emulation of interacting Hamiltonians in small systems. We think that the experimental control already achieved in the laboratory for semiconductor qubit systems should enable the community to see various magnetic ground states in quantum dot plaquettes as predicted in our theory.

Chapter 4: Flatband Ferromagnetism

The Hubbard model [58] was originally formulated with the goal of explaining the existence of ferromagnetism in common transition metals. The tight-binding Hamiltonian simplistically describes screened electron-electron interactions in a narrow-band metal with the use of only two parameters: the tunneling constant between lattice sites t_{ij}, and the onsite Coulomb repulsion energy U, as seen in Eq. (4.1):

$$H = \sum_{i,j} \sum_{s \in \{\uparrow,\downarrow\}} -t_{ij} c_{is}^{\dagger} c_{js} + \sum_{i} \frac{U}{2} n_i (n_i - 1) \tag{4.1}$$

where i, j are summed over the lattice sites. Despite the simplicity of the Hubbard model, no general solution is known, and while some progress has been made, a complete description of ferromagnetism using this model has not been found after 60 years. However, ferromagnetism has been rigorously proven to occur in the Hubbard model in two very specific instances, namely Nagaoka ferromagnetism and flatband ferromagnetism.

One specific situation where the Hubbard model can be proven to exhibit ferromagnetism is when one electron is added to a half-filled band. This result, proven by Nagaoka, requires that $U \gg t_{ij}$, $t_{ij} \geq 0$, and that the lattice be sufficiently connected [62]. Nagaoka ferromagnetism is a somewhat surprising result when considering that for an exactly half-filled band, the Hubbard model reduces to the Heisenberg model, which generally exhibits antiferromagnetism; yet

the addition of a single electron is proven to completely change the magnetic phase. This exact finding of Nagaoka suggests that the Hubbard model, in spite of its apparent simplicity and its seeming dependence on a single effective dimensionless interaction parameter U/t, is extremely rich and subtle, since just adding one particle to the half-filled state changes the ground state from being an antiferromagnetic insulator to a ferromagnetic metal. The model is considered to be the paradigmatic model of strong correlations in many body interacting systems, and is foundational in theoretical studies of many phenomena such as Mott transition, ferromagnetism and antiferromagnetism, narrow band systems, high-T_c cuprate superconductivity, spin liquids, etc. Recently, Nagaoka ferromagnetism has been experimentally observed in a small plaquette of four quantum dots which simulates the Hubbard model [9]. In an earlier work, we studied Nagaoka ferromagnetism in small quantum dot plaquettes theoretically [110], connecting with this recent experiment [9] and establishing the continued validity of Nagaoka-type ferromagnetism in the Hubbard model even when some of the stringent conditions of the original work [62] are relaxed. The idea that the Hubbard model can be simulated by quantum dot plaquettes has been proposed decades ago [59, 60, 61], but current technologies [9, 11, 114] are capable of realizing these experiments now or in the near future. In fact, the laboratory emulation of the Hubbard model and the associated Mott transition reflected in the observation of the collective Coulomb blockade in a recent experiment on a few quantum dots establish the exquisite control and measurement capability achieved in solid state nanostructures inspired by experimental advances in the semiconductor spin qubit quantum computing platforms [101]. Such experiments should enable direct laboratory simulations of the Hubbard model in small lattices of a few electrons. Although our work is entirely theoretical and quite mathematical in nature, we have been inspired by the rapid recent experimental advance in semiconductor spin qubit platforms consisting of quantum dot ar-

rays, which should enable an experimental verification of our exact (and counter-intuitive) results for the Hubbard model.

In specific cases, the Hubbard model can also exhibit a different type of ferromagnetism (i.e. distinct from Nagaoka ferromagnetism) known as flat-band ferromagnetism [63]. This in principle can occur when there is degeneracy in the lowest or highest-energy single particle states; however, due to the Perron-Frobenius theorem, for positive t_{ij} the lowest-energy state of a connected lattice is always nondegenerate. Thus flat-band ferromagnetism can occur only when there are degenerate high-energy states. Because flat-band ferromagnetism involves holes filling in an otherwise filled band, it is convenient to use the particle-hole transformation $\tilde{c}_{is} = c_{is}^{\dagger}$, where $\tilde{c}_{is}$ is the hole annihilation operator. Under this transformation, Eq. (4.1) becomes as follows, up to a constant energy shift:

$$H = \sum_{i,j} \sum_{s\in\{\uparrow,\downarrow\}} t_{ij}\tilde{c}_{is}^{\dagger}\tilde{c}_{js} + \sum_{i} \frac{U}{2}\tilde{n}_i(\tilde{n}_i - 1) \tag{4.2}$$

The weak flatband ferromagnetism theorem is as follows:

Consider the Hubbard model Eq. (4.2) such that the single-hole ground state is k-fold degenerate. Then for h holes, with $h \leq k$, the ferromagnetic ground state energy will be less than or equal to the energy of any nonferromagnetic state.

The proof of this statement [63] follows a similar line of reasoning as Hund's rule. The ferromagnetic ground state consists of the holes filling h of the k degenerate states, and the ground energy corresponds to h times the energy of these states. Because of the Pauli exclusion principle, there will be no doubly-occupied lattice sites, and thus there will be no contribution from the onsite interaction term. Nonferromagnetic states can at best match the same energy,

but the onsite interaction term could potentially increase the energy of the states, since doubly-occupied lattice sites are no longer forbidden by the Pauli exclusion principle.

This theorem does not by itself guarantee ferromagnetism, since the inequality between the ferromagnetic ground state energy and the nonferromagnetic energies is not a strict inequality. There have been many works showing that the inequality is strict in certain classes of lattice geometries [63, 115, 116, 117]; however, it is not known in general for which cases or under what prescribed conditions there will be a unique ferromagnetic ground state.

In this chapter we present two results. In Sec. 4.1, we give a mathematical theorem which prescribes certain conditions under which there will be ferromagnetic and antiferromagnetic degeneracy. This theorem is only applicable for a small number of holes, but is independent of geometry, relying only on the number of lattice sites, holes, and flatband single-particle states. In Sec. 4.2, we give an example of a 6-dot configuration where the ground state is ferromagnetic despite not having any degenerate flatband single-particle states. This is, therefore, an example in which ferromagnetism in the Hubbard model can exist without having any band induced single-particle degeneracy. Additionally, the lowest-energy antiferromagnetic state does not doubly-occupy the single-particle ground state as one might expect, instead doubly occupying a higher energy state. Finally, in Sec. 4.3, we give our conclusions, briefly noting in particular that the examples we present are experimentally accessible with current quantum dot technologies, each requiring only a few quantum dots. The contents of this chapter have been submitted for publication, and are available as a preprint in Ref. [118].

4.1 Flat Band Ferromagnetic and Nonferromagnetic Degeneracy

Although it is not known in general which lattice geometries and filling factors are strictly ferromagnetic, it is interesting to ask the converse: are there cases where it is known with certainty that the ferromagnetic ground state is degenerate with nonferromagnetic ground states? We discuss cases where this is true and present a general combinatorics-based theoretical result which is completely geometry-independent, although to apply it to specific physical situations requires rather strict conditions on the number of states and holes present in the system.

One simple case where flatband ferromagnetic states can be shown to be degenerate with nonferromagnetic states is when the degenerate flatband states are local. In this case, multiple nonoverlapping local states can be filled with any spin configuration without having any doubly occupied dots. Then the interaction term of the Hamiltonian will not contribute to ground state energy, and thus there will be degenerate ferrommagnetic and nonferromagnetic ground states. For example, in the Kagome lattice, single-hole ground states localize, occupying only six sites comprising one hexagon of the lattice. These local states can be filled with holes without overlap if the filling factor $\nu_h \leq 1/18$, and thus there will be degenerate ferromagnetic and nonferromagnetic ground states for these filling factors (note that Mielke proved a stronger statement [116] for $\nu_h \leq 1/6$, but this proof relies strictly on the fact that the Kagome lattice is a line graph, and is not extendable to other lattices). Another example is a small plaquette of dots forming a complete graph ($t_{ij} = t$ for any $i \neq j$). Here the single-hole ground states localize to just two dots, and there is ferromagnetic and nonferromagnetic degeneracy for any $\nu_h \leq 1/4$.

While having localized states often contributes to ground state degeneracy, there is a way that even completely nonlocal states can still lead to degeneracy. Holes can fill the degenerate

flat-band states in a number of ways, each leading to doubly occupied terms $\tilde{c}^{\dagger}_{i\uparrow}\tilde{c}^{\dagger}_{i\downarrow}$ in the full multiparticle many-body state. However, because there are many different ways these states can be filled, it is often possible to form linear combinations in which all doubly occupied terms cancel out. If this is possible, then there will be ferromagnetic and nonferromagnetic ground state degeneracy. In particular, if the number of distinct ways the flatband states can be filled N_f is greater than the number of possible doubly occupied terms N_d, then there will always exist a linear combination of flatband states that cancel out all doubly occupied terms. For a system with n lattice sites, k flatband states, h holes, and for a given total spin s, the quantities N_f and N_d are given as follows:

$$\begin{aligned} N_f &= \binom{k}{\frac{h}{2}+s}\binom{k}{\frac{h}{2}-s} - \binom{k}{\frac{h}{2}+s+1}\binom{k}{\frac{h}{2}-s-1} \\ N_d &= \binom{n}{\frac{h}{2}+s}\binom{n}{\frac{h}{2}-s} - \binom{n}{\frac{h}{2}+s+1}\binom{n}{\frac{h}{2}-s-1} \\ &\quad - \binom{n}{\frac{h}{2}+s}\binom{n-\frac{h}{2}-s}{\frac{h}{2}-s} + \binom{n}{\frac{h}{2}+s+1}\binom{n-\frac{h}{2}-s-1}{\frac{h}{2}-s-1} \end{aligned} \tag{4.3}$$

Then we have the following theorem:

Consider the Hubbard model Eq. (4.2) with n lattice sites such that the single-hole ground state is k-fold degenerate. Then for h holes and some total spin s, with $2s \leq h \leq k$, if the quantities given in eq. (4.3) satisfy $N_f > N_d$, then there will exist a spin s ground state that is degenerate with the ferromagnetic ground state.

While this theorem is completely general and geometry-independent, in practice the condition $N_f > N_d$ is somewhat difficult to satisfy, and thus the situations where it applies are somewhat limited. However, this theorem simplifies dramatically for the special case where there are

only two holes in the system, becoming as follows:

For 2 holes in the Hubbard model given by Eq. (4.2) with n lattice sites and k degenerate single-particle ground states, if $k(k+1)/2 > n$, then there will exist a spin 0 ground state that is degenerate with the spin 1 ground state.

There are several small configurations of sites which satisfy this condition, including a 4-site complete graph (tetrahedron), the 9-site $(2,3)$-Hamming graph, and a 13-site FCC-sublattice centered around a single site, among other configurations. In Appendix B, we calculate using exact diagonalization the lowest-energy states for each spin for these (and many other) plaquettes, illustrating that they do indeed satisfy the theorem we presented.

It is interesting to see how this theorem scales in the limit where the number of lattice sites n is very large. We will assume in this limit that the number of flatband states k scales proportionally with n. For $s = 0$, we use Sterling's approximation to simplify the expressions in Eq. 4.3, and find the following asymptotic behaviors of N_f and N_d:

$$\begin{aligned} N_f &\approx \frac{(k+1)^{\frac{h}{2}+1} k^{\frac{h}{2}-1}}{(\frac{h}{2}+1)!(\frac{h}{2})!} \sim k^h \\ N_d &\approx \frac{(n+1)^{\frac{h}{2}+1} n^{\frac{h}{2}-1} - n^{\frac{h}{2}}(n-\frac{h}{2})^{\frac{h}{2}}}{(\frac{h}{2}+1)!(\frac{h}{2})!} \sim n^{h-1} \end{aligned} \tag{4.4}$$

Then in the large n limit, the condition $N_f > N_d$ is met for $h < \log n / \log(n/k)$, and thus the maximum number of holes for which this theorem applies scales as $\log$ of the system size. Thus while this theorem is useful for studying small systems of quantum dot plaquettes with just a few sites (since $\log n$ is still comparable in magnitude with n in small systems), as the system size increases the number of holes for which it is valid drops off quickly compared to the total system size. In fact, this serves as an important reminder of the fact that small systems that can

be numerically or experimentally simulated cannot always be extrapolated to the thermodynamic limit, as there are effects that are quite strong for small systems which become negligible as the system size increases (in fact, Nagaoka ferromagnetism iself is a dramatic example of this effect also, obviously a filling with one electron or one hole away from half-filling makes no physical sense for a large system although it is a meaningful concept for a small system [110]). Other examples of this include the finite-size effect at the edges of a small lattice, but we have given an example which depends only on the number of states and lattice sites, which stems from the difference between $\log n$ and n.

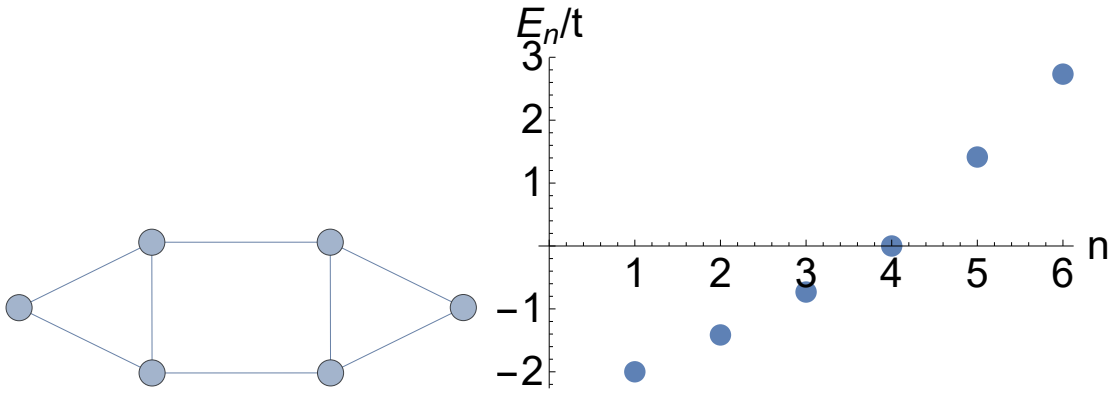

Figure 4.1: **Left:** 6-dot plaquette which exhibits unusual properties when filled with 3 holes. **Right:** Single-particle energy levels of the plaquette to the left ordered from lowest to highest energy. Note these energies include the effect of the particle-hole transformation, thus corresponding to Eq. (4.2).

4.2 Example of Holes Filling Higher Energy States

The basic intuition behind Hund's rule is that particles / holes will fill the lowest-energy single-particle states available first, and in the case of degeneracies will form a ferromagnetic spin configuration to avoid energy penalties from double-occupancy of sites. However, in the Hubbard model when $U \gg t$, there are cases where the system breaks this general rule, pre-

ferring to fill higher energy single-particle states than necessary in order to eliminate the onsite interaction energy from doubly occupied sites. Thus, strong correlation effects in the Hubbard model explicitly violate Hund's rule leading to counter-intuitive ground states. We give one such example below.

Consider the plaquette of six lattice sites shown in Fig. 4.1, with uniform tunneling constant t between nearest neighbors, and $U \gg t$. The single particle-energies for this system are nondegenerate and at a glance are somewhat evenly spaced, as shown in Fig. 4.1, although of course there is some anharmonicity. A simple application of Hund's rule would suggest that the ground state should be antiferromagnetic, as holes should attempt to fill the lowest energy state first before beginning to fill the higher energy states, and this is indeed the case when U is small compared to t. However when U becomes large, the antiferromagnetic ground state must include some contribution from higher-energy hole configurations, which in some cases can even exceed the energy benefit from doubly occupying the lowest-energy state. This is the case for three holes filling the six-site plaquette discussed above. Exact diagonalization yields a ferromagnetic ground state energy of $E_{3/2} = -4.146t$, whereas the lowest energy antiferromagnetic state has an energy given by:

$$E_{1/2} = -3.949t - 1.704t^2/U + O(t^3/U^2) \tag{4.5}$$

Thus in the large U limit, the system exhibits a type of "psuedo-flatband ferromagnetism" (and not antiferromagnetism) despite the single-particle states being nondegenerate.

This result becomes even more striking when considering the wavefunction of the lowest-energy antiferromagnetic state $|\Psi_{1/2}\rangle$. Specifically, we consider the product states of single particle eigenstates. These product states, which we denote by $|\phi_i\rangle$ are not necessarily eigenstates

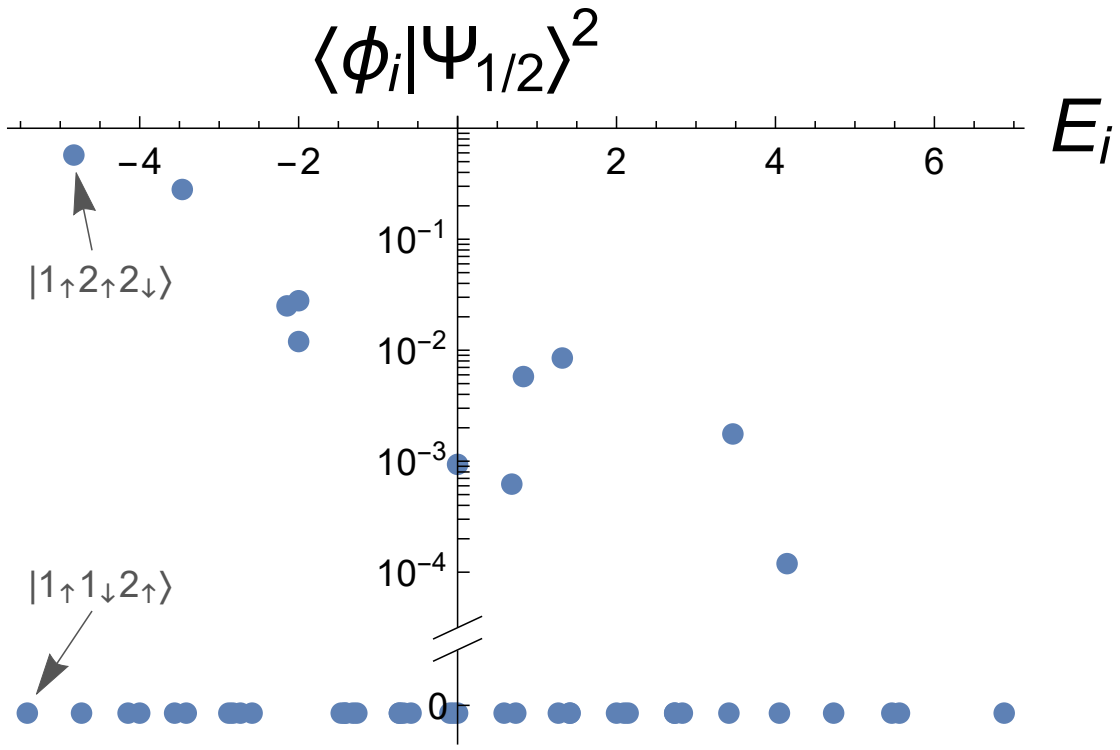

Figure 4.2: For each product state $|\phi_i\rangle$ of single-particle states, the energy of the state is plotted against the wavefunction overlap of $|\phi_i\rangle$ with the lowest-energy spin 1/2 state $|\Psi_{1/2}\rangle$. States at the bottom of the plot have overlap of exactly 0 because they are protected by symmetry.

themselves, and in general the eigenstates of the system will be linear combinations of the $|\phi_i\rangle$. However, it is often assumed (for example, in Hund's rule) that the ground state is simply the lowest-energy of these product states, and that electrons fill the single-particle states one at a time in order of increasing energy, with perhaps some small correction from interaction effects. However, for this specific configuration, this assumption breaks down entirely. In Fig. 4.2, we plot the energy of each of the product states $|\phi_i\rangle$ versus their overlap with $\Psi_{1/2}$. We find that $|\Psi_{1/2}\rangle$ has an overlap of exactly 0 with the lowest energy product state $|1_\uparrow 1_\downarrow 2_\uparrow\rangle$ (here we have notated the single-hole eigenstates from 1 to 6 in order of increasing energy). Instead, the lowest-energy antiferromagnetic state has a large overlap with the 'excited' state $|1_\uparrow 2_\uparrow 2_\downarrow\rangle$ as follows,

with the rest of the wavefunction being comprised of higher energy states:

$$\left|\langle \Psi_{1/2} | 1_\uparrow 2_\uparrow 2_\downarrow \rangle\right|^2 = 0.573 \tag{4.6}$$

The fact that the overlap with $|1_\uparrow 1_\downarrow 2_\uparrow\rangle$ is exactly 0 is due to the K_4 symmetry of the Hamiltonian (H is unchanged by π rotations about the x, y, and z axes). The states $|1_\uparrow 1_\downarrow 2_\uparrow\rangle$ and $|1_\uparrow 2_\uparrow 2_\downarrow\rangle$ fall under different symmetry classes, and thus eigenstates of H will not mix these two states. What is surprising is that the system prefers the higher energy of these two states $|1_\uparrow 2_\uparrow 2_\downarrow\rangle$, as this completely contradicts the naive assumption that the system will attempt to fill the lowest-energy single particle states first, only mixing with higher-energy states to eliminate terms corresponding to doubly occupied lattice sites. In this case, the system actually prefers to start with a slightly higher-energy state because it makes the cancellation of doubly-occupied lattice site terms easier. Again, this is a subtle and highly nontrivial correlation effect which cannot be captured in terms of any simple general rules based on single particle physics.

4.3 Conclusion

We give examples of two interesting and exact theoretical phenomena in the Hubbard model which require only a few (4-6) lattice sites. The first is a general geometry-independent theorem which has limited applicability (particularly, in the thermodynamic limit) but is mathematically exact. This theorem outlines certain cases of flatband ferromagnetism which necessarily have a nonferromagnetic state that is degenerate with the ferromagnetic ground state, relying only on the number of holes, lattice sites, and degenerate flatband states. The second example is a particular geometric arrangement of six sites which exhibits the unusual behavior where the

lowest-energy antiferromagnetic state has no overlap with the product state of the lowest-energy single-particle states, and the many-body ground state is ferromagmmetic rather than antiferromagnetic as implied by Hund's rule. Since these phenomena rely only on a small number of sites, these are good candidates to be observed in quantum dot experiments using current technologies. In particular, we believe both can be studied on existing quantum dot arrays associated with spin qubit platforms, directly experimentally establishing nontrivial many-body correlation effects in the Hubbard model ground states.

Chapter 5: Conclusion

Quantum Dot qubits have significant potential for the development of quantum information technologies due to their long coherence times, small size, and their integration with current semiconductor technologies. If fully realized, this technology could allow new topics of study to be opened by allowing computations to be performed which would take an exponential amount of time and resources to approach using classical computational techniques [17, 20, 21, 23]. Progress in creating and controlling quantum dot qubits still lags behind other current qubit schemes [6] due to the presence of noise in the systems. However, researchers have still been able to use quantum dot plaquettes to perform interesting and useful experiments [9].

Out of the various materials used to fabricate quantum dots, silicon-based devices have shown particular promise [10, 73]. However, the presence of valley degeneracy remains one significant obstacle to further progress in Si quantum dots. We provide an in-depth study of the dynamics of exchange-coupled quantum dots which have valley degrees of freedom. By using a perturbative approach which is completely analytical, we show that spin-valley entanglement can easily arise if the valley states are not carefully accounted for, and that this entanglement can hamper quantum information applications. Specifically, in the case where the valley splitting is large, quantum information stored in the spin states of electrons can become entangled with the valley states that the electron inhabits whenever electrons are not initialized to a valley eigenstate.

When the valley splitting is large, this is not particularly hard to circumvent, as it is straightforward to initialize electrons to the ground state, which is a valley eigenstate. Things become much more troublesome when the valley splitting is small, because it becomes difficult to control the initial valley states. In this case, spin-valley entanglement can arise whenever electrons are not initialized to the same valley state. However, this spin-valley entanglement cannot be detected in two-qubit systems with simply the exchange interaction and measurement along the initialization axis, but it will adversely affect systems with more qubits. Thus it may be possible for initial two-qubit experiments to miss the effects of spin-valley entanglement if not designed carefully.

Despite the slower progress compared to other qubit platforms, quantum dots are particularly useful in simulating condensed matter systems. Specifically, the Hamiltonian of quantum dot plaquettes approximates the Hubbard model, and such plaquettes can be arranged in order to test various geometric arrangements that might be difficult to fabricate otherwise. Many interesting theoretical phenomena are predicted to arise from the Hubbard model, including Nagaoka and flatband ferromagnetism [62, 63], and in fact Nagaoka ferromagnetism has been observed in quantum dot plaquettes [9]. We give a thorough theoretical analysis of a wide variety of geometric arrangements of quantum dots, and determine for which arrangements a ferromagnetic ground state can be expected. We examine the effects of long-range Coulomb interactions and long-range hopping on Nagaoka ferromagnetic ground states, both of which do not satisfy the conditions of Nagaoka's original theorem. We find that ferromagnetism is robust to the addition of long-range Coulomb interactions, but that long-range hopping destroys the ferromagnetism after passing a certain threshold, and we specifically calculate this threshold for a specific geometric arrangement of dots. We present a general, geometry-independent result detailing certain situations where flatband ferromagnetic ground states necessarily have degenerate nonferromag-

netic states, and we give an example of a specific geometric arrangement that seems to violate Hund's rule, where a configuration of higher-energy single-particle states has a lower total energy than the configuration of lowest-energy single-particle states. We also find other ferromagnetic and partially ferromagnetic states not explained by Nagaoka or flatband ferromagnetism. All of these phenomena require only a few quantum dots, and are potentially observable by current quantum dot experiments.

Appendix A: Derivation of Eqs. (2.3) & (2.6)

In this section we give the detailed derivation of Eqs. (2.3) & (2.6) beginning from the Hamiltonian H given by Eq. (2.1).

The Hubbard Hamiltonian H acts on a vector space of 8 single particle states, corresponding to every combination of choices for dot $j = |1\rangle$ or $|2\rangle$, valley state $v = |+\rangle$ or $|-\rangle$, and spin $s = |\uparrow\rangle$ or $|\downarrow\rangle$. We consider 2 electrons in this system, corresponding to $\binom{8}{2} = 28$ two-particle states. Because H commutes with the spin operators S^2 and S_z, spin is conserved, and H can be divided into the following four noninteracting blocks corresponding to the total spin of the system: the singlet subspace, which consists of 10 states; and three triplet subspaces with $S_z = -1$, 0, or 1, each of which consisting of 6 states. The three triplet subspaces are identical up to the value of S_z, so we focus only on one of them (where $S_z = 0$). The six triplet states are as follows:

$$
\begin{aligned}
|1_+1_-\rangle &= \frac{c^\dagger_{1,+,\uparrow}c^\dagger_{1,-,\downarrow} + c^\dagger_{1,+,\downarrow}c^\dagger_{1,-,\uparrow}}{\sqrt{2}}\,|0\rangle \\
|1_+2_+\rangle &= \frac{c^\dagger_{1,+,\uparrow}c^\dagger_{2,+,\downarrow} + c^\dagger_{1,+,\downarrow}c^\dagger_{2,+,\uparrow}}{\sqrt{2}}\,|0\rangle \\
|1_+2_-\rangle &= \frac{c^\dagger_{1,+,\uparrow}c^\dagger_{2,-,\downarrow} + c^\dagger_{1,+,\downarrow}c^\dagger_{2,-,\uparrow}}{\sqrt{2}}\,|0\rangle \\
|1_-2_+\rangle &= \frac{c^\dagger_{1,-,\uparrow}c^\dagger_{2,+,\downarrow} + c^\dagger_{1,-,\downarrow}c^\dagger_{2,+,\uparrow}}{\sqrt{2}}\,|0\rangle \\
|1_-2_-\rangle &= \frac{c^\dagger_{1,-,\uparrow}c^\dagger_{2,-,\downarrow} + c^\dagger_{1,-,\downarrow}c^\dagger_{2,-,\uparrow}}{\sqrt{2}}\,|0\rangle
\end{aligned}
$$

$$|2_+2_-\rangle = \frac{c^\dagger_{2,+,\uparrow}c^\dagger_{2,-,\downarrow} + c^\dagger_{2,+,\downarrow}c^\dagger_{2,-,\uparrow}}{\sqrt{2}}|0\rangle \tag{A.1}$$

where $|0\rangle$ is the "vacuum" state corresponding to the system with no electrons in either dot. Writing the Hamiltonian H in the basis given by Eq. (A.1) yields the following:

$$H_T = \begin{pmatrix} U+\epsilon & t_- & t_+ & -t_+ & -t_- & 0 \\ t_-^* & \Delta_1+\Delta_2 & 0 & 0 & 0 & -t_- \\ t_+^* & 0 & \Delta_1-\Delta_2 & 0 & 0 & t_+ \\ -t_+^* & 0 & 0 & -\Delta_1+\Delta_2 & 0 & -t_+ \\ -t_-^* & 0 & 0 & 0 & -\Delta_1-\Delta_2 & t_- \\ 0 & -t_-^* & t_+^* & -t_+^* & t_-^* & U-\epsilon \end{pmatrix} \tag{A.2}$$

Note that matrix elements corresponding to an electron moving from one valley state to the other in the same dot are 0, since the Hamiltonian is written in terms of the valley eigenstates $|+\rangle$ and $|-\rangle$. Some tunneling matrix elements such as $|1_+1_-\rangle \rightarrow |1_-2_-\rangle$ contain an additional minus sign due to Fermi statistics since the particle which does not tunnel (in this case 1_-) switches from the second position to the first position in the state definition (compare this to the matrix element $|1_+1_-\rangle \rightarrow |1_+2_+\rangle$, where 1_+ is in the first position in both states). Switching the position corresponds to commuting two creation operators, which produces a minus sign.

The $|1_+1_-\rangle$ and $|2_+2_-\rangle$ states contain 2 electrons in a single dot, which cause the states to have a much higher energy due to the onsite Coulomb interaction energy U. Thus these states will not directly affect the system dynamics; however, there will still be an indirect perturbative effect on the lower energy states and energies. To determine this effect we perform a routine

perturbation theory calculation with the unperturbed Hamiltonian $H_0 = \mathrm{diag}(U, 0, 0, 0, 0, U)$, and the perturbation H' consisting of the rest of the matrix elements in Eq. (A.2). Assuming $U \gg t_c, \Delta_j, \epsilon$, the first order correction in U^{-1} to the Hamiltonian is given by:

$$H_T = \begin{pmatrix} \Delta_1 + \Delta_2 - \frac{2|t_-|^2}{U} & \frac{t_- t_+^* - t_+ t_-^*}{U} & \frac{t_+ t_-^* - t_- t_+^*}{U} & \frac{2|t_-|^2}{U} \\ \frac{t_+ t_-^* - t_- t_+^*}{U} & \Delta_1 - \Delta_2 - \frac{2|t_+|^2}{U} & \frac{2|t_+|^2}{U} & \frac{t_- t_+^* - t_+ t_-^*}{U} \\ \frac{t_- t_+^* - t_+ t_-^*}{U} & \frac{2|t_+|^2}{U} & -\Delta_1 + \Delta_2 - \frac{2|t_+|^2}{U} & \frac{t_+ t_-^* - t_- t_+^*}{U} \\ \frac{2|t_-|^2}{U} & \frac{t_+ t_-^* - t_- t_+^*}{U} & \frac{t_- t_+^* - t_+ t_-^*}{U} & -\Delta_1 - \Delta_2 - \frac{2|t_-|^2}{U} \end{pmatrix} \tag{A.3}$$

where only the four low energy states are shown.

A similar process is carried out for the singlet space, where there are 10 total states:

$$\begin{aligned}
|1_+1_-\rangle &= \frac{c^\dagger_{1,+,\uparrow} c^\dagger_{1,-,\downarrow} - c^\dagger_{1,+,\downarrow} c^\dagger_{1,-,\uparrow}}{\sqrt{2}} |0\rangle \\
|1_+2_+\rangle &= \frac{c^\dagger_{1,+,\uparrow} c^\dagger_{2,+,\downarrow} - c^\dagger_{1,+,\downarrow} c^\dagger_{2,+,\uparrow}}{\sqrt{2}} |0\rangle \\
|1_+2_-\rangle &= \frac{c^\dagger_{1,+,\uparrow} c^\dagger_{2,-,\downarrow} - c^\dagger_{1,+,\downarrow} c^\dagger_{2,-,\uparrow}}{\sqrt{2}} |0\rangle \\
|1_-2_+\rangle &= \frac{c^\dagger_{1,-,\uparrow} c^\dagger_{2,+,\downarrow} - c^\dagger_{1,-,\downarrow} c^\dagger_{2,+,\uparrow}}{\sqrt{2}} |0\rangle \\
|1_-2_-\rangle &= \frac{c^\dagger_{1,-,\uparrow} c^\dagger_{2,-,\downarrow} - c^\dagger_{1,-,\downarrow} c^\dagger_{2,-,\uparrow}}{\sqrt{2}} |0\rangle \\
|2_+2_-\rangle &= \frac{c^\dagger_{2,+,\uparrow} c^\dagger_{2,-,\downarrow} - c^\dagger_{2,+,\downarrow} c^\dagger_{2,-,\uparrow}}{\sqrt{2}} |0\rangle \\
|1_{+\mathbb{1}}\rangle &= c^\dagger_{1,+,\uparrow} c^\dagger_{1,+,\downarrow} |0\rangle \\
|1_{-\mathbb{1}}\rangle &= c^\dagger_{1,-,\uparrow} c^\dagger_{1,-,\downarrow} |0\rangle \\
|2_{+\mathbb{1}}\rangle &= c^\dagger_{2,+,\uparrow} c^\dagger_{2,+,\downarrow} |0\rangle \\
|2_{-\mathbb{1}}\rangle &= c^\dagger_{2,-,\uparrow} c^\dagger_{2,-,\downarrow} |0\rangle
\end{aligned} \tag{A.4}$$

Writing H in this basis yields:

$$H_S = \begin{pmatrix}
U+\epsilon & t_- & t_+ & t_+ & t_- & 0 & 0 & 0 & 0 & 0 \\
t_-^* & \Delta_1+\Delta_2 & 0 & 0 & 0 & t_- & \sqrt{2}t_+^* & 0 & \sqrt{2}t_+ & 0 \\
t_+^* & 0 & \Delta_1-\Delta_2 & 0 & 0 & t_+ & \sqrt{2}t_-^* & 0 & 0 & \sqrt{2}t_- \\
t_+^* & 0 & 0 & -\Delta_1+\Delta_2 & 0 & t_+ & 0 & \sqrt{2}t_-^* & \sqrt{2}t_- & 0 \\
t_-^* & 0 & 0 & 0 & -\Delta_1-\Delta_2 & t_- & 0 & \sqrt{2}t_+^* & 0 & \sqrt{2}t_+ \\
0 & t_-^* & t_+^* & t_+^* & t_-^* & U-\epsilon & 0 & 0 & 0 & 0 \\
0 & \sqrt{2}t_+ & \sqrt{2}t_- & 0 & 0 & 0 & U+\epsilon+2\Delta_1 & 0 & 0 & 0 \\
0 & 0 & 0 & \sqrt{2}t_- & \sqrt{2}t_+ & 0 & 0 & U+\epsilon-2\Delta_1 & 0 & 0 \\
0 & \sqrt{2}t_+^* & 0 & \sqrt{2}t_-^* & 0 & 0 & 0 & 0 & U-\epsilon+2\Delta_2 & 0 \\
0 & 0 & \sqrt{2}t_-^* & 0 & \sqrt{2}t_+^* & 0 & 0 & 0 & 0 & U-\epsilon-2\Delta_2
\end{pmatrix} \tag{A.5}$$

Here the minus sign due to Fermi statistics is canceled by a second minus sign arising from swapping the spins of a singlet state, making all tunneling matrix elements positive. Again performing a perturbation theory expansion produces the following Hamiltonian:

$$H_S = \begin{pmatrix}
\Delta_1+\Delta_2-\frac{2|t_-|^2+4|t_+|^2}{U} & -\frac{2t_-t_+^*}{U} & -\frac{2t_+t_-^*}{U} & -\frac{2|t_-|^2}{U} \\
-\frac{2t_+t_-^*}{U} & \Delta_1-\Delta_2-\frac{2|t_+|^2+4|t_-|^2}{U} & -\frac{2|t_+|^2}{U} & -\frac{2t_-t_+^*}{U} \\
-\frac{2t_-t_+^*}{U} & -\frac{2|t_+|^2}{U} & -\Delta_1+\Delta_2-\frac{2|t_+|^2+4|t_-|^2}{U} & -\frac{2t_+t_-^*}{U} \\
-\frac{2|t_-|^2}{U} & -\frac{2t_+t_-^*}{U} & -\frac{2t_-t_+^*}{U} & -\Delta_1-\Delta_2-\frac{2|t_-|^2+4|t_+|^2}{U}
\end{pmatrix} \tag{A.6}$$

Appendix B: Tables of Ground States for Various Plaquette Geometries

Below we give the ground state energies for many different plaquette geometries. These energies are found via exact diagonalization of the Hamiltonian under the expansion where $U \gg t$. The energies are given to order t^2/U for most plaquettes less than 10 dots, and to leading order t for greater than 10 dots. Here we define $J = 4t^2/U$. Each table corresponds to a particular dot geometry, and each row corresponds to a different number of electrons occupying the plaquette. For each possible value of the total spin, the lowest-energy state with that spin is given, with the ground state across all spin values shown in bold. Thus a bold value in the rightmost column represents ferromagnetism. We color the values in the tables which correspond to cases of Nagaoka ferromagnetism green, cases of Mielke flatband ferromagnetism purple, and other cases of flatband ferromagnetism not covered by Mielke's original theorem blue.

B.1 Geometries with Fewer Dots

3 dot ring		
	Spin	
# of el.	0, 1/2	1, 3/2
4	-t -0.5J	**-2t**
3	**-1.5J**	0
2	**-2t -2J**	-t

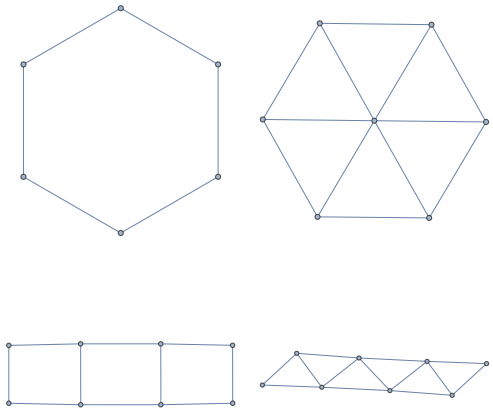

Figure B.1: Illustration of various plaquette geometries. **Top Left:** 6 dot ring. **Top Right:** 7 dots: hexagon with center. **Bottom Left:** 8 dots: 2x4 array. **Bottom Right:** 8 dot zigzag.

4 dot ring			
	Spin		
# of el.	0, 1/2	1, 3/2	2
4	**-3J**	-2J	0
3, 5	-1.732t -1.25J	**-2t**	
2, 6	**-2.828t -J**	-2t	

5 dot ring			
	Spin		
# of el.	0, 1/2	1, 3/2	2, 5/2
8	-2.618t -0.362J	**-3.236t**	
7	**-3.165t -1.047J**	-2.618t	
6	**-2t -3J**	-1.902t -0.952J	-2t
5	**-3.118J**	-1.809J	0
4	-2t -J	**-2t -2J**	-1.618t
3	-2.956t -0.937J	**-3.236t**	
2	**-3.236t -0.553J**	-2.618t	

6 dot ring				
	Spin			
# of el.	0, 1/2	1, 3/2	2, 5/2	3
6	**-4.303J**	-3.618J	-2J	0
5, 7	**-2t -2J**	-1.956t -0.679J	-2t	
4, 8	-3.464t -0.833J	**-3.464t -1.667J**	-3t	
3, 9	-3.759t -0.672J	**-4t**		
2, 10	**-3.464t -0.333J**	-3t		

7 dot ring				
	Spin			
# of el.	0, 1/2	1, 3/2	2, 5/2	3, 7/2
12	-3.247t -0.175J	**-3.604t**		
11	**-4.444t -0.513J**	-4.049t		
10	**-4.494t -1.952J**	-4.381t -0.625J	-4.494t	
9	-3.589t -0.783J	**-3.589t -1.607J**	-3.247t	
8	-2t -3J	**-2t -3.618J**	-1.978t -0.496J	-2t
7	**-4.605J**	-3.556J	-1.901J	0
6	**-2t -4.303J**	-2t -J	-2t -2J	-1.802t
5	**-3.604t -1.785J**	-3.546t -0.605J	-3.604t	
4	-4.494t -0.651J	**-4.494t -1.301J**	-4.049t	
3	-4.294t -0.482J	**-4.494t**		
2	**-3.604t -0.215J**	-3.247t		

8 dot ring					
	Spin				
# of el.	0, 1/2	1, 3/2	2, 5/2	3, 7/2	4
8	**-5.651J**	-5.128J	-3.802J	-2J	0
7, 9	-2t -2.5J	**-2t -3J**	-1.987t -0.375J	-2t	
6, 10	**-3.696t -3.988J**	-3.696t -0.927J	-3.696t -1.854J	-3.414t	
5, 11	**-4.828t -1.5J**	-4.769t -0.509J	-4.828t		
4, 12	-5.226t -0.5J	**-5.226t -J**	-4.828t		
3, 13	-4.664t -0.351J	**-4.828t**			
2, 14	**-3.696t -0.146J**	-3.414t			

9 dot ring					
	Spin				
# of el.	0, 1/2	1, 3/2	2, 5/2	3, 7/2	4, 9/2
16	-3.532t -0.092J	**-3.759t**			
15	**-5.03t -0.272J**	-4.759t			
14	**-5.759t -1.156J**	-5.671t -0.375J	-5.759t		
13	-5.745t -0.54J	**-5.745t -1.108J**	-5.411t		
12	-5.064t -2.449J	**-5.064t -2.954J**	-5.03t -0.405J	-5.064t	
11	**-3.754t -3.332J**	-3.754t -2.245J	-3.754t -1.8J	-3.532t	
10	**-2t -5.651J**	-2t -3J	-2t -3.802J	-1.992t -0.292J	-2t
9	**-6.047J**	-5.186J	-3.735J	-1.94J	0
8	-2t -4.7J	**-2t -5.128J**	-2t -2J	-2t -2J	-1.879t
7	-3.759t -2.37J	**-3.759t -2.844J**	-3.74t -0.355J	-3.759t	
6	**-5.064t -3.513J**	-5.064t -0.816J	-5.064t -1.633J	-4.759t	
5	**-5.759t -1.229J**	-5.703t -0.418J	-5.759t		
4	-5.759t -0.385J	**-5.759t -0.771J**	-5.411t		
3	-4.928t -0.261J	**-5.064t**			
2	**-3.759t -0.104J**	-3.532t			

10 dot ring						
	Spin					
# of el.	0, 1/2	1, 3/2	2, 5/2	3, 7/2	4, 9/2	5
10	**-7.015J**	-6.592J	-5.476J	-3.879J	-2J	0
9, 11	**-2t -4.732J**	-2t -4.127J	-2t -3.414J	-1.995t -0.234J	-2t	
8, 12	-3.804t -4.52J	**-3.804t -4.933J**	-3.804t -1.924J	-3.804t -1.924J	-3.618t	
7, 13	-5.236t -2.155J	**-5.236t -2.585J**	-5.215t -0.323J	-5.236t		
6, 14	**-6.155t -3.012J**	-6.155t -0.7J	-6.155t -1.4J	-5.854t		
5, 15	**-6.472t -J**	-6.421t -0.341J	-6.472t			
4, 16	-6.155t -0.3J	**-6.155t -0.6J**	-5.854t			
3, 17	-5.122t -0.199J	**-5.236t**				
2, 18	**-3.804t -0.076J**	-3.618t				

6 dots: pentagon with center				
	Spin			
# of el.	0, 1/2	1, 3/2	2, 5/2	3
10	-2.724t -0.215J	**-3.236t**		
9	-4.029t -0.532J	**-4.686t**		
8	-3.953t -1.311J	**-4.426t -1.115J**	-4.068t	
7	-3.044t -1.993J	-3.217t -1.226J	**-3.449t**	
6	**-5.118J**	-4.309J	-3J	0
5	**-2.794t -4.9J**	-2.502t -3.563J	-1.618t	
4	-4.176t -4.339J	**-4.653t -3.954J**	-3.236t	
3	**-5.17t -2.91J**	-4.686t		
2	**-5.464t -2.183J**	-4.068t		

7 dots: hexagon with center				
	Spin			
# of el.	0, 1/2	1, 3/2	2, 5/2	3, 7/2
12	-3.476t -0.33J	**-3.646t**		
11	**-4.926t -0.45J**	-4.646t		
10	-4.903t -1.155J	-5.233t -0.733J	**-5.646t**	
9	-4.722t -1.05J	**-4.941t -1.725J**	-4.646t	
8	-3.369t -2.419J	-3.391t -1.992J	-3.5t -1.128J	**-3.646t**
7	**-6.118J**	-5J	-3.5J	0
6	**-3.058t -6.477J**	-2.968t -5.865J	-2.778t -4.087J	-2t
5	**-4.817t -5.26J**	-4.503t -4.005J	-3.646t	
4	-5.662t -4.207J	**-6.151t -3.93J**	-4.646t	
3	**-6.151t -2.823J**	-5.646t		
2	**-5.912t -2.162J**	-4.646t		

8 dots: septagon with center					
	Spin				
# of el.	0, 1/2	1, 3/2	2, 5/2	3, 7/2	4
14	-3.289t -0.285J	**-3.63t**			
13	-4.919t -0.286J	**-5.432t**			
12	-5.732t -0.904J	**-6.108t -0.619J**	-5.877t		
11	-5.983t -2.072J	-6.041t -0.716J	**-6.322t**		
10	-4.925t -3.51J	-5.06t -1.058J	**-5.256t -1.705J**	-5.075t	
9	-3.626t -2.515J	-3.658t -1.953J	-3.731t -1.073J	**-3.828t**	
8	**-7.105J**	-6.556J	-5.401J	-4J	0
7	**-3.171t -7.169J**	-3.049t -6.076J	-2.745t -4.103J	-1.828t	
6	**-5.157t -6.773J**	-4.932t -5.191J	-4.971t -4.583J	-3.63t	
5	**-6.475t -5.236J**	-6.173t -4.11J	-5.432t		
4	-6.845t -4.028J	**-7.288t -3.764J**	-5.877t		
3	**-6.889t -2.799J**	-6.322t			
2	**-6.28t -2.242J**	-5.075t			

6 dots: 2x3 array				
	Spin			
# of el.	0, 1/2	1, 3/2	2, 5/2	3
6	**-4.879J**	-4.06J	-2.5J	0
5, 7	-2.31t -1.258J	-2.363t -0.627J	**-2.414t**	
4, 8	-3.647t -2.082J	**-3.666t -1.709J**	-3.414t	
3, 9	**-4.257t -1.367J**	-3.828t		
2, 10	**-3.925t -0.841J**	-3.414t		

8 dots: 2x4 array					
	Spin				
# of el.	0, 1/2	1, 3/2	2, 5/2	3, 7/2	4
8	**-6.793J**	-6.023J	-4.707J	-2.707J	0
7, 9	-2.54t -1.346J	-2.574t -0.806J	-2.597t -0.377J	**-2.618t**	
6, 10	**-4.347t -1.371J**	-4.338t -1.323J	-4.317t -1.223J	-4.236t	
5, 11	-5.265t -2.671J	**-5.29t -1.724J**	-4.854t		
4, 12	**-5.993t -2.167J**	-5.507t -1.421J	-5.236t		
3, 13	**-5.542t -1.271J**	-4.854t			
2, 14	**-4.546t -0.626J**	-4.236t			

9 dots: 3x3 array					
	Spin				
# of el.	0, 1/2	1, 3/2	2, 5/2	3, 7/2	4, 9/2
9	**-7.749J**	-6.759J	-5.108J	-3J	0
8, 10	-2.687t -1.721J	-2.703t -1.498J	-2.748t -1.024J	-2.787t -0.584J	**-2.828t**
7, 11	-4.469t -1.964J	-4.493t -1.502J	**-4.527t -2.302J**	-4.243t	
6, 12	**-5.919t -3.6J**	-5.804t -2.787J	-5.706t -1.971J	-5.657t	
5, 13	**-6.491t -2.585J**	-6.391t -1.838J	-5.657t		
4, 14	-6.307t -1.895J	**-6.664t -1.718J**	-5.657t		
3, 15	**-5.888t -1.095J**	-5.657t			
2, 16	**-4.939t -0.75J**	-4.243t			

4 dot zigzag			
	Spin		
# of el.	0, 1/2	1, 3/2	2
6	-2.372t -0.423J	**-2.562t**	
5	-2.303t -0.973J	**-2.562t**	
4	**-3J**	-2J	0
3	**-2.303t -2.721J**	-1.562t	
2	**-3.372t -2.077J**	-2.562t	

5 dot zigzag			
	Spin		
# of el.	0, 1/2	1, 3/2	2, 5/2
8	-2.669t -0.296J	**-3.091t**	
7	-3.45t -0.652J	**-3.553t**	
6	-2.588t -1.865J	-2.804t -0.893J	**-2.935t**
5	**-3.707J**	-2.5J	0
4	**-2.588t -3.857J**	-2.476t -3.2J	-1.618t
3	**-3.923t -2.925J**	-3.091t	
2	**-4.311t -2.016J**	-3.553t	

6 dot zigzag				
	Spin			
# of el.	0, 1/2	1, 3/2	2, 5/2	3
10	-3.127t -0.253J	**-3.39t**		
9	**-4.013t -0.664J**	-3.984t		
8	-4.26t -1.087J	-4.333t -0.606J	**-4.429t**	
7	-2.994t -1.561J	-3.106t -0.698J	**-3.182t**	
6	**-4.959J**	-4.255J	-2.671J	0
5	**-2.719t -4.475J**	-2.588t -3.455J	-1.802t	
4	**-4.562t -4.509J**	-4.11t -3.13J	-3.39t	
3	**-5.219t -3.073J**	-3.984t		
2	**-5.013t -1.774J**	-4.429t		

7 dot zigzag				
	Spin			
# of el.	0, 1/2	1, 3/2	2, 5/2	3, 7/2
12	-3.275t -0.216J	**-3.609t**		
11	-4.557t -0.483J	**-4.609t**		
10	-4.996t -0.835J	-5.028t -0.493J	**-5.086t**	
9	-4.926t -0.99J	-5.008t -0.497J	**-5.086t**	
8	-3.143t -2.011J	-3.24t -1.227J	-3.306t -0.567J	**-3.354t**
7	**-5.621J**	-4.657J	-2.757J	0
6	**-2.842t -5.551J**	-2.797t -4.921J	-2.665t -3.635J	-1.877t
5	**-4.852t -5.348J**	-4.311t -3.101J	-3.609t	
4	**-6.135t -4.812J**	-5.573t -3.446J	-4.609t	
3	**-6.262t -2.971J**	-5.086t		
2	**-5.539t -1.514J**	-5.086t		

8 dot zigzag					
	Spin				
# of el.	0, 1/2	1, 3/2	2, 5/2	3, 7/2	4
14	-3.509t -0.179J	**-3.786t**			
13	**-4.827t -0.49J**	-4.786t			
12	-5.74t -0.776J	-5.747t -0.453J	**-5.786t**		
11	-5.931t -0.693J	-5.989t -0.34J	**-6.04t**		
10	-5.407t -1.359J	-5.471t -0.872J	-5.534t -0.419J	**-5.592t**	
9	-3.346t -1.574J	-3.403t -0.991J	-3.445t -0.469J	**-3.477t**	
8	**-6.932J**	-6.223J	-5.039J	-2.866J	0
7	**-2.907t -6.155J**	-2.849t -5.237J	-2.716t -3.732J	-1.925t	
6	**-5.164t -6.539J**	-5.028t -5.959J	-4.463t -3.375J	-3.786t	
5	**-6.586t -5.739J**	-5.895t -3.582J	-4.786t		
4	**-7.418t -4.845J**	-6.841t -3.46J	-5.786t		
3	**-7.096t -2.785J**	-6.04t			
2	**-5.944t -1.269J**	-5.592t			

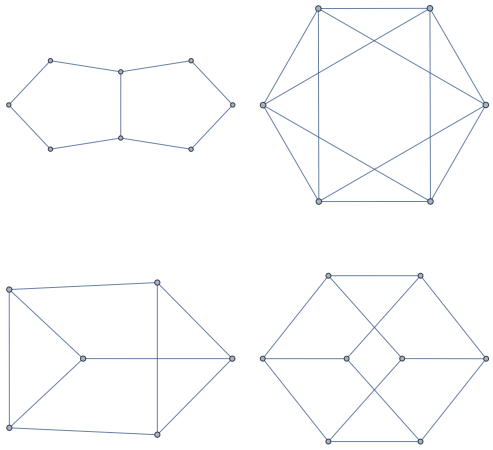

Figure B.2: Illustration of various plaquette geometries. **Top Left:** 8 dots: 2 adjacent pentagons. **Top Right:** 6 dots: octahedron. **Bottom Left:** 6 dots: triangular prism. **Bottom Right:** 8 dots: cube.

8 dots: 2 adjacent pentagons					
	Spin				
# of el.	0, 1/2	1, 3/2	2, 5/2	3, 7/2	4
14	-3.499t -0.14J	**-3.814t**			
13	-5.063t -0.261J	**-5.228t**			
12	**-5.612t -1.089J**	-5.547t -1.025J	-5.228t		
11	**-5.153t -1.969J**	-5.066t -1.366J	-4.757t		
10	**-4.023t -4.398J**	-3.945t -2.85J	-3.878t -1.57J	-3.757t	
9	-2.299t -4.87J	-2.329t -2.826J	-2.327t -0.373J	**-2.343t**	
8	**-5.798J**	-5.34J	-3.941J	-2.366J	0
7	-2.325t -2.913J	**-2.328t -3.858J**	-2.267t -2.265J	-2t	
6	**-4.033t -1.829J**	-4.024t -1.941J	-4.006t -2.065J	-3.814t	
5	-5.095t -0.999J	-5.16t -0.445J	**-5.228t**		
4	-5.418t -1.327J	**-5.436t -1.014J**	-5.228t		
3	**-5.102t -0.76J**	-4.757t			
2	**-4.093t -0.455J**	-3.757t			

6 dots: octahedron				
	Spin			
# of el.	0, 1/2	1, 3/2	2, 5/2	3
10	-3.236t -0.724J	**-4t**		
9	**-4.509t -1.088J**	-4t		
8	**-5.123t -1.894J**	-4.503t -1.102J	-4t	
7	-3t -2.55J	-3.449t -1.638J	**-4t**	
6	**-6J**	-5J	-3J	0
5	**-3t -5.75J**	-3t -4.25J	-2t	
4	-4.275t -4.947J	**-4.302t -3.867J**	-4t	
3	**-5.413t -3.573J**	-4t		
2	**-6.472t -2.894J**	-4t		

6 dots: triangular prism				
	Spin			
# of el.	0, 1/2	1, 3/2	2, 5/2	3
10	-3.323t -0.556J	**-4t**		
9	**-4.39t -1.305J**	-4t		
8	**-4.614t -2.138J**	-4.459t -1.207J	-4t	
7	-2.562t -1.852J	-2.791t -1.173J	**-3t**	
6	**-5.303J**	-4.281J	-2.5J	0
5	**-2.732t -3.684J**	-2.618t -3.171J	-2t	
4	**-4.152t -4.126J**	-4.07t -2.284J	-4t	
3	**-4.766t -2.509J**	-4t		
2	**-4.962t -1.306J**	-4t		

8 dots: cube					
	Spin				
# of el.	0, 1/2	1, 3/2	2, 5/2	3, 7/2	4
8	**-7.82J**	-7J	-5.414J	-3J	0
7, 9	-2.625t -3.573J	-2.714t -1.636J	-2.858t -1.124J	**-3t**	
6, 10	**-4.788t -1.811J**	-4.673t -2.032J	-4.51t -1.092J	-4t	
5, 11	-5.546t -3.056J	**-5.984t -2.47J**	-5t		
4, 12	-5.962t -2.157J	-5.951t -1.717J	**-6t**		
3, 13	**-5.658t -1.329J**	-5t			
2, 14	**-5.292t -0.857J**	-4t			

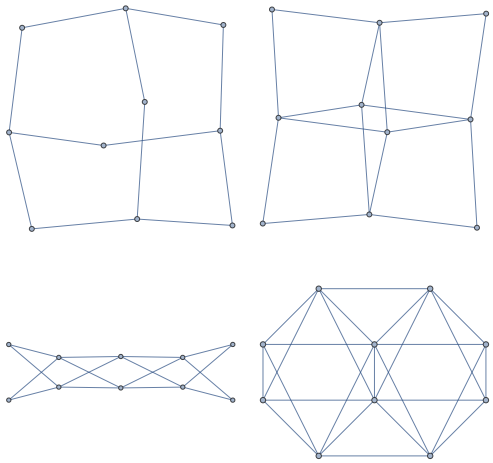

Figure B.3: Illustration of various plaquette geometries. **Top Left:** 10 dot diamond lattice. **Top Right:** 10 dot bcc lattice. **Bottom Left:** 10 dot bcc: 2x5 criss cross. **Bottom Right:** 10 dot fcc lattice.

10 dots: 3 adjacent pentagons						
	Spin					
# of el.	0, 1/2	1, 3/2	2, 5/2	3, 7/2	4, 9/2	5
18	-3.756t -0.071J	**-3.966t**				
17	-5.548t -0.198J	**-5.845t**				
16	-6.511t -0.694J	-6.741t -0.488J	**-6.845t**			
15	**-7.171t -1.351J**	-7.117t -1.248J	-6.498t			
14	**-6.816t -3.309J**	-6.783t -2.695J	-6.457t -1.387J	-6.15t		
13	**-5.888t -4.544J**	-5.746t -2.606J	-5.733t -1.609J	-5.578t		
12	**-4.429t -6.17J**	-4.352t -4.664J	-4.318t -3.134J	-4.268t -1.723J	-4.046t	
11	-2.466t -3.621J	-2.472t -3.203J	-2.488t -2.048J	-2.496t -0.432J	**-2.514t**	
10	**-7.404J**	-7.034J	-6.264J	-4.353J	-2.5J	0
9	-2.48t -4.452J	**-2.481t -5.462J**	-2.451t -4.053J	-2.342t -2.299J	-2.086t	
8	**-4.424t -3.277J**	-4.421t -3.056J	-4.41t -2.823J	-4.396t -2.416J	-3.966t	
7	-5.798t -1.422J	-5.827t -1.247J	-5.841t -0.881J	**-5.845t**		
6	-6.63t -2.368J	-6.657t -1.445J	-6.762t -0.538J	**-6.845t**		
5	**-6.984t -1.645J**	-6.861t -0.699J	-6.498t			
4	-6.434t -1.157J	**-6.72t -1.053J**	-6.15t			
3	**-5.698t -0.637J**	-5.578t				
2	**-4.535t -0.403J**	-4.046t				

10 dot diamond lattice						
	Spin					
# of el.	0, 1/2	1, 3/2	2, 5/2	3, 7/2	4, 9/2	5
10	-6.883J	**-7.726J**	-6.59J	-4.732J	-2.5J	0
9, 11	-2.396t -4.353J	-2.403t -4.307J	-2.414t -1.898J	-2.417t -0.614J	**-2.449t**	
8, 12	**-4.388t -5.578J**	-4.375t -4.304J	-4.317t -2.458J	-4.237t -1.827J	-3.864t	
7, 13	**-5.97t -3.057J**	-5.921t -2.891J	-5.812t -2.248J	-5.278t		
6, 14	**-6.74t -1.307J**	-6.684t -1.32J	-6.653t -0.781J	-6.692t		
5, 15	-6.724t -1.472J	**-6.941t -1.672J**	-6.692t			
4, 16	-6.29t -0.745J	-6.573t -0.605J	**-6.692t**			
3, 17	**-5.594t -0.448J**	-5.278t				
2, 18	**-4.52t -0.294J**	-3.864t				

10 dots: 2 adjacent hexagons						
	Spin					
# of el.	0, 1/2	1, 3/2	2, 5/2	3, 7/2	4, 9/2	5
10	**-7.52J**	-7.017J	-5.967J	-4.305J	-2.43J	0
9, 11	-2.293t -4.268J	-2.293t -1.995J	-2.298t -1.894J	-2.297t -0.241J	**-2.303t**	
8, 12	**-4.093t -4.875J**	-4.082t -4.067J	-4.043t -3.057J	-4.016t -2.006J	-3.921t	
7, 13	-5.579t -2.558J	**-5.585t -3.33J**	-5.487t -1.745J	-5.224t		
6, 14	**-6.513t -1.485J**	-6.504t -1.59J	-6.489t -1.714J	-6.224t		
5, 15	-6.726t -0.665J	-6.782t -0.291J	**-6.842t**			
4, 16	-6.366t -0.886J	**-6.369t -0.612J**	-6.224t			
3, 17	**-5.517t -0.471J**	-5.224t				
2, 18	**-4.16t -0.29J**	-3.921t				

10 dot bcc lattice						
	Spin					
# of el.	0, 1/2	1, 3/2	2, 5/2	3, 7/2	4, 9/2	5
10	-8.984J	**-9.799J**	-8.405J	-6.361J	-3.618J	0
9, 11	-3.196t -3.189J	-3.282t -2.256J	-3.362t -1.386J	-3.413t -0.734J	**-3.464t**	
8, 12	-5.098t -2.441J	-5.072t -2.729J	-5.123t -2.928J	**-5.125t -2.391J**	-4.878t	
7, 13	-6.49t -3.393J	-6.5t -2.79J	**-6.571t -2.417J**	-6.293t		
6, 14	**-7.618t -3.534J**	-7.463t -3.174J	-7.29t -2.366J	-6.293t		
5, 15	**-7.786t -3.072J**	-7.673t -2.348J	-6.293t			
4, 16	-7.509t -2.391J	**-7.857t -2.264J**	-6.293t			
3, 17	**-7.027t -1.654J**	-6.293t				
2, 18	**-6.08t -1.228J**	-4.878t				

10 dots: 2x5 bcc criss-cross						
	Spin					
# of el.	0, 1/2	1, 3/2	2, 5/2	3, 7/2	4, 9/2	5
10	-9.284J	**-9.83J**	-8.405J	-6.374J	-3.618J	0
9, 11	-3.268t -2.157J	-3.334t -1.582J	-3.387t -1.021J	-3.428t -0.489J	**-3.464t**	
8, 12	-5.358t -1.963J	-5.353t -1.999J	-5.34t -2.074J	-5.393t -0.404J	**-5.464t**	
7, 13	-6.216t -3.62J	**-6.389t -2.574J**	-6.247t -2.192J	-5.464t		
6, 14	**-7.441t -3.203J**	-7.247t -3.069J	-6.752t -1.888J	-5.464t		
5, 15	**-7.879t -3.096J**	-7.128t -2.129J	-5.464t			
4, 16	**-8.363t -3.072J**	-7.337t -2.036J	-5.464t			
3, 17	**-7.471t -2.032J**	-5.464t				
2, 18	**-6.098t -1.164J**	-5.464t				

10 dot fcc lattice						
	Spin					
# of el.	0, 1/2	1, 3/2	2, 5/2	3, 7/2	4, 9/2	5
18	-4.364t -0.272J	**-4.65t**				
17	-6.3t -0.43J	**-6.569t**				
16	**-7.749t -1.162J**	-7.618t -0.859J	-7.569t			
15	**-8.606t -1.68J**	-8.566t -J	-8.569t			
14	**-8.888t -2.802J**	-8.617t -2.15J	-8.853t -1.532J	-8.868t		
13	**-8.588t -3.606J**	-8.522t -2.684J	-8.46t -1.553J	-8.454t		
12	-7.066t -3.088J	-7.181t -2.453J	-7.265t -1.711J	-7.365t -0.924J	**-7.454t**	
11	-4.602t -4.002J	-4.786t -3.163J	-4.957t -2.093J	-5.094t -1.037J	**-5.218t**	
10	**-11.472J**	-10.746J	-9.267J	-7.371J	-4.281J	0
9	-3.538t -10.12J	**-3.549t -9.538J**	-3.455t -7.972J	-3.18t -5.079J	-2.414t	
8	**-6.506t -11.143J**	-6.415t -10.363J	-6.179t -8.361J	-5.933t -6.143J	-4.65t	
7	**-8.246t -9.861J**	-8.166t -8.761J	-7.732t -6.303J	-6.569t		
6	**-9.823t -9.276J**	-9.762t -8.453J	-9.25t -6.114J	-7.569t		
5	**-10.933t -7.723J**	-10.311t -5.714J	-8.569t			
4	**-11.326t -6.351J**	-10.824t -5.253J	-8.868t			
3	**-10.697t -4.257J**	-8.454t				
2	**-9.177t -2.941J**	-7.454t				

6 dots: square between triangles				
	Spin			
# of el.	0, 1/2	1, 3/2	2, 5/2	3
10	-3.115t -0.514J	**-3.414t**		
9	-3.949t -0.426J	**-4.146t**		
8	**-4.374t -1.222J**	-4.322t -1.006J	-4.146t	
7	-2.586t -1.576J	-2.666t -0.644J	**-2.732t**	
6	**-4.532J**	-4.121J	-2.5J	0
5	**-2.653t -3.883J**	-2.454t -2.063J	-2t	
4	**-4.256t -3.931J**	-3.705t -2.525J	-3.414t	
3	**-4.742t -2.329J**	-4.146t		
2	**-4.537t -0.923J**	-4.146t		

B.2 Geometries with Many Dots

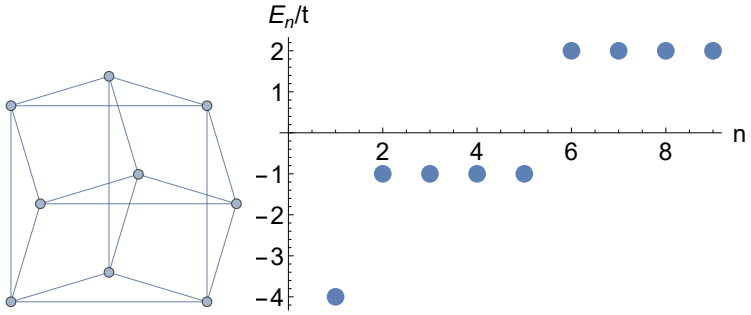

Figure B.4: Illustration of plaquette geometry (Left) and single particle energies (Right) for 9 dots: (2,3)-Hamming graph

9 dots: (2,3)-Hamming graph					
	Spin				
# of el.	0, 1/2	1, 3/2	2, 5/2	3, 7/2	4
16	**-4t**	**-4t**			
15	-5.5857t	**-6t**			
14	-7.1945t	-7.1315t	**-8t**		
13	-7.4647t	**-7.7421t**	-7t		
12	**-7.7014t**	-7.2919t	-6.8076t	-6t	
11	**-5.9511t**	-5.9366t	-5.8503t	-5t	
10	-3.1623t	-3.3456t	-3.5616t	-3.7762t	**-4t**
9	0	0	0	0	0
8	**-3.4142t**	-3.3162t	-3.1009t	-2.7321t	-2t
7	-5.5185t	**-5.534t**	-5.063t	-4t	
6	-6.7831t	-6.9136t	**-7.4357t**	-6t	
5	-7.507t	-7.9138t	**-8t**		
4	-7.5146t	**-7.8541t**	-7t		
3	**-7.4774t**	-6t			
2	**-7.1231t**	-5t			

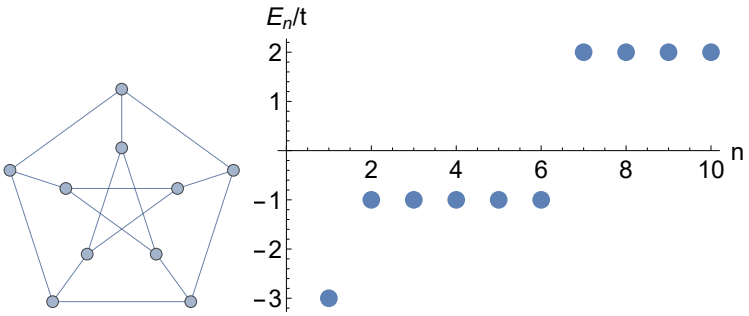

Figure B.5: Illustration of plaquette geometry (Left) and single particle energies (Right) for 10 dots: Petersen graph

10 dots: Petersen graph					
	Spin				
# of el.	0, 1/2	1, 3/2	2, 5/2	3, 7/2	4, 9/2
18	-3.9173t	**-4t**			
17	-5.7459t	**-6t**			
16	-6.8988t	-7.2802t	**-8t**		
15	-7.8383t	**-7.9503t**	-7t		
14	**-7.7187t**	-7.6523t	-6.9835t	-6t	
13	**-6.708t**	-6.2825t	-5.8116t	-5t	
12	**-5.1579t**	-4.8585t	-4.8241t	-4.5823t	-4t
11	-2.6981t	-2.7244t	-2.8192t	-2.8951t	**-3t**
10	0	0	0	0	0
9	**-2.8097t**	-2.7863t	-2.6564t	-2.4142t	-2t
8	**-4.9536t**	-4.9468t	-4.9152t	-4.5866t	-4t
7	-6.5726t	-6.5144t	**-6.8102t**	-6t	
6	-7.3782t	-7.309t	-7.614t	**-8t**	
5	-7.0921t	**-7.3878t**	-7t		
4	-6.7057t	**-6.7932t**	-6t		
3	**-6.0931t**	-5t			
2	**-5.4641t**	-4t			

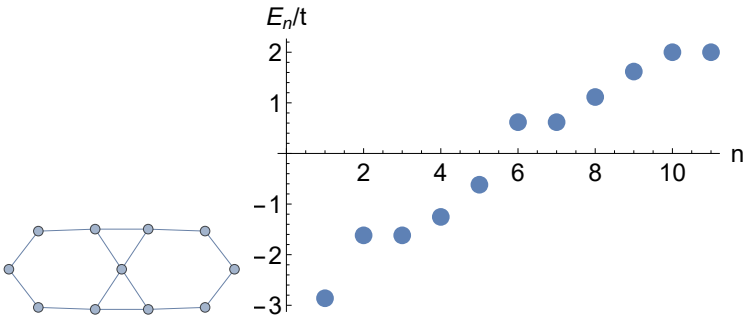

Figure B.6: Illustration of plaquette geometry (Left) and single particle energies (Right) for 11 dots: Kagome lattice

11 dots: Kagome lattice						
	Spin					
# of el.	0, 1/2	1, 3/2	2, 5/2	3, 7/2	4, 9/2	5
20	-3.9028t	**-4t**				
19	-5.5437t	**-5.618t**				
18	**-6.8951t**	-6.779t	-6.7329t			
17	-7.6334t	**-7.6422t**	-7.351t			
16	-7.744t	-7.8192t	-7.8956t	**-7.969t**		
15	-7.304t	-7.3657t	**-7.367t**	-7.351t		
14	-6.3466t	-6.35t	**-6.3582t**	-6.1877t	-6.0969t	
13	-4.7628t	-4.7668t	**-4.771t**	-4.7107t	-4.4788t	
12	-2.8445t	-2.8493t	-2.8493t	-2.8548t	-2.8564t	**-2.8608t**
11	0	0	0	0	0	0
10	**-2.8375t**	**-2.8375t**	-2.8373t	-2.8371t	-2.578t	-2t
9	**-4.7518t**	-4.7107t	-4.6642t	-4.5937t	-4t	
8	**-6.3655t**	-6.3373t	-6.1913t	-6.1535t	-5.618t	
7	-7.4895t	**-7.5335t**	-7.1921t	-6.7329t		
6	**-8.2293t**	-8.213t	-8.172t	-7.351t		
5	-7.9642t	**-8.0416t**	-7.969t			
4	-7.4423t	**-7.4568t**	-7.351t			
3	**-6.4196t**	-6.0969t				
2	**-4.9689t**	-4.4788t				

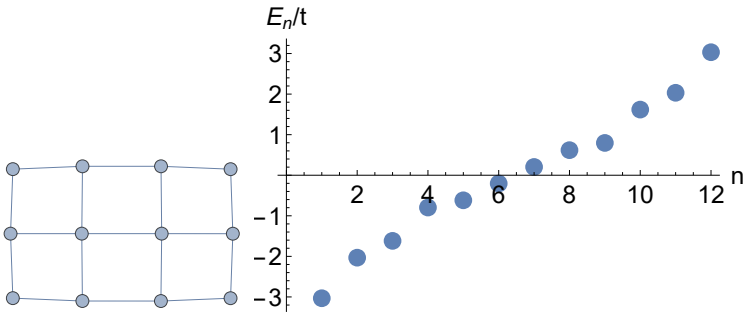

Figure B.7: Illustration of plaquette geometry (Left) and single particle energies (Right) for 12 dots: 3x4 square lattice

12 dots: 3x4 square lattice						
	Spin					
# of el.	0, 1/2	1, 3/2	2, 5/2	3, 7/2	4, 9/2	5, 11/2
11, 13	-2.9176t	-2.9489t	-2.9751t	-2.9961t	-3.0149t	**-3.0322t**
10, 14	**-5.1784t**	-5.1749t	-5.1673t	-5.1545t	-5.1328t	-5.0645t
9, 15	-6.7036t	**-6.7102t**	-6.6797t	-6.6691t	-6.6825t	
8, 16	-7.9639t	**-8.0024t**	-7.8733t	-7.7534t	-7.4787t	
7, 17	-8.753t	**-8.7704t**	-8.4928t	-8.0967t		
6, 18	**-9.249t**	-9.1326t	-8.9408t	-8.3006t		
5, 19	**-9.0554t**	-8.6366t	-8.0967t			
4, 20	**-8.2599t**	-8.2524t	-7.4787t			
3, 21	**-7.0889t**	-6.6825t				
2, 22	**-5.5t**	-5.0645t				

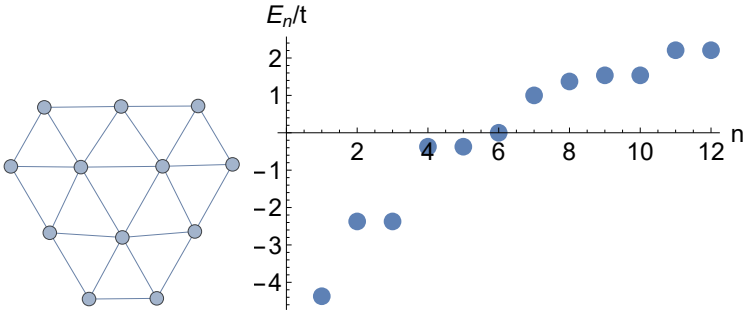

Figure B.8: Illustration of plaquette geometry (Left) and single particle energies (Right) for 12 dots: triangle lattice

12 dots: triangle lattice						
	Spin					
# of el.	0, 1/2	1, 3/2	2, 5/2	3, 7/2	4, 9/2	5, 11/2
22	-4.0901t	**-4.416t**				
21	**-6.0743t**	-5.9525t				
20	**-7.7223t**	-7.4786t	-7.489t			
19	-8.664t	-8.7639t	**-8.8613t**			
18	-9.0987t	-9.3905t	-9.6533t	**-9.8613t**		
17	-9.5499t	-9.7413t	-9.8213t	**-9.8613t**		
16	-9.6144t	-9.6149t	**-9.6259t**	-9.6043t	-9.4885t	
15	-8.6899t	-8.771t	-8.8835t	-9.0017t	**-9.1156t**	
14	**-6.9326t**	-6.9212t	-6.9081t	-6.8908t	-6.8406t	-6.744t
13	-4.1043t	-4.1644t	-4.2238t	-4.2725t	-4.3234t	**-4.3723t**
12	0	0	0	0	0	0
11	**-3.4469t**	-3.4049t	-3.3249t	-3.2117t	-3.0355t	-2.208t
10	**-6.1048t**	-6.0723t	-6.013t	-5.6787t	-5.1205t	-4.416t
9	**-8.3091t**	-8.2684t	-7.8417t	-7.1366t	-5.9525t	
8	-9.8348t	**-9.999t**	-9.502t	-9.0703t	-7.489t	
7	**-11.1618t**	-10.7841t	-10.3275t	-8.8613t		
6	**-12.1777t**	-11.3801t	-10.9679t	-9.8613t		
5	**-11.8013t**	-11.0846t	-9.8613t			
4	-10.7776t	**-11.141t**	-9.4885t			
3	**-9.5882t**	-9.1156t				
2	**-7.8072t**	-6.744t				

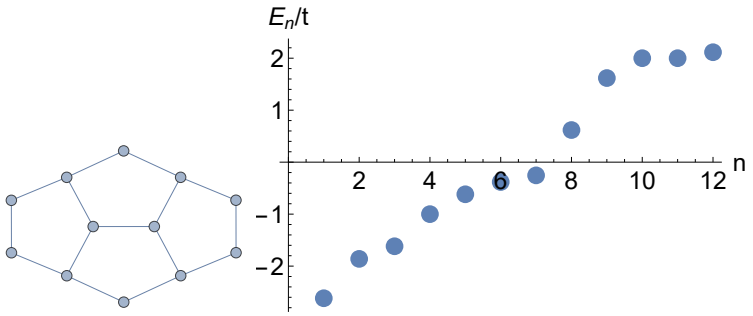

Figure B.9: Illustration of plaquette geometry (Left) and single particle energies (Right) for 12 dots: 4 adjacent pentagons

12 dots: 4 adjacent pentagons						
	Spin					
# of el.	0, 1/2	1, 3/2	2, 5/2	3, 7/2	4, 9/2	5, 11/2
22	-3.9693t	**-4.1149t**				
21	-5.9239t	**-6.1149t**				
20	-7.4645t	-7.594t	**-7.7329t**			
19	-8.3466t	**-8.362t**	-8.351t			
18	**-8.7285t**	-8.7119t	-8.6377t	-8.0969t		
17	**-8.4649t**	-8.4168t	-8.0788t	-7.7149t		
16	**-7.7016t**	-7.6604t	-7.5074t	-7.2633t	-7.0969t	
15	**-6.4056t**	-6.2942t	-6.2205t	-6.2093t	-6.0969t	
14	**-4.6774t**	-4.6668t	-4.629t	-4.6165t	-4.6019t	-4.4788t
13	-2.5629t	-2.5744t	-2.5851t	-2.5981t	-2.6078t	**-2.618t**
12	0	0	0	0	0	0
11	**-2.5706t**	-2.5699t	-2.5571t	-2.5202t	-2.3996t	-2.1149t
10	**-4.7029t**	-4.6957t	-4.6949t	-4.6881t	-4.5666t	-4.1149t
9	-6.3047t	-6.3257t	-6.3346t	**-6.341t**	-6.1149t	
8	-7.5825t	-7.619t	-7.6594t	-7.6986t	**-7.7329t**	
7	-8.2239t	-8.2711t	-8.3296t	**-8.351t**		
6	**-8.5705t**	-8.502t	-8.4079t	-8.0969t		
5	**-8.3087t**	-8.2013t	-7.7149t			
4	-7.5317t	**-7.5333t**	-7.0969t			
3	**-6.3387t**	-6.0969t				
2	**-4.8299t**	-4.4788t				

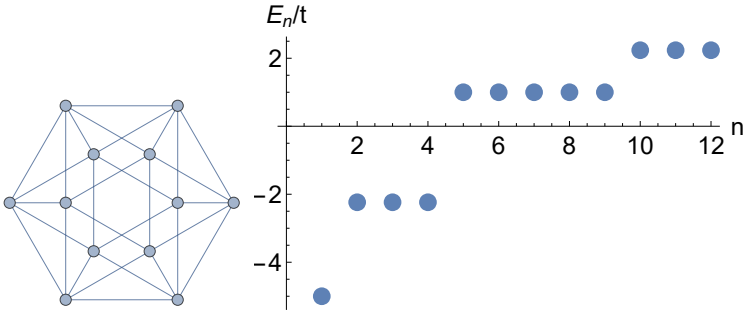

Figure B.10: Illustration of plaquette geometry (Left) and single particle energies (Right) for 12 dots: icosahedron

12 dots: icosahedron						
	Spin					
# of el.	0, 1/2	1, 3/2	2, 5/2	3, 7/2	4, 9/2	5, 11/2
22	-4.0943t	**-4.4721t**				
21	-6.145t	**-6.7082t**				
20	-7.6862t	**-8.0527t**	-7.7082t			
19	**-9.4379t**	-9.0898t	-8.7082t			
18	**-10.8708t**	-10.4651t	-10.08t	-9.7082t		
17	-10.5737t	-10.7619t	**-10.8116t**	-10.7082t		
16	-10.1516t	-10.3966t	-10.7331t	-11.2211t	**-11.7082t**	
15	-9.4187t	-9.5558t	-9.628t	**-9.7674t**	-9.4721t	
14	**-7.991t**	-7.9108t	-7.8183t	-7.76t	-7.4707t	-7.2361t
13	-4.2367t	-4.3665t	-4.5315t	-4.6867t	-4.8473t	**-5t**
12	0	0	0	0	0	0
11	**-3.4806t**	-3.4472t	-3.3804t	-3.2519t	-2.913t	-2.2361t
10	-6.3265t	**-6.3291t**	-6.1957t	-5.9724t	-5.7174t	-4.4721t
9	**-9.1212t**	-8.7907t	-8.13t	-7.3353t	-6.7082t	
8	**-11.8779t**	-11.0131t	-10.0811t	-8.9171t	-7.7082t	
7	**-12.7168t**	-11.6355t	-10.4343t	-8.7082t		
6	-12.7096t	**-13.1905t**	-11.9313t	-9.7082t		
5	-12.6537t	**-13.4443t**	-10.7082t			
4	-11.6497t	**-12.1895t**	-11.7082t			
3	**-10.7494t**	-9.4721t				
2	**-9.2279t**	-7.2361t				

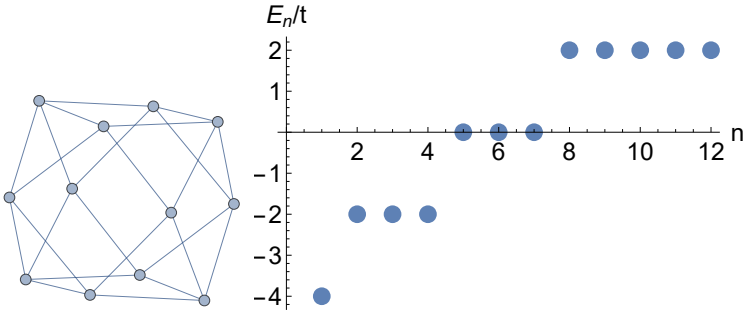

Figure B.11: Illustration of plaquette geometry (Left) and single particle energies (Right) for 12 dots: cuboctahedron

12 dots: cuboctahedron						
	Spin					
# of el.	0, 1/2	1, 3/2	2, 5/2	3, 7/2	4, 9/2	5, 11/2
22	**-4t**	**-4t**				
21	-5.9153t	**-6t**				
20	-7.7375t	-7.7468t	**-8t**			
19	-9.2002t	-9.451t	**-10t**			
18	**-10.3255t**	-10.1679t	-10.2674t	-10t		
17	-10.2328t	-10.3376t	**-10.3892t**	-10t		
16	-9.9934t	-9.9072t	-9.7962t	-9.7505t	**-10t**	
15	-8.3886t	**-8.471t**	-8.4547t	-8.4338t	-8t	
14	**-6.6394t**	-6.5918t	-6.534t	-6.5102t	-6.4667t	-6t
13	-3.5224t	-3.6096t	-3.7088t	-3.809t	-3.9058t	**-4t**
12	0	0	0	0	0	0
11	**-3.4943t**	-3.4683t	-3.2978t	-3.0755t	-2.7913t	-2t
10	**-6.0941t**	-6.0754t	-6.0063t	-5.5833t	-5.0187t	-4t
9	**-8.2176t**	-8.1762t	-7.9333t	-7.1942t	-6t	
8	**-10.1759t**	-9.6179t	-9.3573t	-9.3707t	-8t	
7	**-10.9403t**	-10.5902t	-10.2t	-10t		
6	-11.2782t	**-11.3335t**	-10.8622t	-10t		
5	-10.9465t	**-11.4593t**	-10t			
4	-10.0423t	**-10.2462t**	-10t			
3	**-8.8681t**	-8t				
2	**-7.4186t**	-6t				

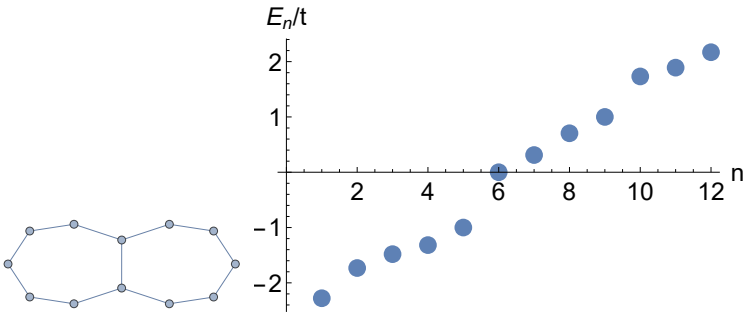

Figure B.12: Illustration of plaquette geometry (Left) and single particle energies (Right) for 12 dots: 2 adjacent septagons

12 dots: 2 adjacent septagons						
	Spin					
# of el.	0, 1/2	1, 3/2	2, 5/2	3, 7/2	4, 9/2	5, 11/2
22	-3.8071t	**-4.0613t**				
21	-5.7109t	**-5.7934t**				
20	**-7.0429t**	-7.0052t	-6.7934t			
19	**-7.7759t**	-7.7187t	-7.498t			
18	**-8.08t**	-7.9946t	-7.9265t	-7.8091t		
17	-7.7668t	**-7.8153t**	-7.784t	-7.8091t		
16	**-7.0321t**	-7.0292t	-7.0233t	-7.011t	-6.8091t	
15	-5.7855t	**-5.7861t**	-5.7824t	-5.7179t	-5.4917t	
14	**-4.1526t**	-4.1505t	-4.1477t	-4.1084t	-4.0779t	-4.0105t
13	-2.2727t	-2.2741t	-2.2743t	-2.2762t	-2.2758t	**-2.2784t**
12	0	0	0	0	0	0
11	-2.2735t	-2.2742t	-2.2749t	**-2.2756t**	-2.2501t	-2.1701t
10	**-4.1584t**	-4.1573t	-4.155t	-4.151t	-4.1417t	-4.0613t
9	-5.7881t	-5.7865t	-5.793t	-5.7823t	**-5.7934t**	
8	**-7.0028t**	-6.9923t	-6.9406t	-6.9139t	-6.7934t	
7	-7.8016t	**-7.8069t**	-7.7162t	-7.498t		
6	**-8.0829t**	-8.0746t	-8.0609t	-7.8091t		
5	-7.7148t	-7.7608t	**-7.8091t**			
4	**-6.9162t**	-6.9077t	-6.8091t			
3	**-5.7455t**	-5.4917t				
2	**-4.1909t**	-4.0105t				

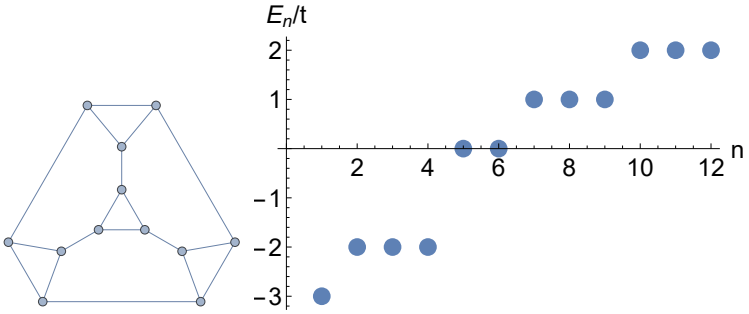

Figure B.13: Illustration of plaquette geometry (Left) and single particle energies (Right) for 12 dots: truncated tetrahedron

12 dots: truncated tetrahedron						
	Spin					
# of el.	0, 1/2	1, 3/2	2, 5/2	3, 7/2	4, 9/2	5, 11/2
22	-3.8548t	**-4t**				
21	-5.6857t	**-6t**				
20	-7.153t	**-7.2512t**	-7t			
19	**-8.3469t**	-8.2954t	-8t			
18	-8.7881t	-8.7349t	-8.8291t	**-9t**		
17	-8.8369t	-8.9243t	-8.9382t	**-9t**		
16	-8.8694t	-8.8901t	-8.9231t	-8.9577t	**-9t**	
15	**-7.4721t**	-7.449t	-7.4153t	-7.3155t	-7t	
14	**-5.4205t**	-5.4078t	-5.4017t	-5.3955t	-5.357t	-5t
13	-2.8938t	-2.9119t	-2.933t	-2.957t	-2.9703t	**-3t**
12	0	0	0	0	0	0
11	**-2.8371t**	-2.8342t	-2.786t	-2.6996t	-2.5529t	-2t
10	**-5.3058t**	-5.2842t	-5.0965t	-4.9502t	-4.5529t	-4t
9	**-7.4439t**	-7.1779t	-6.6392t	-6.2305t	-6t	
8	**-9.1522t**	-8.5611t	-8.147t	-7.5606t	-7t	
7	**-9.6447t**	-9.2777t	-8.9411t	-8t		
6	-9.6705t	**-9.8117t**	-9.3906t	-9t		
5	-9.3822t	**-9.7702t**	-9t			
4	-8.8079t	-8.9459t	**-9t**			
3	**-7.339t**	-7t				
2	**-5.6519t**	-5t				

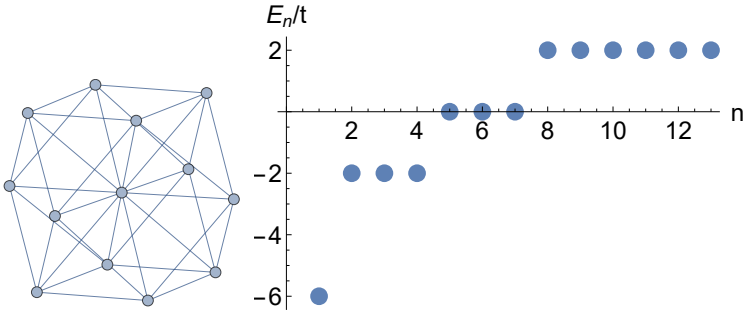

Figure B.14: Illustration of plaquette geometry (Left) and single particle energies (Right) for 13 dots: FCC lattice (cuboctahedron with center)

13 dots: FCC lattice (cuboctahedron with center)							
	Spin						
# of el.	0, 1/2	1, 3/2	2, 5/2	3, 7/2	4, 9/2	5, 11/2	6
24	**-4t**	**-4t**					
23	**-6t**	**-6t**					
22	-7.7403t	-7.871t	**-8t**				
21	-9.5552t	-9.6625t	**-10t**				
20	-10.8105t	-11.0213t	-11.3645t	**-12t**			
19	-12.0246t	-11.988t	**-12.1859t**	-12t			
18	-11.7258t	-11.9205t	-12.1634t	**-12.2829t**	-12t		
17	-11.5713t	-11.5946t	-11.6016t	-11.6503t	**-12t**		
16	-9.7317t	-9.9794t	-10.1818t	-10.2407t	**-10.3303t**	-10t	
15	-8.0492t	-8.135t	-8.2188t	-8.3152t	**-8.3707t**	-8t	
14	-5.3755t	-5.3902t	-5.4543t	-5.5604t	-5.6951t	-5.8436t	**-6t**
13	0	0	0	0	0	0	0
12	**-3.7243t**	-3.7077t	-3.646t	-3.5509t	-3.3313t	-2.9438t	-2t
11	**-7.1654t**	-7.1024t	-6.7447t	-6.2969t	-5.6731t	-4t	
10	**-9.6813t**	-9.637t	-9.535t	-8.9292t	-8.1277t	-6t	
9	**-11.7707t**	-11.701t	-11.395t	-10.4625t	-8t		
8	**-13.7166t**	-13.0744t	-12.7837t	-12.8213t	-10t		
7	**-14.3472t**	-13.9839t	-13.5181t	-12t			
6	-14.546t	**-14.6431t**	-14.1514t	-12t			
5	-14.2217t	**-14.748t**	-12t				
4	-13.2602t	**-13.4679t**	-12t				
3	**-12.0947t**	-10t					
2	**-10.6671t**	-8t					

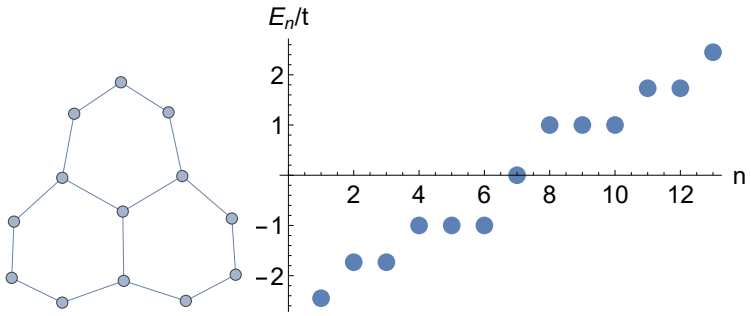

Figure B.15: Illustration of plaquette geometry (Left) and single particle energies (Right) for 13 dots: 3 adjacent hexagons

13 dots: 3 adjacent hexagons							
	Spin						
# of el.	0, 1/2	1, 3/2	2, 5/2	3, 7/2	4, 9/2	5, 11/2	6
12, 14	-2.4283t	-2.4299t	-2.4355t	-2.4364t	-2.4422t	-2.4434t	**-2.4495t**
11, 15	**-4.4122t**	-4.4067t	-4.3793t	-4.3515t	-4.33t	-4.1815t	
10, 16	**-6.1311t**	-6.1271t	-6.1235t	-6.0445t	-6.0155t	-5.9136t	
9, 17	**-7.515t**	-7.5121t	-7.4809t	-7.256t	-6.9136t		
8, 18	**-8.4948t**	-8.4917t	-8.4796t	-8.4616t	-7.9136t		
7, 19	-8.8459t	-8.8752t	-8.897t	**-8.9136t**			
6, 20	-8.7807t	-8.7935t	-8.8623t	**-8.9136t**			
5, 21	**-8.341t**	-8.2314t	-7.9136t				
4, 22	-7.2468t	**-7.4316t**	-6.9136t				
3, 23	**-6.0194t**	-5.9136t					
2, 24	**-4.5183t**	-4.1815t					

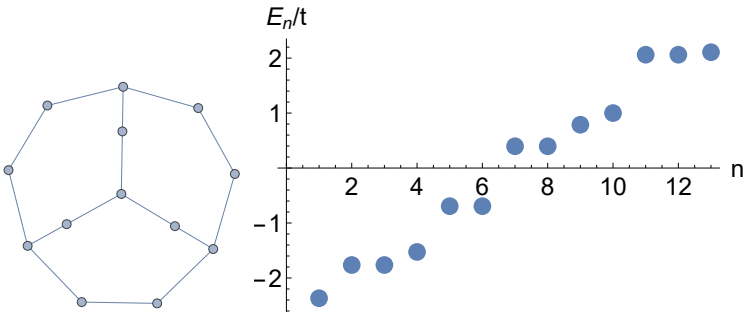

Figure B.16: Illustration of plaquette geometry (Left) and single particle energies (Right) for 13 dots: 3 septagons sharing 2 edges

13 dots: 3 septagons sharing 2 edges							
	Spin						
# of el.	0, 1/2	1, 3/2	2, 5/2	3, 7/2	4, 9/2	5, 11/2	6
24	-4.0848t	**-4.1686t**					
23	-6.0113t	**-6.2301t**					
22	-7.4479t	**-7.4657t**	-7.2301t				
21	**-8.4065t**	-8.3499t	-8.0178t				
20	**-8.9493t**	-8.8306t	-8.6t	-8.4141t			
19	**-8.8941t**	-8.8126t	-8.7883t	-8.8105t			
18	-8.335t	**-8.4004t**	-8.3907t	-8.3383t	-8.1167t		
17	-7.5004t	-7.4929t	**-7.5051t**	-7.4228t	-7.4228t		
16	-6.2019t	**-6.2079t**	-6.1976t	-6.1925t	-6.1195t	-5.8967t	
15	**-4.4245t**	-4.4211t	-4.4093t	-4.3739t	-4.3367t	-4.1327t	
14	-2.3468t	-2.3505t	-2.3516t	-2.3524t	-2.3583t	-2.3593t	**-2.3686t**
13	0	0	0	0	0	0	0
12	**-2.3519t**	-2.3512t	-2.3494t	-2.3478t	-2.3422t	-2.2755t	-2.1071t
11	**-4.4177t**	-4.4098t	-4.4029t	-4.3968t	-4.3954t	-4.1686t	
10	-6.1988t	-6.1978t	-6.1945t	-6.2079t	-6.2106t	**-6.2301t**	
9	**-7.5236t**	-7.5149t	-7.446t	-7.3828t	-7.2301t		
8	**-8.4437t**	-8.4183t	-8.3828t	-8.2726t	-8.0178t		
7	**-8.9113t**	-8.8698t	-8.8437t	-8.4141t			
6	-8.7691t	-8.7845t	-8.8059t	**-8.8105t**			
5	-8.3081t	**-8.359t**	-8.1167t				
4	-7.181t	**-7.4344t**	-7.4228t				
3	**-6.025t**	-5.8967t					
2	**-4.492t**	-4.1327t					

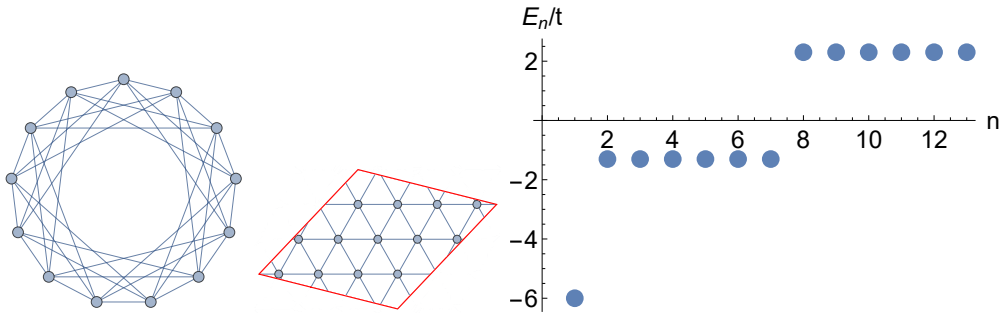

Figure B.17: Illustration of plaquette geometry (Left) and single particle energies (Right) for 13 dots: Paley-13 graph (triangle lattice with PBC)

13 dots: Paley-13 graph (triangle lattice with PBC)							
	Spin						
# of el.	0, 1/2	1, 3/2	2, 5/2	3, 7/2	4, 9/2	5, 11/2	6
24	**-4.6056t**	**-4.6056t**					
23	**-6.9083t**	**-6.9083t**					
22	-8.7177t	-8.9812t	**-9.2111t**				
21	-10.7043t	-10.9538t	**-11.5139t**				
20	-11.79t	-12.1959t	-12.7335t	**-13.8167t**			
19	-12.8266t	-12.9854t	**-13.4368t**	-12.5139t			
18	-12.6951t	-12.8908t	**-13.0302t**	-12.1777t	-11.2111t		
17	**-12.3798t**	-12.1954t	-11.618t	-10.8536t	-9.9083t		
16	-10.784t	**-10.7897t**	-10.5095t	-10.1266t	-9.4571t	-8.6056t	
15	**-8.3931t**	-8.3615t	-8.3062t	-8.2131t	-7.9285t	-7.3028t	
14	-4.4142t	-4.629t	-4.9018t	-5.1824t	-5.4527t	-5.7152t	**-6t**
13	0	0	0	0	0	0	0
12	**-4.1205t**	-4.1019t	-3.9503t	-3.8287t	-3.5009t	-3.2361t	-2.3028t
11	**-7.5209t**	-7.4412t	-7.0293t	-6.5704t	-5.8856t	-4.6056t	
10	-9.8407t	**-9.9917t**	-9.9107t	-9.2735t	-8.6215t	-6.9083t	
9	-11.498t	-11.7485t	**-12.0227t**	-11.2606t	-9.2111t		
8	-12.6485t	-12.819t	-13.2218t	**-13.9952t**	-11.5139t		
7	-13.2178t	-13.6182t	**-14.034t**	-13.8167t			
6	-13.3629t	-13.3112t	**-13.8504t**	-12.5139t			
5	-13.0425t	**-13.233t**	-11.2111t				
4	-12.5132t	**-12.5738t**	-9.9083t				
3	**-11.773t**	-8.6056t					
2	**-11.0828t**	-7.3028t					

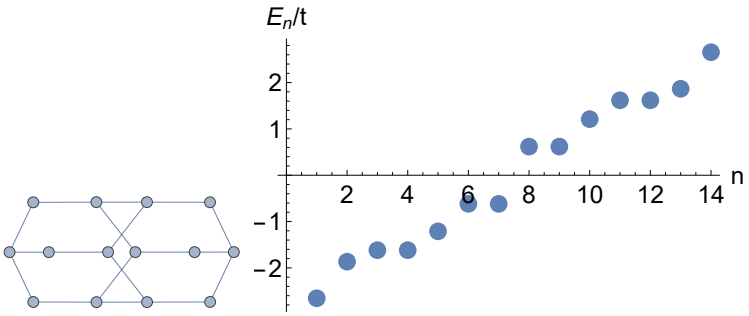

Figure B.18: Illustration of plaquette geometry (Left) and single particle energies (Right) for 14 dots: diamond lattice

14 dots: diamond lattice							
	Spin						
# of el.	0, 1/2	1, 3/2	2, 5/2	3, 7/2	4, 9/2	5, 11/2	6, 13/2
13, 15	-2.593t	-2.599t	-2.6119t	-2.6253t	-2.6339t	-2.6444t	**-2.6554t**
12, 16	**-4.7895t**	-4.7838t	-4.7671t	-4.7492t	-4.7385t	-4.6294t	-4.5216t
11, 17	-6.7058t	**-6.7155t**	-6.642t	-6.5838t	-6.567t	-6.1397t	
10, 18	**-8.3493t**	-8.3128t	-8.2818t	-8.1885t	-8.0084t	-7.7577t	
9, 19	**-9.2748t**	-9.244t	-9.2344t	-9.0984t	-8.9685t		
8, 20	**-9.9614t**	-9.9571t	-9.9493t	-9.9453t	-9.5865t		
7, 21	-9.9891t	-10.0439t	-10.1117t	**-10.2045t**			
6, 22	-9.7506t	**-9.7754t**	-9.7284t	-9.5865t			
5, 23	-8.975t	**-9.165t**	-8.9685t				
4, 24	-7.847t	**-7.9151t**	-7.7577t				
3, 25	**-6.6649t**	-6.1397t					
2, 26	**-4.9985t**	-4.5216t					

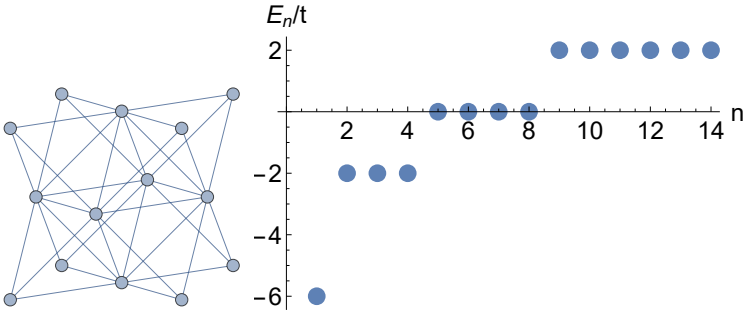

Figure B.19: Illustration of plaquette geometry (Left) and single particle energies (Right) for 14 dots: FCC lattice

14 dots: FCC lattice (cube corners and faces)							
	Spin						
# of el.	0, 1/2	1, 3/2	2, 5/2	3, 7/2	4, 9/2	5, 11/2	6, 13/2
26	**-4t**	**-4t**					
25	**-6t**	**-6t**					
24	-7.8209t	-7.9202t	**-8t**				
23	-9.6257t	-9.792t	**-10t**				
22	-11.3397t	-11.3635t	-11.5867t	**-12t**			
21	-11.6194t	-11.6732t	**-12.066t**	-12t			
20	-11.6194t	-11.5904t	-11.8483t	**-12.0059t**	-12t		
19	-11.2739t	-11.5348t	-11.7206t	-11.8831t	**-12t**		
18	-10.6634t	-11.1579t	-11.3907t	-11.6087t	-11.8118t	**-12t**	
17	-10.0182t	-10.1039t	-10.1845t	-10.2276t	**-10.243t**	-10t	
16	**-8.7516t**	-8.7107t	-8.6697t	-8.6092t	-8.5538t	-8.2416t	-8t
15	-5.2615t	-5.4334t	-5.5888t	-5.6933t	-5.7995t	-5.8997t	**-6t**
14	0	0	0	0	0	0	0
13	-3.7329t	**-3.7511t**	-3.7477t	-3.6176t	-3.3652t	-3t	-2t
12	-7.1039t	-7.1603t	**-7.2741t**	-6.8335t	-6.3276t	-5.6818t	-4t
11	-9.7551t	**-9.7789t**	-9.6215t	-8.8961t	-8.1484t	-6t	
10	**-12.1207t**	-11.9871t	-11.8019t	-11.5098t	-10.6477t	-8t	
9	**-13.3752t**	-13.2952t	-13.121t	-12.9747t	-10t		
8	**-14.5246t**	-14.3463t	-14.0359t	-13.5327t	-12t		
7	**-14.6024t**	-14.2983t	-13.8549t	-12t			
6	-14.2324t	**-14.5364t**	-14.1482t	-12t			
5	-13.9429t	**-14.3657t**	-12t				
4	-12.9965t	**-13.2403t**	-12t				
3	**-12.0265t**	-10t					
2	**-10.7633t**	-8t					

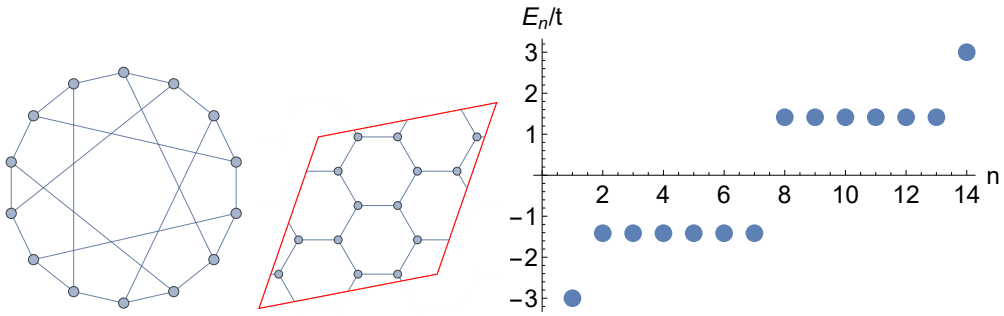

Figure B.20: Illustration of plaquette geometry (Left) and single particle energies (Right) for 14 dots: Heawood graph (hexagons with PBC)

14 dots: Heawood graph (hexagons with PBC)							
	Spin						
# of el.	0, 1/2	1, 3/2	2, 5/2	3, 7/2	4, 9/2	5, 11/2	6, 13/2
13, 15	-2.8389t	-2.8083t	-2.8259t	-2.8618t	-2.9148t	-2.9477t	**-3t**
12, 16	**-5.2483t**	-5.2275t	-5.1252t	-5.0448t	-4.9828t	-4.8928t	-4.4142t
11, 17	**-7.3059t**	-7.2518t	-7.1223t	-6.9363t	-6.5107t	-5.8284t	
10, 18	**-9.0061t**	-8.9841t	-8.9156t	-8.5495t	-8.0241t	-7.2426t	
9, 19	-10.0634t	-10.0469t	**-10.0938t**	-9.5609t	-8.6569t		
8, 20	-10.8095t	-10.7021t	-10.7533t	**-11.1262t**	-10.0711t		
7, 21	-10.7005t	-10.836t	-11.1354t	**-11.4853t**			
6, 22	-9.9128t	-10.0607t	**-10.3206t**	-10.0711t			
5, 23	-9.1832t	**-9.1906t**	-8.6569t				
4, 24	-8.0058t	**-8.0358t**	-7.2426t				
3, 25	**-6.8259t**	-5.8284t					
2, 26	**-5.6569t**	-4.4142t					

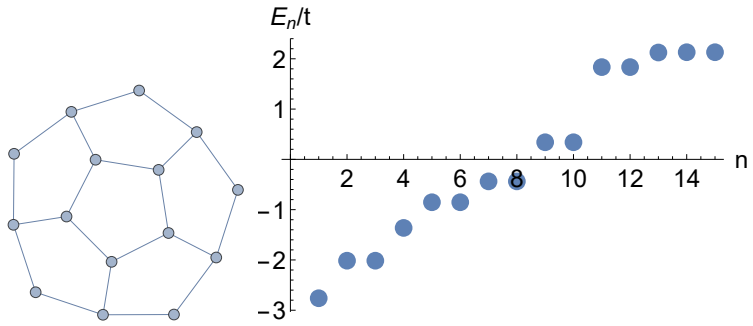

Figure B.21: Illustration of plaquette geometry (Left) and single particle energies (Right) for 15 dots: 6 adjacent pentagons

15 dots: 6 adjacent pentagons								
	Spin							
# of el.	0, 1/2	1, 3/2	2, 5/2	3, 7/2	4, 9/2	5, 11/2	6, 13/2	7
28	-4.1656t	**-4.261t**						
27	-6.2104t	**-6.3859t**						
26	-8.041t	**-8.241t**	-8.2206t					
25	-9.7301t	-9.8536t	**-10.0553t**					
24	-10.5774t	-10.6633t	**-10.7221t**	-10.3955t				
23	**-11.0792t**	-11.0193t	-10.8981t	-10.7357t				
22	**-11.1434t**	-11.0974t	-10.9806t	-10.8783t	-10.298t			
21	**-10.7828t**	-10.722t	-10.6327t	-10.1435t	-9.8604t			
20	**-10.0089t**	-9.921t	-9.8132t	-9.5486t	-9.3563t	-9.0077t		
19	**-8.6727t**	-8.5827t	-8.4358t	-8.3604t	-8.2785t	-8.155t		
18	-6.9682t	**-6.9991t**	-6.9221t	-6.8653t	-6.8325t	-6.8253t	-6.7917t	
17	**-4.9952t**	-4.9896t	-4.9808t	-4.9726t	-4.9694t	-4.9027t	-4.7766t	
16	-2.6776t	-2.6881t	-2.701t	-2.7135t	-2.726t	-2.7386t	-2.7495t	**-2.7616t**
15	0	0	0	0	0	0	0	0
14	**-2.6851t**	-2.6818t	-2.6765t	-2.6681t	-2.6388t	-2.5725t	-2.4528t	-2.1305t
13	-5.0292t	**-5.0331t**	-5.0218t	-5.0206t	-4.9224t	-4.7281t	-4.261t	
12	**-6.9623t**	-6.9552t	-6.9534t	-6.956t	-6.9545t	-6.6837t	-6.3859t	
11	-8.542t	-8.5681t	-8.5977t	-8.6152t	**-8.6389t**	-8.2206t		
10	-9.8367t	-9.853t	-9.8985t	-9.9529t	-10.0067t	**-10.0553t**		
9	-10.5t	-10.5615t	**-10.5803t**	-10.5673t	-10.3955t			
8	**-10.9259t**	-10.8696t	-10.8431t	-10.8018t	-10.7357t			
7	**-10.9384t**	-10.793t	-10.7796t	-10.298t				
6	**-10.6643t**	-10.4915t	-10.2417t	-9.8604t				
5	**-9.7389t**	-9.633t	-9.0077t					
4	-8.3722t	**-8.5969t**	-8.155t					
3	**-6.9472t**	-6.7917t						
2	**-5.2119t**	-4.7766t						

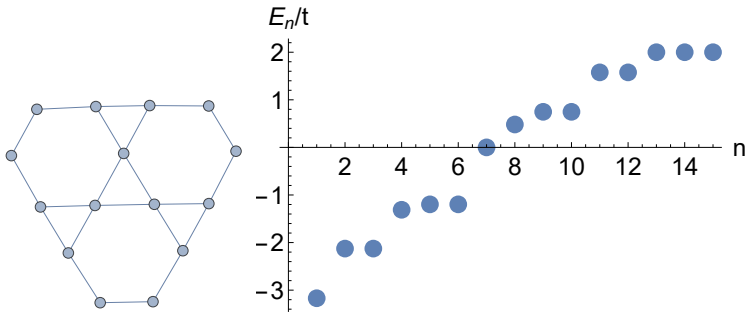

Figure B.22: Illustration of plaquette geometry (Left) and single particle energies (Right) for 15 dots: Kagome lattice

15 dots: Kagome lattice								
	Spin							
# of el.	0, 1/2	1, 3/2	2, 5/2	3, 7/2	4, 9/2	5, 11/2	6, 13/2	7
28	-3.9277t	**-4t**						
27	-5.8787t	**-6t**						
26	-7.4213t	**-7.5991t**	-7.5764t					
25	-8.9092t	-9.0222t	**-9.1528t**					
24	**-10.1696t**	-10.11t	-10.1066t	-9.9003t				
23	-10.7478t	**-10.8128t**	-10.7663t	-10.6478t				
22	-10.9083t	-11.0028t	-11.0315t	-11.0732t	**-11.129t**			
21	-10.8369t	-10.9169t	-10.9944t	-11.0684t	**-11.129t**			
20	-10.0649t	-10.0992t	-10.1195t	**-10.1389t**	-10.1282t	-9.9318t		
19	-8.9526t	-8.9717t	**-8.9863t**	-8.9146t	-8.8603t	-8.7347t		
18	-7.5772t	-7.5839t	-7.5922t	**-7.5996t**	-7.5299t	-7.4605t	-7.4236t	
17	-5.4241t	-5.4286t	-5.4323t	**-5.4351t**	-5.4267t	-5.4108t	-5.2968t	
16	-3.1477t	-3.1506t	-3.1532t	-3.1568t	-3.159t	-3.1628t	-3.1657t	**-3.1701t**
15	0	0	0	0	0	0	0	0
14	**-3.1363t**	**-3.1362t**	-3.1361t	-3.136t	-3.0327t	-2.8955t	-2.6492t	-2t
13	-5.4285t	**-5.4336t**	-5.4327t	-5.4302t	-5.2029t	-4.8018t	-4t	
12	**-7.5739t**	-7.5375t	-7.5017t	-7.4698t	-7.0525t	-6.6443t	-6t	
11	**-9.0721t**	-9.0462t	-8.9431t	-8.6048t	-8.4393t	-7.5764t		
10	-10.3647t	-10.3502t	**-10.3714t**	-9.8731t	-9.514t	-9.1528t		
9	**-11.3738t**	-11.3691t	-11.0776t	-10.5407t	-9.9003t			
8	**-11.7808t**	-11.752t	-11.7035t	-11.4988t	-10.6478t			
7	-11.6469t	-11.6703t	**-11.6974t**	-11.129t				
6	**-11.2495t**	-11.1487t	-11.1253t	-11.129t				
5	**-10.3727t**	-10.2133t	-9.9318t					
4	-9.023t	**-9.2046t**	-8.7347t					
3	**-7.6089t**	-7.4236t						
2	**-5.74t**	-5.2968t						

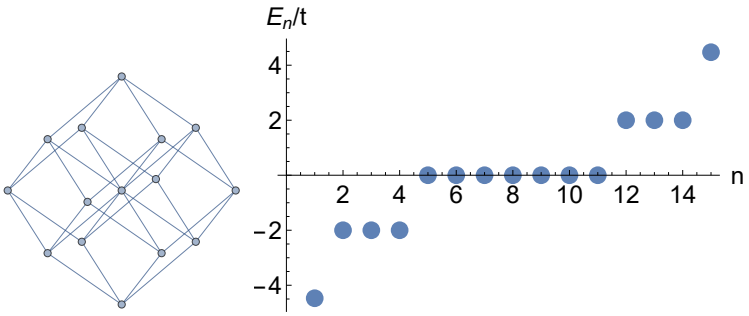

Figure B.23: Illustration of plaquette geometry (Left) and single particle energies (Right) for 15 dots: BCC lattice

15 dots: BCC lattice								
	Spin							
# of el.	0, 1/2	1, 3/2	2, 5/2	3, 7/2	4, 9/2	5, 11/2	6, 13/2	7
14, 16	-4.0336t	-4.046t	-4.0881t	-4.1553t	-4.2367t	-4.3111t	-4.3906t	**-4.4721t**
13, 17	-6.777t	-6.7898t	-6.8037t	**-6.8125t**	-6.7455t	-6.6735t	-6.4721t	
12, 18	-8.6685t	-8.6733t	-8.7133t	-8.7966t	-8.8849t	**-8.9866t**	-8.4721t	
11, 19	-10.3637t	-10.4068t	-10.4621t	-10.4353t	-10.4101t	**-10.4721t**		
10, 20	**-11.7632t**	-11.65t	-11.5352t	-11.4778t	-11.2915t	-10.4721t		
9, 21	**-12.8176t**	-12.6034t	-12.273t	-11.67t	-10.4721t			
8, 22	**-13.9409t**	-13.4546t	-12.8161t	-12.0214t	-10.4721t			
7, 23	**-13.7813t**	-13.1347t	-12.3597t	-10.4721t				
6, 24	-13.1295t	**-13.407t**	-12.6455t	-10.4721t				
5, 25	-12.5431t	**-12.9246t**	-10.4721t					
4, 26	-11.1801t	**-11.4094t**	-10.4721t					
3, 27	**-9.8352t**	-8.4721t						
2, 28	**-8.2267t**	-6.4721t						

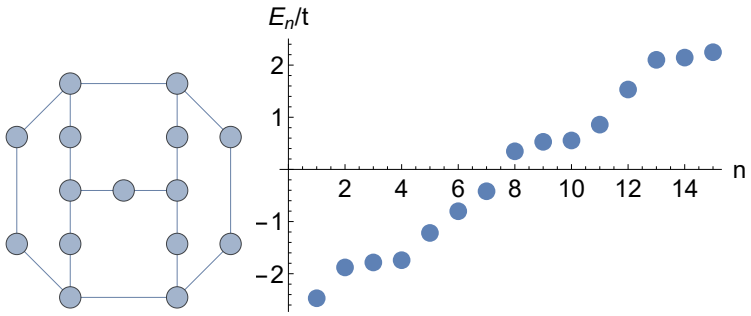

Figure B.24: Illustration of plaquette geometry (Left) and single particle energies (Right) for 15 dots: 4 septagons sharing 2 edges

15 dots: 4 septagons sharing 2 edges								
	Spin							
# of el.	0, 1/2	1, 3/2	2, 5/2	3, 7/2	4, 9/2	5, 11/2	6, 13/2	7
28	-4.3399t	**-4.3908t**						
27	-6.3644t	**-6.4917t**						
26	-7.9835t	**-8.0629t**	-8.0238t					
25	**-9.2471t**	-9.204t	-8.8822t					
24	**-10.063t**	-10.0386t	-9.7256t	-9.4372t				
23	**-10.518t**	-10.2588t	-10.1072t	-9.9659t				
22	**-10.4976t**	-10.3735t	-10.3333t	-10.3014t	-10.3132t			
21	-10.007t	**-10.0489t**	-10.0361t	-9.9644t	-9.8944t			
20	-9.2439t	-9.2405t	**-9.2529t**	-9.2406t	-9.1602t	-9.0925t		
19	**-8.072t**	-8.0658t	-8.0625t	-8.0642t	-7.9247t	-7.8742t		
18	**-6.5261t**	-6.5255t	-6.5214t	-6.5167t	-6.4794t	-6.394t	-6.1336t	
17	-4.63t	**-4.6304t**	-4.6187t	-4.6011t	-4.5782t	-4.5223t	-4.3496t	
16	-2.4408t	-2.4399t	-2.4432t	-2.4477t	-2.4498t	-2.4579t	-2.4615t	**-2.4702t**
15	0	0	0	0	0	0	0	0
14	**-2.4443t**	-2.4426t	-2.443t	-2.4413t	-2.4401t	-2.4372t	-2.3614t	-2.247t
13	**-4.6236t**	-4.6202t	-4.6152t	-4.6099t	-4.6006t	-4.5853t	-4.3908t	
12	**-6.5384t**	-6.5364t	-6.5205t	-6.5126t	-6.5193t	-6.5228t	-6.4917t	
11	**-8.0919t**	-8.0656t	-8.0635t	-8.0286t	-8.0213t	-8.0238t		
10	**-9.2679t**	-9.262t	-9.2369t	-9.1958t	-9.1132t	-8.8822t		
9	**-10.0966t**	-10.0529t	-9.9891t	-9.8099t	-9.4372t			
8	**-10.4911t**	-10.4441t	-10.393t	-10.3135t	-9.9659t			
7	**-10.3582t**	-10.3516t	-10.3317t	-10.3132t				
6	**-9.9983t**	-9.986t	-9.9727t	-9.8944t				
5	-9.1084t	**-9.194t**	-9.0925t					
4	-7.7905t	**-7.8786t**	-7.8742t					
3	**-6.3278t**	-6.1336t						
2	**-4.7218t**	-4.3496t						

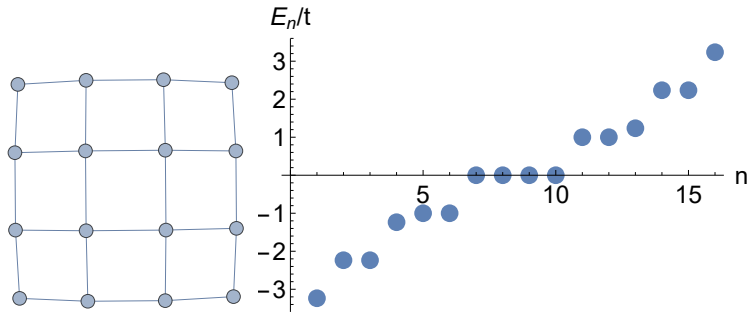

Figure B.25: Illustration of plaquette geometry (Left) and single particle energies (Right) for 16 dots: 4x4 square lattice

16 dots: 4x4 square lattice								
	Spin							
# of el.	0, 1/2	1, 3/2	2, 5/2	3, 7/2	4, 9/2	5, 11/2	6, 13/2	7, 15/2
15, 17	-3.118t	-3.1396t	-3.1578t	-3.1769t	-3.1933t	-3.2093t	-3.2227t	**-3.2361t**
14, 18	**-5.6674t**	-5.6632t	-5.6567t	-5.6462t	-5.6354t	-5.625t	-5.626t	-5.4721t
13, 19	-7.5776t	-7.6t	-7.624t	-7.6462t	-7.6692t	-7.6874t	**-7.7082t**	
12, 20	**-9.3304t**	-9.3214t	-9.3018t	-9.2592t	-9.2073t	-9.1191t	-8.9443t	
11, 21	-10.5029t	-10.5014t	**-10.5143t**	-10.4234t	-10.3663t	-9.9443t		
10, 22	-11.5156t	**-11.5237t**	-11.4496t	-11.4001t	-11.0648t	-10.9443t		
9, 23	**-12.2549t**	-12.2524t	-11.904t	-11.6522t	-10.9443t			
8, 24	**-12.6886t**	-12.5083t	-12.2862t	-11.821t	-10.9443t			
7, 25	**-12.5453t**	-12.179t	-12.0066t	-10.9443t				
6, 26	**-12.1331t**	-11.7623t	-11.4451t	-10.9443t				
5, 27	**-11.0317t**	-10.7191t	-9.9443t					
4, 28	-9.6005t	**-9.7525t**	-8.9443t					
3, 29	**-7.9326t**	-7.7082t						
2, 30	**-6.0156t**	-5.4721t						

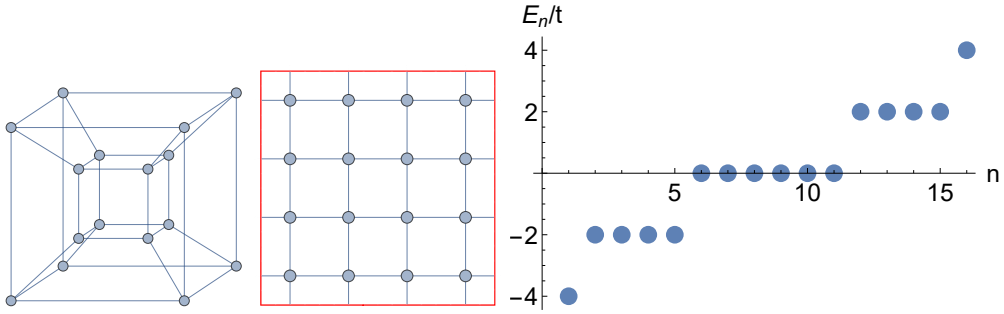

Figure B.26: Illustration of plaquette geometry (Left) and single particle energies (Right) for 16 dots: hypercube (4x4 square lattice with PBC)

16 dots: hypercube (4x4 square lattice with PBC)								
	Spin							
# of el.	0, 1/2	1, 3/2	2, 5/2	3, 7/2	4, 9/2	5, 11/2	6, 13/2	7, 15/2
15, 17	-3.4549t	-3.5186t	-3.6035t	-3.6911t	-3.7689t	-3.8484t	-3.924t	**-4t**
14, 18	**-6.6775t**	-6.643t	-6.6179t	-6.5687t	-6.5238t	-6.4117t	-6.2781t	-6t
13, 19	-8.6365t	-8.6968t	-8.7426t	**-8.8205t**	-8.7575t	-8.5486t	-8t	
12, 20	-10.6611t	-10.6424t	-10.6729t	-10.6823t	-10.7467t	**-10.8116t**	-10t	
11, 21	**-12.1808t**	-12.1425t	-12.1591t	-12.0006t	-11.9082t	-12t		
10, 22	**-13.7555t**	-13.3513t	-13.202t	-12.7418t	-12.3871t	-12t		
9, 23	**-14.1611t**	-13.7702t	-13.3162t	-12.7566t	-12t			
8, 24	**-14.3475t**	-14.2234t	-13.7099t	-13.1416t	-12t			
7, 25	-13.8398t	**-14.0605t**	-13.4586t	-12t				
6, 26	-13.3011t	-13.257t	**-13.8026t**	-12t				
5, 27	-12.0779t	**-12.3427t**	-12t					
4, 28	**-10.814t**	-10.7913t	-10t					
3, 29	**-9.1944t**	-8t						
2, 30	**-7.5696t**	-6t						

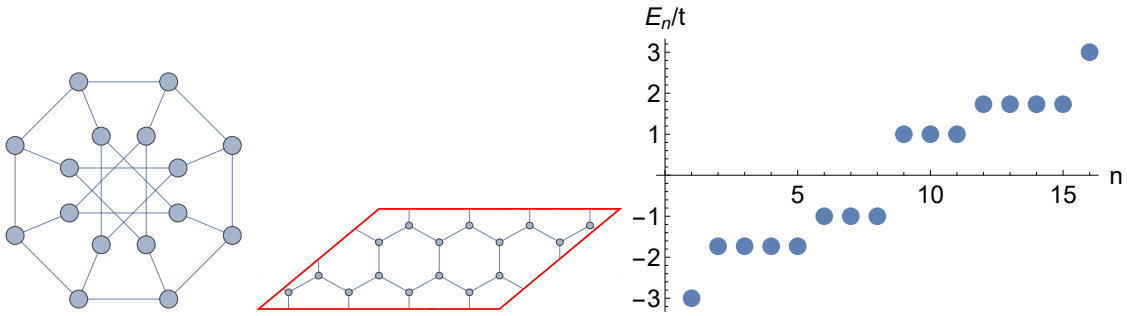

Figure B.27: Illustration of plaquette geometry (Left) and single particle energies (Right) for 16 dots: Mobius-Kantor graph (hexagons with PBC)

16 dots: Mobius-Kantor graph (hexagons with PBC)								
	Spin							
# of el.	0, 1/2	1, 3/2	2, 5/2	3, 7/2	4, 9/2	5, 11/2	6, 13/2	7, 15/2
15, 17	-2.8396t	-2.8379t	-2.8544t	-2.8799t	-2.9059t	-2.9396t	-2.9652t	**-3t**
14, 18	**-5.3152t**	-5.3044t	-5.2578t	-5.2204t	-5.186t	-5.1218t	-5.0402t	-4.7321t
13, 19	**-7.4952t**	-7.4692t	-7.406t	-7.3157t	-7.2562t	-6.9284t	-6.4641t	
12, 20	-9.3443t	**-9.3546t**	-9.3072t	-9.1263t	-8.884t	-8.8116t	-8.1962t	
11, 21	**-10.8322t**	-10.8302t	-10.8063t	-10.4843t	-10.1118t	-9.9282t		
10, 22	**-11.8867t**	-11.7957t	-11.8724t	-11.864t	-11.3916t	-10.9282t		
9, 23	-12.2914t	-12.3379t	-12.4179t	**-12.6624t**	-11.9282t			
8, 24	-12.6193t	-12.5361t	-12.5753t	-12.6746t	**-12.9282t**			
7, 25	-11.9385t	-12.0729t	**-12.1114t**	-11.9282t				
6, 26	-11.1999t	-11.2377t	**-11.5091t**	-10.9282t				
5, 27	-10.0982t	**-10.1133t**	-9.9282t					
4, 28	-8.6982t	**-8.6991t**	-8.1962t					
3, 29	**-7.2016t**	-6.4641t						
2, 30	**-5.7139t**	-4.7321t						

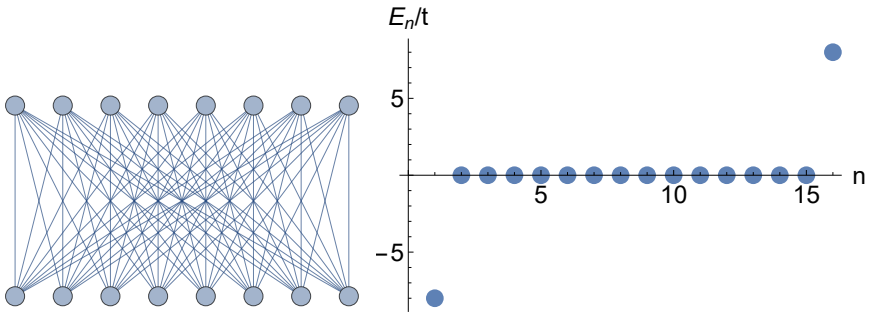

Figure B.28: Illustration of plaquette geometry (Left) and single particle energies (Right) for 16 dots: (8,8) complete bipartite graph (BCC with PBC)

16 dots: (8,8) complete bipartite graph (BCC with PBC)								
	Spin							
# of el.	0, 1/2	1, 3/2	2, 5/2	3, 7/2	4, 9/2	5, 11/2	6, 13/2	7, 15/2
15, 17	-4.899t	-5.3589t	-5.7854t	-6.2426t	-6.6695t	-7.1231t	-7.5498t	**-8t**
14, 18	**-8.9443t**	-8.8288t	-8.8318t	-8.7034t	-8.7178t	-8.5537t	-8.6023t	-8t
13, 19	**-9.3979t**	-9.3312t	-9.2945t	-9.2085t	-9.189t	-9.0627t	-8t	
12, 20	**-9.8995t**	**-9.8995t**	-9.7932t	-9.798t	-9.6784t	-9.6954t	-8t	
11, 21	**-10.4004t**	-10.3609t	-10.2956t	-10.2666t	-10.1831t	-8t		
10, 22	**-10.9545t**	-10.8614t	-10.8628t	-10.7634t	-10.7703t	-8t		
9, 23	**-11.4153t**	-11.3627t	-11.33t	-11.2662t	-8t			
8, 24	**-11.9164t**	**-11.9164t**	-11.8295t	-11.8322t	-8t			
7, 25	**-12.417t**	-12.3828t	-12.3311t	-8t				
6, 26	**-12.9615t**	-12.8833t	-12.8841t	-8t				
5, 27	**-13.4276t**	-13.3842t	-8t					
4, 28	**-13.9284t**	**-13.9284t**	-8t					
3, 29	**-14.4289t**	-8t						
2, 30	**-14.9666t**	-8t						

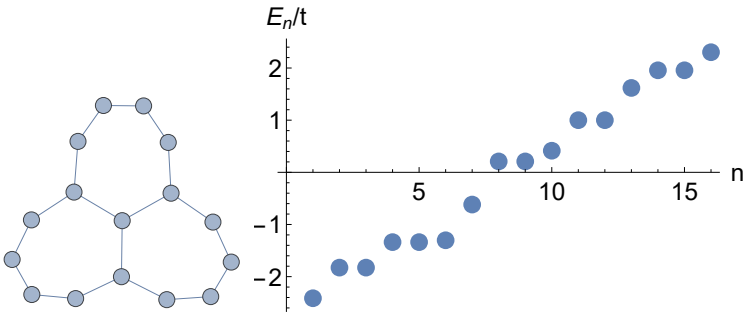

Figure B.29: Illustration of plaquette geometry (Left) and single particle energies (Right) for 16 dots: 3 adjacent septagons

16 dots: 3 adjacent septagons								
	Spin							
# of el.	0, 1/2	1, 3/2	2, 5/2	3, 7/2	4, 9/2	5, 11/2	6, 13/2	7, 15/2
30	-4.1201t	**-4.2591t**						
29	-6.0736t	**-6.2154t**						
28	-7.6673t	-7.7682t	**-7.8334t**					
27	**-9.1737t**	-9.1402t	-8.8334t					
26	**-10.1161t**	-10.0768t	-9.9276t	-9.8334t				
25	**-10.6977t**	-10.6014t	-10.5778t	-10.2476t				
24	**-10.9426t**	-10.8485t	-10.8101t	-10.6856t	-10.4567t			
23	-10.6471t	**-10.6764t**	-10.6567t	-10.6436t	-10.6657t			
22	-10.0788t	-10.0844t	-10.0862t	**-10.0953t**	-10.0706t	-10.0477t		
21	**-9.1672t**	-9.1642t	-9.1591t	-9.1514t	-9.1385t	-8.7449t		
20	**-7.8457t**	-7.8454t	-7.8438t	-7.8409t	-7.819t	-7.6521t	-7.4067t	
19	**-6.2447t**	-6.2438t	-6.2421t	-6.2396t	-6.1781t	-6.1502t	-6.0684t	
18	**-4.4433t**	-4.4427t	-4.4411t	-4.4393t	-4.4043t	-4.3777t	-4.3485t	-4.2413t
17	-2.4051t	-2.4065t	-2.4073t	-2.409t	-2.4095t	-2.4116t	-2.4119t	**-2.4142t**
16	0	0	0	0	0	0	0	0
15	-2.4069t	-2.4075t	-2.408t	-2.4085t	**-2.409t**	-2.3945t	-2.3628t	-2.3028t
14	**-4.4455t**	-4.4449t	-4.4437t	-4.4422t	-4.4396t	-4.436t	-4.4306t	-4.2591t
13	**-6.2397t**	**-6.2398t**	-6.2369t	-6.2363t	-6.2363t	-6.2264t	-6.2154t	
12	-7.8239t	-7.8272t	-7.8211t	-7.8173t	-7.8253t	-7.8222t	**-7.8334t**	
11	**-9.1331t**	-9.1293t	-9.0954t	-9.061t	-9.0222t	-8.8334t		
10	**-10.1053t**	-10.1001t	-10.0977t	-10.0106t	-9.9866t	-9.8334t		
9	**-10.7058t**	-10.7018t	-10.6735t	-10.4594t	-10.2476t			
8	**-10.9247t**	-10.9218t	-10.9129t	-10.8988t	-10.4567t			
7	-10.5866t	-10.6153t	-10.6412t	**-10.6657t**				
6	-9.9647t	-9.9713t	-10.0164t	**-10.0477t**				
5	**-9.0492t**	-8.9628t	-8.7449t					
4	-7.6562t	**-7.7809t**	-7.4067t					
3	**-6.1671t**	-6.0684t						
2	**-4.4983t**	-4.2413t						

List of Publications

Publications and preprints this thesis is based on:

1. Donovan Buterakos and Sankar Das Sarma. Ferromagnetism in quantum dot plaquettes. *Phys. Rev. B* **100**, 224421 (2019).

2. Donovan Buterakos and Sankar Das Sarma. Spin-valley qubit dynamics in exchange-coupled silicon quantum dots. *PRX Quantum* **2**, 040358 (2021).

3. Donovan Buterakos and Sankar Das Sarma. Certain exact many-body results for Hubbard model ground states testable in small quantum dot arrays. arXiv:2202.11115 (2022).

Other publications I contributed to:

1. Donovan Buterakos, Robert E. Throckmorton, and Sankar Das Sarma. Crosstalk error correction through dynamical decoupling of single-qubit gates in capacitively coupled singlet-triplet semiconductor spin qubits. *Phys. Rev. B* **97**, 045431 (2018).

2. Donovan Buterakos, Robert E. Throckmorton, and Sankar Das Sarma. Error correction for gate operations in systems of exchange-coupled singlet-triplet qubits in double quantum dots. *Phys. Rev. B* **98**, 035406 (2018).

3. Donovan Buterakos, Robert E. Throckmorton, and Sankar Das Sarma. Simulation of the coupling strength of capacitively coupled singlet-triplet qubits. *Phys. Rev. B* **100**, 075411 (2019).

4. Donovan Buterakos and Sankar Das Sarma. Coupled electron-impurity and electron-phonon systems as trivial non-Fermi liquids. *Phys. Rev. B* **100**, 235149 (2019).

5. Yunxiang Liao, Donovan Buterakos, Mike Schecter, and Sankar Das Sarma. Two-dimensional electron self-energy: Long-range Coulomb interaction. *Phys. Rev. B* **102**, 085145 (2020).

6. Donovan Buterakos, Sankar Das Sarma, and Edwin Barnes. Geometrical formalism for dynamically corrected gates in multiqubit systems. *PRX Quantum* **2**, 010341 (2021).

7. Donovan Buterakos, DinhDuy Vu, Jiabin Yu, and Sankar Das Sarma. Presence versus absence of two-dimensional Fermi surface anomalies. *Phys. Rev. B* **103**, 205154 (2021).

Bibliography

[1] Alexey I. Ekimov and Alexei A. Onushchenko. Quantum size effect in three-dimensional microscopic semiconductor crystals. *ZhETF Pisma Redaktsiiu*, 34:363, 1981.

[2] Alexander L. Efros and Al L. Efros. Interband absorption of light in a semiconductor sphere. *Sov. Phys. Semicond*, 16(7):772–775, 1982.

[3] F. Pelayo García de Arquer, Dmitri V. Talapin, Victor I. Klimov, Yasuhiko Arakawa, Manfred Bayer, and Edward H. Sargent. Semiconductor quantum dots: Technological progress and future challenges. *Science*, 373(6555):eaaz8541, 2021.

[4] Debasis Bera, Lei Qian, Teng-Kuan Tseng, and Paul H. Holloway. Quantum dots and their multimodal applications: A review. *Materials*, 3(4):2260–2345, Mar 2010. PMC5445848[pmcid].

[5] Daniel Loss and David P. DiVincenzo. Quantum computation with quantum dots. *Phys. Rev. A*, 57:120–126, Jan 1998.

[6] Frank Arute, Kunal Arya, Ryan Babbush, Dave Bacon, Joseph C. Bardin, Rami Barends, Rupak Biswas, Sergio Boixo, Fernando G. S. L. Brandao, David A. Buell, Brian Burkett, Yu Chen, Zijun Chen, Ben Chiaro, Roberto Collins, William Courtney, Andrew Dunsworth, Edward Farhi, Brooks Foxen, Austin Fowler, Craig Gidney, Marissa Giustina, Rob Graff, Keith Guerin, Steve Habegger, Matthew P. Harrigan, Michael J. Hartmann, Alan Ho, Markus Hoffmann, Trent Huang, Travis S. Humble, Sergei V. Isakov, Evan Jeffrey, Zhang Jiang, Dvir Kafri, Kostyantyn Kechedzhi, Julian Kelly, Paul V. Klimov, Sergey Knysh, Alexander Korotkov, Fedor Kostritsa, David Landhuis, Mike Lindmark, Erik Lucero, Dmitry Lyakh, Salvatore Mandrà, Jarrod R. McClean, Matthew McEwen, Anthony Megrant, Xiao Mi, Kristel Michielsen, Masoud Mohseni, Josh Mutus, Ofer Naaman, Matthew Neeley, Charles Neill, Murphy Yuezhen Niu, Eric Ostby, Andre Petukhov, John C. Platt, Chris Quintana, Eleanor G. Rieffel, Pedram Roushan, Nicholas C. Rubin, Daniel Sank, Kevin J. Satzinger, Vadim Smelyanskiy, Kevin J. Sung, Matthew D. Trevithick, Amit Vainsencher, Benjamin Villalonga, Theodore White, Z. Jamie Yao, Ping Yeh, Adam Zalcman, Hartmut Neven, and John M. Martinis. Quantum supremacy using a programmable superconducting processor. *Nature*, 574(7779):505–510, Oct 2019.

[7] John M. Nichol, Lucas A. Orona, Shannon P. Harvey, Saeed Fallahi, Geoffrey C. Gardner, Michael J. Manfra, and Amir Yacoby. High-fidelity entangling gate for double-quantum-dot spin qubits. *npj Quantum Information*, 3(1):3, Jan 2017.

[8] Nico W. Hendrickx, William I. L. Lawrie, Maximilian Russ, Floor van Riggelen, Sander L. de Snoo, Raymond N. Schouten, Amir Sammak, Giordano Scappucci, and Menno Veldhorst. A four-qubit germanium quantum processor. *Nature*, 591(7851):580–585, Mar

2021.

[9] J. P. Dehollain, U. Mukhopadhyay, V. P. Michal, Y. Wang, B. Wunsch, C. Reichl, W. Wegscheider, M. S. Rudner, E. Demler, and L. M. K. Vandersypen. Nagaoka ferromagnetism observed in a quantum dot plaquette. *Nature*, 579(7800):528–533, Mar 2020.

[10] D. M. Zajac, T. M. Hazard, X. Mi, E. Nielsen, and J. R. Petta. Scalable gate architecture for a one-dimensional array of semiconductor spin qubits. *Phys. Rev. Applied*, 6:054013, Nov 2016.

[11] A. R. Mills, D. M. Zajac, M. J. Gullans, F. J. Schupp, T. M. Hazard, and J. R. Petta. Shuttling a single charge across a one-dimensional array of silicon quantum dots. *Nature Communications*, 10(1):1063, Mar 2019.

[12] A. M. Turing. On computable numbers, with an application to the entscheidungsproblem. *J. of Math*, 58(345-363):5, 1936.

[13] A. Church. An unsolvable problem of elementary number theory. *American Journal of Mathematics*, 58(2):345–363, 1936.

[14] Wikipedia contributors. Churchturing thesis — wikipedia, the free encyclopedia, 2022. [Online; accessed 29-March-2022].

[15] P Benioff. Computer as a physical system: a microscopic quantum mechanical hamiltonian model of computers represented by turing machines. *J. Stat. Phys.; (United States)*, 22(5), 1 1980.

[16] Paul Benioff. Quantum mechanical hamiltonian models of turing machines. *Journal of Statistical Physics*, 29(3):515–546, Nov 1982.

[17] Richard P. Feynman. Simulating physics with computers. *International Journal of Theoretical Physics*, 21(6):467–488, Jun 1982.

[18] Y. Manin. Computable and uncomputable. *Sov. Radio*, 21, 1980.

[19] David Deutsch. Quantum theory, the church-turing principle and the universal quantum computer. *Proc. R. Soc. Lond. A*, 400:97117, 1985.

[20] Peter W Shor. Algorithms for quantum computation: discrete logarithms and factoring. In *Proceedings 35th annual symposium on foundations of computer science*, pages 124–134. IEEE, 1994.

[21] Peter W. Shor. Polynomial-time algorithms for prime factorization and discrete logarithms on a quantum computer. *SIAM Journal on Computing*, 26(5):14841509, Oct 1997.

[22] R. L. Rivest, A. Shamir, and L. Adleman. A method for obtaining digital signatures and public-key cryptosystems. *Commun. ACM*, 21(2):120126, Feb 1978.

[23] Lov K. Grover. Quantum mechanics helps in searching for a needle in a haystack. *Phys. Rev. Lett.*, 79:325–328, Jul 1997.

[24] Charles H. Bennett and Gilles Brassard. Quantum cryptography: Public key distribution and coin tossing. *Theoretical Computer Science*, 560:711, Dec 2014.

[25] W. K. Wootters and W. H. Zurek. A single quantum cannot be cloned. *Nature*, 299(5886):802–803, Oct 1982.

[26] W. M. Witzel and S. Das Sarma. Multiple-pulse coherence enhancement of solid state spin qubits. *Phys. Rev. Lett.*, 98:077601, Feb 2007.

[27] B. Lee, W. M. Witzel, and S. Das Sarma. Universal pulse sequence to minimize spin dephasing in the central spin decoherence problem. *Phys. Rev. Lett.*, 100:160505, Apr 2008.

[28] Xin Wang, Lev S. Bishop, J. P. Kestner, Edwin Barnes, Kai Sun, and S. Das Sarma. Composite pulses for robust universal control of singlet–triplet qubits. *Nature Communications*, 3(1):997, Aug 2012.

[29] Xin Wang, Lev S. Bishop, Edwin Barnes, J. P. Kestner, and S. Das Sarma. Robust quantum gates for singlet-triplet spin qubits using composite pulses. *Phys. Rev. A*, 89:022310, Feb 2014.

[30] Robert E. Throckmorton, Chengxian Zhang, Xu-Chen Yang, Xin Wang, Edwin Barnes, and S. Das Sarma. Fast pulse sequences for dynamically corrected gates in singlet-triplet qubits. *Phys. Rev. B*, 96:195424, Nov 2017.

[31] Donovan Buterakos, Robert E. Throckmorton, and S. Das Sarma. Crosstalk error correction through dynamical decoupling of single-qubit gates in capacitively coupled singlet-triplet semiconductor spin qubits. *Phys. Rev. B*, 97:045431, Jan 2018.

[32] Donovan Buterakos, Robert E. Throckmorton, and S. Das Sarma. Error correction for gate operations in systems of exchange-coupled singlet-triplet qubits in double quantum dots. *Phys. Rev. B*, 98:035406, Jul 2018.

[33] Junkai Zeng, Xiu-Hao Deng, Antonio Russo, and Edwin Barnes. General solution to inhomogeneous dephasing and smooth pulse dynamical decoupling. *New Journal of Physics*, 20(3):033011, mar 2018.

[34] Junkai Zeng, C. H. Yang, A. S. Dzurak, and Edwin Barnes. Geometric formalism for constructing arbitrary single-qubit dynamically corrected gates. *Phys. Rev. A*, 99:052321, May 2019.

[35] Donovan Buterakos, Sankar Das Sarma, and Edwin Barnes. Geometrical formalism for dynamically corrected gates in multiqubit systems. *PRX Quantum*, 2:010341, Mar 2021.

[36] A.Yu. Kitaev. Fault-tolerant quantum computation by anyons. *Annals of Physics*, 303(1):2–30, 2003.

[37] R. Raussendorf, J. Harrington, and K. Goyal. Topological fault-tolerance in cluster state quantum computation. *New Journal of Physics*, 9(6):199–199, jun 2007.

[38] Austin G. Fowler, Ashley M. Stephens, and Peter Groszkowski. High-threshold universal quantum computation on the surface code. *Phys. Rev. A*, 80:052312, Nov 2009.

[39] David Wang, Austin Fowler, Ashley Stephens, and Lloyd Hollenberg. Threshold error rates for the toric and planar codes. *Quantum Information Computation*, 10:456–469, 05 2010.

[40] Jeremy Levy. Universal quantum computation with spin-$1/2$ pairs and heisenberg exchange. *Phys. Rev. Lett.*, 89:147902, Sep 2002.

[41] D. P. DiVincenzo, D. Bacon, J. Kempe, G. Burkard, and K. B. Whaley. Universal quantum computation with the exchange interaction. *Nature*, 408(6810):339–342, Nov 2000.

[42] J. Medford, J. Beil, J. M. Taylor, S. D. Bartlett, A. C. Doherty, E. I. Rashba, D. P. DiVincenzo, H. Lu, A. C. Gossard, and C. M. Marcus. Self-consistent measurement and state tomography of an exchange-only spin qubit. *Nature Nanotechnology*, 8(9):654–659, Sep 2013.

[43] Zhan Shi, C. B. Simmons, J. R. Prance, John King Gamble, Teck Seng Koh, Yun-Pil Shim, Xuedong Hu, D. E. Savage, M. G. Lagally, M. A. Eriksson, Mark Friesen, and S. N. Coppersmith. Fast hybrid silicon double-quantum-dot qubit. *Phys. Rev. Lett.*, 108:140503, Apr 2012.

[44] Dohun Kim, Zhan Shi, C. B. Simmons, D. R. Ward, J. R. Prance, Teck Seng Koh, John King Gamble, D. E. Savage, M. G. Lagally, Mark Friesen, S. N. Coppersmith, and Mark A. Eriksson. Quantum control and process tomography of a semiconductor quantum dot hybrid qubit. *Nature*, 511(7507):70–74, Jul 2014.

[45] M. D. Shulman, O. E. Dial, S. P. Harvey, H. Bluhm, V. Umansky, and A. Yacoby. Demonstration of entanglement of electrostatically coupled singlet-triplet qubits. *Science*, 336(6078):202–205, 2012.

[46] X. Mi, J. V. Cady, D. M. Zajac, P. W. Deelman, and J. R. Petta. Strong coupling of a single electron in silicon to a microwave photon. *Science*, 355(6321):156–158, 2017.

[47] Anasua Chatterjee, Paul Stevenson, Silvano De Franceschi, Andrea Morello, Nathalie P. de Leon, and Ferdinand Kuemmeth. Semiconductor qubits in practice. *Nature Reviews Physics*, 3(3):157–177, Mar 2021.

[48] Daniel Jirovec, Andrea Hofmann, Andrea Ballabio, Philipp M. Mutter, Giulio Tavani, Marc Botifoll, Alessandro Crippa, Josip Kukucka, Oliver Sagi, Frederico Martins, Jaime Saez-Mollejo, Ivan Prieto, Maksim Borovkov, Jordi Arbiol, Daniel Chrastina, Giovanni Isella, and Georgios Katsaros. A singlet-triplet hole spin qubit in planar ge. *Nature Materials*, 20(8):1106–1112, Aug 2021.

[49] F. van Riggelen, N. W. Hendrickx, W. I. L. Lawrie, M. Russ, A. Sammak, G. Scappucci, and M. Veldhorst. A two-dimensional array of single-hole quantum dots. *Applied Physics Letters*, 118(4):044002, 2021.

[50] Jun Yoneda, Kenta Takeda, Tomohiro Otsuka, Takashi Nakajima, Matthieu R. Delbecq, Giles Allison, Takumu Honda, Tetsuo Kodera, Shunri Oda, Yusuke Hoshi, Noritaka Usami, Kohei M. Itoh, and Seigo Tarucha. A quantum-dot spin qubit with coherence limited by charge noise and fidelity higher than 99.9%. *Nature Nanotechnology*, 13(2):102–106, Feb 2018.

[51] K. Takeda, A. Noiri, J. Yoneda, T. Nakajima, and S. Tarucha. Resonantly driven singlet-triplet spin qubit in silicon. *Phys. Rev. Lett.*, 124:117701, Mar 2020.

[52] W. Huang, C. H. Yang, K. W. Chan, T. Tanttu, B. Hensen, R. C. C. Leon, M. A. Fogarty, J. C. C. Hwang, F. E. Hudson, K. M. Itoh, A. Morello, A. Laucht, and A. S. Dzurak. Fidelity benchmarks for two-qubit gates in silicon. *Nature*, 569(7757):532–536, May 2019.

[53] X. Xue, T. F. Watson, J. Helsen, D. R. Ward, D. E. Savage, M. G. Lagally, S. N. Coppersmith, M. A. Eriksson, S. Wehner, and L. M. K. Vandersypen. Benchmarking gate fidelities in a $\mathrm{Si/SiGe}$ two-qubit device. *Phys. Rev. X*, 9:021011, Apr 2019.

[54] M. A. Reed, J. N. Randall, R. J. Aggarwal, R. J. Matyi, T. M. Moore, and A. E. Wetsel. Observation of discrete electronic states in a zero-dimensional semiconductor nanostructure. *Phys. Rev. Lett.*, 60:535–537, Feb 1988.

[55] A. L. Saraiva, M. J. Calderón, Xuedong Hu, S. Das Sarma, and Belita Koiller. Physical mechanisms of interface-mediated intervalley coupling in si. *Phys. Rev. B*, 80:081305, Aug 2009.

[56] A. L. Saraiva, M. J. Calderón, Rodrigo B. Capaz, Xuedong Hu, S. Das Sarma, and Belita Koiller. Intervalley coupling for interface-bound electrons in silicon: An effective mass study. *Phys. Rev. B*, 84:155320, Oct 2011.

[57] F. Borjans, X. Zhang, X. Mi, G. Cheng, N. Yao, C.A.C. Jackson, L.F. Edge, and J.R. Petta. Probing the variation of the intervalley tunnel coupling in a silicon triple quantum dot. *PRX Quantum*, 2:020309, Apr 2021.

[58] J. Hubbard. Electron correlations in narrow energy bands. *Proc. R. Soc. Lond. A*, 276:238–257, 1963.

[59] C. A. Stafford and S. Das Sarma. Collective coulomb blockade in an array of quantum dots: A mott-hubbard approach. *Phys. Rev. Lett.*, 72:3590–3593, May 1994.

[60] R. Kotlyar, C. A. Stafford, and S. Das Sarma. Addition spectrum, persistent current, and spin polarization in coupled quantum dot arrays: Coherence, correlation, and disorder. *Phys. Rev. B*, 58:3989–4013, Aug 1998.

[61] R. Kotlyar, C. A. Stafford, and S. Das Sarma. Correlated charge polarization in a chain of coupled quantum dots. *Phys. Rev. B*, 58:R1746–R1749, Jul 1998.

[62] Yosuke Nagaoka. Ferromagnetism in a narrow, almost half-filled s band. *Phys. Rev.*, 147:392–405, Jul 1966.

[63] Hal Tasaki. From Nagaoka's Ferromagnetism to Flat-Band Ferromagnetism and Beyond: An Introduction to Ferromagnetism in the Hubbard Model. *Progress of Theoretical Physics*, 99(4):489–548, 04 1998.

[64] E. Kawakami, P. Scarlino, D. R. Ward, F. R. Braakman, D. E. Savage, M. G. Lagally, Mark Friesen, S. N. Coppersmith, M. A. Eriksson, and L. M. K. Vandersypen. Electrical control of a long-lived spin qubit in a si/sige quantum dot. *Nature Nanotechnology*, 9(9):666–670, Sep 2014.

[65] M. Veldhorst, C. H. Yang, J. C. C. Hwang, W. Huang, J. P. Dehollain, J. T. Muhonen, S. Simmons, A. Laucht, F. E. Hudson, K. M. Itoh, A. Morello, and A. S. Dzurak. A two-qubit logic gate in silicon. *Nature*, 526(7573):410–414, Oct 2015.

[66] R. Maurand, X. Jehl, D. Kotekar-Patil, A. Corna, H. Bohuslavskyi, R. Laviéville, L. Hutin, S. Barraud, M. Vinet, M. Sanquer, and S. De Franceschi. A cmos silicon spin qubit. *Nature Communications*, 7(1):13575, Nov 2016.

[67] M. A. Fogarty, K. W. Chan, B. Hensen, W. Huang, T. Tanttu, C. H. Yang, A. Laucht, M. Veldhorst, F. E. Hudson, K. M. Itoh, D. Culcer, T. D. Ladd, A. Morello, and A. S. Dzurak. Integrated silicon qubit platform with single-spin addressability, exchange control and single-shot singlet-triplet readout. *Nature Communications*, 9(1):4370, Oct 2018.

[68] T. F. Watson, S. G. J. Philips, E. Kawakami, D. R. Ward, P. Scarlino, M. Veldhorst, D. E. Savage, M. G. Lagally, Mark Friesen, S. N. Coppersmith, M. A. Eriksson, and L. M. K. Vandersypen. A programmable two-qubit quantum processor in silicon. *Nature*, 555(7698):633–637, Mar 2018.

[69] D. M. Zajac, A. J. Sigillito, M. Russ, F. Borjans, J. M. Taylor, G. Burkard, and J. R. Petta. Resonantly driven cnot gate for electron spins. *Science*, 359(6374):439–442, 2018.

[70] A. J. Sigillito, M. J. Gullans, L. F. Edge, M. Borselli, and J. R. Petta. Coherent transfer of quantum information in a silicon double quantum dot using resonant swap gates. *npj Quantum Information*, 5(1):110, Nov 2019.

[71] R. Zhao, T. Tanttu, K. Y. Tan, B. Hensen, K. W. Chan, J. C. C. Hwang, R. C. C. Leon, C. H. Yang, W. Gilbert, F. E. Hudson, K. M. Itoh, A. A. Kiselev, T. D. Ladd, A. Morello, A. Laucht, and A. S. Dzurak. Single-spin qubits in isotopically enriched silicon at low magnetic field. *Nature Communications*, 10(1):5500, Dec 2019.

[72] F. Borjans, X. G. Croot, X. Mi, M. J. Gullans, and J. R. Petta. Resonant microwave-mediated interactions between distant electron spins. *Nature*, 577(7789):195–198, Jan 2020.

[73] L. Petit, H. G. J. Eenink, M. Russ, W. I. L. Lawrie, N. W. Hendrickx, S. G. J. Philips, J. S. Clarke, L. M. K. Vandersypen, and M. Veldhorst. Universal quantum logic in hot silicon qubits. *Nature*, 580(7803):355–359, Apr 2020.

[74] Xiao Xue, Benjamin D'Anjou, Thomas F. Watson, Daniel R. Ward, Donald E. Savage, Max G. Lagally, Mark Friesen, Susan N. Coppersmith, Mark A. Eriksson, William A. Coish, and Lieven M. K. Vandersypen. Repetitive quantum nondemolition measurement and soft decoding of a silicon spin qubit. *Phys. Rev. X*, 10:021006, Apr 2020.

[75] C. H. Yang, R. C. C. Leon, J. C. C. Hwang, A. Saraiva, T. Tanttu, W. Huang, J. Camirand Lemyre, K. W. Chan, K. Y. Tan, F. E. Hudson, K. M. Itoh, A. Morello, M. Pioro-Ladrière, A. Laucht, and A. S. Dzurak. Operation of a silicon quantum processor unit cell above one kelvin. *Nature*, 580(7803):350–354, Apr 2020.

[76] Wayne M. Witzel, Malcolm S. Carroll, Andrea Morello, Łukasz Cywiński, and S. Das Sarma. Electron spin decoherence in isotope-enriched silicon. *Phys. Rev. Lett.*, 105:187602, Oct 2010.

[77] Patrik Recher, Johan Nilsson, Guido Burkard, and Björn Trauzettel. Bound states and magnetic field induced valley splitting in gate-tunable graphene quantum dots. *Phys. Rev. B*, 79:085407, Feb 2009.

[78] Dimitrie Culcer, A. L. Saraiva, Belita Koiller, Xuedong Hu, and S. Das Sarma. Valley-based noise-resistant quantum computation using si quantum dots. *Phys. Rev. Lett.*, 108:126804, Mar 2012.

[79] Niklas Rohling and Guido Burkard. Universal quantum computing with spin and valley states. *New Journal of Physics*, 14(8):083008, aug 2012.

[80] J. Corrigan, J. P. Dodson, H. Ekmel Ercan, J. C. Abadillo-Uriel, Brandur Thorgrimsson, T. J. Knapp, Nathan Holman, Thomas McJunkin, Samuel F. Neyens, E. R. MacQuarrie, Ryan H. Foote, L. F. Edge, Mark Friesen, S. N. Coppersmith, and M. A. Eriksson. Coherent control and spectroscopy of a semiconductor quantum dot wigner molecule. 2020. arXiv:2009.13572.

[81] J. P. Dodson, H. Ekmel Ercan, J. Corrigan, Merritt Losert, Nathan Holman, Thomas McJunkin, L. F. Edge, Mark Friesen, S. N. Coppersmith, and M. A. Eriksson. How valley-orbit states in silicon quantum dots probe quantum well interfaces. 2021. arXiv:2103.14702.

[82] Brian Paquelet Wuetz, Merritt P. Losert, Alberto Tosato, Mario Lodari, Peter L. Bavdaz, Lucas Stehouwer, Payam Amin, James S. Clarke, Susan N. Coppersmith, Amir Sammak, Menno Veldhorst, Mark Friesen, and Giordano Scappucci. Effect of quantum hall edge strips on valley splitting in silicon quantum wells. *Phys. Rev. Lett.*, 125:186801, Oct 2020.

[83] Yun-Pil Shim, Rusko Ruskov, Hilary M. Hurst, and Charles Tahan. Induced quantum dot probe for material characterization. *Applied Physics Letters*, 114(15):152105, 2019.

[84] Seong Woo Oh, Artem O. Denisov, Pengcheng Chen, and Jason R. Petta. Cryogen-free scanning gate microscope for the characterization of si/$si_{0.7}ge_{0.3}$ quantum devices at millikelvin temperatures. 2021. arXiv:2105.05684.

[85] Zhengping Jiang, Neerav Kharche, Timothy Boykin, and Gerhard Klimeck. Effects of interface disorder on valley splitting in sige/si/sige quantum wells. *Applied Physics Letters*, 100(10):103502, 2012.

[86] Bilal Tariq and Xuedong Hu. Effects of interface steps on the valley-orbit coupling in a si/sige quantum dot. *Phys. Rev. B*, 100:125309, Sep 2019.

[87] C. H. Yang, W. H. Lim, N. S. Lai, A. Rossi, A. Morello, and A. S. Dzurak. Orbital and valley state spectra of a few-electron silicon quantum dot. *Phys. Rev. B*, 86:115319, Sep 2012.

[88] A.J. Sigillito, J.C. Loy, D.M. Zajac, M.J. Gullans, L.F. Edge, and J.R. Petta. Site-selective quantum control in an isotopically enriched $^{28}\mathrm{Si}/\mathrm{si}_{0.7}\mathrm{ge}_{0.3}$ quadruple quantum dot. *Phys. Rev. Applied*, 11:061006, Jun 2019.

[89] Samuel F. Neyens, Ryan H. Foote, Brandur Thorgrimsson, T. J. Knapp, Thomas McJunkin, L. M. K. Vandersypen, Payam Amin, Nicole K. Thomas, James S. Clarke, D. E. Savage, M. G. Lagally, Mark Friesen, S. N. Coppersmith, and M. A. Eriksson. The critical role of substrate disorder in valley splitting in si quantum wells. *Applied Physics Letters*, 112(24):243107, 2018.

[90] Donovan Buterakos and Sankar Das Sarma. Spin-valley qubit dynamics in exchange-coupled silicon quantum dots. *PRX Quantum*, 2:040358, Dec 2021.

[91] S. Das Sarma, Xin Wang, and Shuo Yang. Hubbard model description of silicon spin qubits: Charge stability diagram and tunnel coupling in si double quantum dots. *Phys. Rev. B*, 83:235314, Jun 2011.

[92] Shuo Yang, Xin Wang, and S. Das Sarma. Generic hubbard model description of semiconductor quantum-dot spin qubits. *Phys. Rev. B*, 83:161301, Apr 2011.

[93] Jason Kestner. private communication.

[94] C. H. Yang, A. Rossi, R. Ruskov, N. S. Lai, F. A. Mohiyaddin, S. Lee, C. Tahan, G. Klimeck, A. Morello, and A. S. Dzurak. Spin-valley lifetimes in a silicon quantum dot with tunable valley splitting. *Nature Communications*, 4(1):2069, Jun 2013.

[95] J. K. Gamble, P. Harvey-Collard, N. T. Jacobson, A. D. Baczewski, E. Nielsen, L. Maurer, I. Montaño, M. Rudolph, M. S. Carroll, C. H. Yang, A. Rossi, A. S. Dzurak, and R. P. Muller. Valley splitting of single-electron si mos quantum dots. *Applied Physics Letters*, 109(25):253101, 2016.

[96] Junjiro Kanamori. Electron Correlation and Ferromagnetism of Transition Metals. *Progress of Theoretical Physics*, 30(3):275–289, 09 1963.

[97] Martin C. Gutzwiller. Effect of correlation on the ferromagnetism of transition metals. *Phys. Rev. Lett.*, 10:159–162, Mar 1963.

[98] J. P. F. LeBlanc, Andrey E. Antipov, Federico Becca, Ireneusz W. Bulik, Garnet Kin-Lic Chan, Chia-Min Chung, Youjin Deng, Michel Ferrero, Thomas M. Henderson, Carlos A. Jiménez-Hoyos, E. Kozik, Xuan-Wen Liu, Andrew J. Millis, N. V. Prokof'ev, Mingpu Qin, Gustavo E. Scuseria, Hao Shi, B. V. Svistunov, Luca F. Tocchio, I. S. Tupitsyn, Steven R. White, Shiwei Zhang, Bo-Xiao Zheng, Zhenyue Zhu, and Emanuel Gull. Solutions of the two-dimensional hubbard model: Benchmarks and results from a wide range of numerical algorithms. *Phys. Rev. X*, 5:041041, Dec 2015.

[99] Eric Bobrow and Yi Li. Stability of the nagaoka-type ferromagnetic state in a t_{2g} orbital system on a cubic lattice. *Phys. Rev. B*, 97:155132, Apr 2018.

[100] Eric Bobrow, Keaton Stubis, and Yi Li. Exact results on itinerant ferromagnetism and the 15-puzzle problem. *Phys. Rev. B*, 98:180101, Nov 2018.

[101] T. Hensgens, T. Fujita, L. Janssen, Xiao Li, C. J. Van Diepen, C. Reichl, W. Wegscheider, S. Das Sarma, and L. M. K. Vandersypen. Quantum simulation of a fermi–hubbard model using a semiconductor quantum dot array. *Nature*, 548(7665):70–73, Aug 2017.

[102] C. J. van Diepen, P. T. Eendebak, B. T. Buijtendorp, U. Mukhopadhyay, T. Fujita, C. Reichl, W. Wegscheider, and L. M. K. Vandersypen. Automated tuning of inter-dot tunnel coupling in double quantum dots. *Applied Physics Letters*, 113(3):033101, 2018.

[103] H. G. J. Eenink, L. Petit, W. I. L. Lawrie, J. S. Clarke, L. M. K. Vandersypen, and M. Veldhorst. Tunable coupling and isolation of single electrons in silicon metal-oxide-semiconductor quantum dots. *Nano Letters*, 19(12):8653–8657, Dec 2019.

[104] A. R. Mills, M. M. Feldman, C. Monical, P. J. Lewis, K. W. Larson, A. M. Mounce, and J. R. Petta. Computer-automated tuning procedures for semiconductor quantum dot arrays. *Applied Physics Letters*, 115(11):113501, 2019.

[105] Hanno Flentje, Benoit Bertrand, Pierre-André Mortemousque, Vivien Thiney, Arne Ludwig, Andreas D. Wieck, Christopher Bäuerle, and Tristan Meunier. A linear triple quantum dot system in isolated configuration. *Applied Physics Letters*, 110(23):233101, 2017.

[106] Pierre-André Mortemousque, Emmanuel Chanrion, Baptiste Jadot, Hanno Flentje, Arne Ludwig, Andreas D. Wieck, Matias Urdampilleta, Christopher Bäuerle, and Tristan Meu-

nier. Coherent control of individual electron spins in a two-dimensional quantum dot array. *Nature Nanotechnology*, 16(3):296–301, Mar 2021.

[107] W. I. L. Lawrie, H. G. J. Eenink, N. W. Hendrickx, J. M. Boter, L. Petit, S. V. Amitonov, M. Lodari, B. Paquelet Wuetz, C. Volk, S. G. J. Philips, G. Droulers, N. Kalhor, F. van Riggelen, D. Brousse, A. Sammak, L. M. K. Vandersypen, G. Scappucci, and M. Veldhorst. Quantum dot arrays in silicon and germanium. *Applied Physics Letters*, 116(8):080501, 2020.

[108] Yao Wang, Juan Pablo Dehollain, Fang Liu, Uditendu Mukhopadhyay, Mark S. Rudner, Lieven M. K. Vandersypen, and Eugene Demler. Ab initio exact diagonalization simulation of the nagaoka transition in quantum dots. *Phys. Rev. B*, 100:155133, Oct 2019.

[109] A. V. Onufriev and J. B. Marston. Enlarged symmetry and coherence in arrays of quantum dots. *Phys. Rev. B*, 59:12573–12578, May 1999.

[110] Donovan Buterakos and Sankar Das Sarma. Ferromagnetism in quantum dot plaquettes. *Phys. Rev. B*, 100:224421, Dec 2019.

[111] Xuedong Hu and S. Das Sarma. Hilbert-space structure of a solid-state quantum computer: Two-electron states of a double-quantum-dot artificial molecule. *Phys. Rev. A*, 61:062301, May 2000.

[112] Xuedong Hu and S. Das Sarma. Spin-based quantum computation in multielectron quantum dots. *Phys. Rev. A*, 64:042312, Sep 2001.

[113] Erik Nielsen, Edwin Barnes, J. P. Kestner, and S. Das Sarma. Six-electron semiconductor double quantum dot qubits. *Phys. Rev. B*, 88:195131, Nov 2013.

[114] C. J. van Diepen, T.-K. Hsiao, U. Mukhopadhyay, C. Reichl, W. Wegscheider, and L. M. K. Vandersypen. Quantum simulation of antiferromagnetic heisenberg chain with gate-defined quantum dots. *Phys. Rev. X*, 11:041025, Nov 2021.

[115] A. Mielke. Ferromagnetism in the hubbard model on line graphs and further considerations. *Journal of Physics A: Mathematical and General*, 24(14):3311–3321, jul 1991.

[116] A Mielke. Exact ground states for the hubbard model on the kagome lattice. *Journal of Physics A: Mathematical and General*, 25(16):4335–4345, aug 1992.

[117] Hal Tasaki. Ferromagnetism in the hubbard models with degenerate single-electron ground states. *Phys. Rev. Lett.*, 69:1608–1611, Sep 1992.

[118] Donovan Buterakos and Sankar Das Sarma. Certain exact many-body results for hubbard model ground states testable in small quantum dot arrays, 2022. arXiv:2202.11115.